Experimental Investigation of the Flow Behaviour Inside a Centrifugal Impeller Channel at Design and Off-Design Flow Rates.

by

Ammar Mohammadnour Altaf

A thesis
presented to the University of Waterloo
in fulfilment of the
thesis requirement for the degree of
Master of Applied Science
in
Mechanical Engineering

Waterloo, Ontario, Canada, 2007

I hereby declare that I am the sole author of this thesis. This is a true copy of the thesis, including any required final revisions, as accepted by my examiners.

I understand that my thesis may be made electronically available to the public.

Ammar M. Altaf

Abstract

An experimental study of the flow behavior inside the channels of an 8-blade backswept low specific speed impeller at design and off-design conditions is presented. The measurements took place at both the inlet and the outlet of the impeller channel at the mid height of the channel passage. The particle image velocimetry (PIV) technique was used to measure the velocity components in the inlet and outlet frames of the impeller channel. The flow behavior inside the channel, the mean normalized primary and secondary velocity components at six radial locations inside the channels, and turbulence intensity in terms of the variation in the relative velocity components were investigated at the design condition, 75%, 50%, 40%, 30% and 25% of the design flow rate. The results demonstrated a well behaved flow with no evidence of flow separation at the design condition. The fluid flow inside the impeller channel started experiencing a flow separation, when the flow rate is reduced, which propagated throughout the channel passage and caused the channel to stall with a large recirculation zone at severe off-design flow rates.

Acknowledgments

In the name of God, the most Gracious, the most Merciful.

First, I wish to thank God for all the success He provided me in my life especially the successful accomplishment of this degree.

Also, I would like to express my sincere thanks to Professor David A. Johnson, the man, who supported me through the hard times of my father's sickness and the good times of the birth of my first baby, the supportive academic supervisor, who enriched my humble knowledge with his great expertise. This work would have been impossible without his encouragement and support.

Special thanks to my colleagues Zeyad Almutairi, Adam Mcphee, Mike Macwilliam, Brian Gaunt and Steve Orlando who supported me in different stages of this work. I would also like to thank the workshop technicians who helped me at this work.

This degree is fully supported by Saudi Aramco Company in the form of graduate scholarship. I am very thankful for their support.

I wish that God would make it possible for me to return part of what my parents have done for me. Their prayers, guidance and encouragements saw me through all the steps of my life. I would like also to thank my supportive brothers and sisters for their prayers.

Finally, I am deeply grateful to my wonderful friend, companion and wife, Zahara, who was there for me at all times. Her support, encouragement, prayers and patience are milestones in accomplishing this degree. The smile on my son's face, Abdulelah, when carried by you made me work hard to accomplish this degree. Thank You.

Contents

4 Results and Discussion 87

List of Figures

List of Tables

Nomenclature

Latin

A	Flow area (m^2)
a	Particle acceleration (m/s^2)
B	Bias error
b	Blade height (m)
b_1	Inlet blade height (m)
b_2	Outlet blade height (m)
b_s	Shroud blade height (m)
C_s	Light scattering cross section (m^2)
d_p	Particle diameter (μm)
D_2	Impeller exit diameter (m)
g	Acceleration due to gravity (m/s^2)
H	Head (mH_2O)

I_0	laser intensity
L_{int}	Interrogation area dimension (pixels)
M	Image scale factor
N_s	Specific speed
P	Precision error
p	Pressure (N/m^2)
P_w	Ideal Power (W)
P_s	Total light scattered power (W)
Q	Volume flow rate (m^3/s)
r	Radius (m)
r_1	Inlet radius (m)
r_2	Outlet radius (m)
r_s	Shrouded radius (m)
S	Standard deviation (m/s)
t	Time (s)
t_b	Blade thickness (m)
T	Torque (Nm)
T_{Tare}	Tare torque (Nm)
U	Circumferential velocity (m/s)
U_2	Outlet circumferential velocity (m/s)
U_f	Fluid velocity (m/s)

U_g	Velocity due to gravity (m/s)
U_p	Particle velocity (m/s)
U_s	Velocity lag (m/s)
V	Absolute velocity (m/s)
$\vec{V}$	Velocity vector(m/s)
V_m	Meridional velocity (m/s)
V_t	Tangential component of absolute velocity (m/s)
V_x	Absolute velocity component in x-direction (m/s)
V_y	Absolute velocity component in y-direction (m/s)
W	Relative velocity (m/s)
W_p	Primary component of relative velocity (m/s)
W_s	Secondary component of relative velocity (m/s)
W_x	Relative velocity component in x-direction (m/s)
W'_x	Radial fluctuating of relative velocity (m/s)
W_y	Relative velocity component in y-direction (m/s)
W'_y	Tangential fluctuating of relative velocity (m/s)
Z	Number of blades

Greek

α	Absolute velocity angle (deg)
β	Blade angle (deg)
β_d	Deviation angle (deg)
β_r	Relative velocity angle (deg)
Δd	Distance traveled by the particle (m)
Δt	Time between illumination pulses (s)
Δu	Slip velocity (m/s)
η	Efficiency
θ	Angle between the horizontal direction and location of velocity vector in the vector map (deg)
μ	Fluid dynamic viscosity (Ns/m^2)
ν	Fluid kinematic viscosity (m^2/s)
ρ	Density (kg/m^3)
ρ_f	Fluid density (kg/m^3)
ρ_p	Particle density (kg/m^3)
φ	Flow coefficient
ψ	Head coefficient
ω	Angular velocity (rad/s)

Subscripts

$_1$	Inlet section
$_2$	Outlet section
$_f$	Fluid
$_p$	Particle
$_x$	Index in x-direction
$_y$	Index in y-direction

Abbreviations

2-D	Two Dimensional
3-D	Three Dimensional
BEP	Best Efficiency Point
CNC	Computer Numerical Control
CCD	Charge-Coupled Device
CFD	Computational Fluid Dynamics
FFT	Fast Fourier Transform
LDV	Laser Doppler Velocimetry
LES	Large Eddy Simulation
Nd:YAG	Neodymium-doped Yttrium Aluminium Garnet
PIV	Particle Image Velocimetry
PS	Pressure side of impeller blade
rpm	Revolutions per minute
RSS	Root Sum Square
SNR	Signal to Noise Ratio
SS	Suction side of impeller blade
TI	Turbulence Intensity
TKE	Turbulent kinetic energy

Chapter 1

Introduction

1.1 Background

Turbomachines are all devices where energy is extracted or added to a continuous stream of moving fluid. White states “The meaning of the Latin origin prefix “turbo-” indicates that this type of machine consists of a rotating part which is usually a row of blades called a rotor connected to a spinning shaft” [1]. Duct fans, compressors and pumps are categorized as turbomachines that absorb power to increase the fluid energy, pressure or head. The other category of turbomachines could be represented by hydraulic, steam and gas turbines where energy is extracted from the fluid by expanding it to a lower pressure or head in which power is produced [2].

“Turbomachines could also be categorized based on the nature of the flow path through the passages of the rotor” [2]. When the running fluid moves parallel to the shaft (axis of rotation), the device is called an axial flow turbomachine. On the other hand, if the fluid changes its path to become perpendicular to the rotation axis, the device is called a radial flow turbomachine. If the direction of the through-flow includes both radial and axial velocity components, the machine is called a mixed flow turbomachine.

Pumps, which are the oldest fluid energy devices known, add energy to fluids and this is accomplished by increasing the total head or pressure of the fluids. A very broad classification of pumps results into two main streams: dynamic and displacement as shown in Figure 1.1 [3].

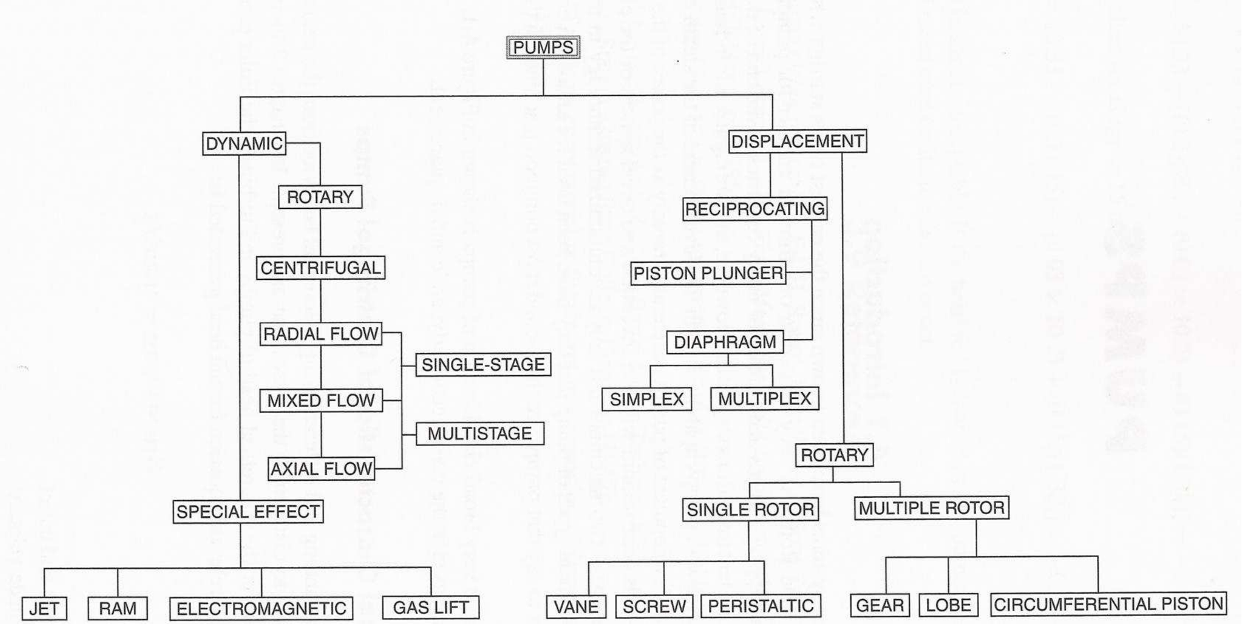

Figure 1.1: Broad classification of pumps [3]

1.2 Centrifugal Pumps

Centrifugal pumps are named from the positive effect of the centrifugal force produced by their rotating impeller on the pressure increase of the passing fluid where energy is added. A centrifugal pump consists of a set of rotating vanes or impellers that receives the fluid from its centre portion called an eye. This fluid passes the impeller channels where it is discharged into a casing known as a volute. During this step, the pressure and absolute velocity of the fluid are increased due to the work applied by the impeller vanes. The volute collects the flow from the impeller and guides it to the discharge opening while converting part of the kinetic energy of the flowing fluid into pressure. Increasing the flow area available to the fluid helps to increase the amount of kinetic energy converted to pressure by reducing the fluid velocity which is accomplished by using a diffuser(Figure 1.2) [4].

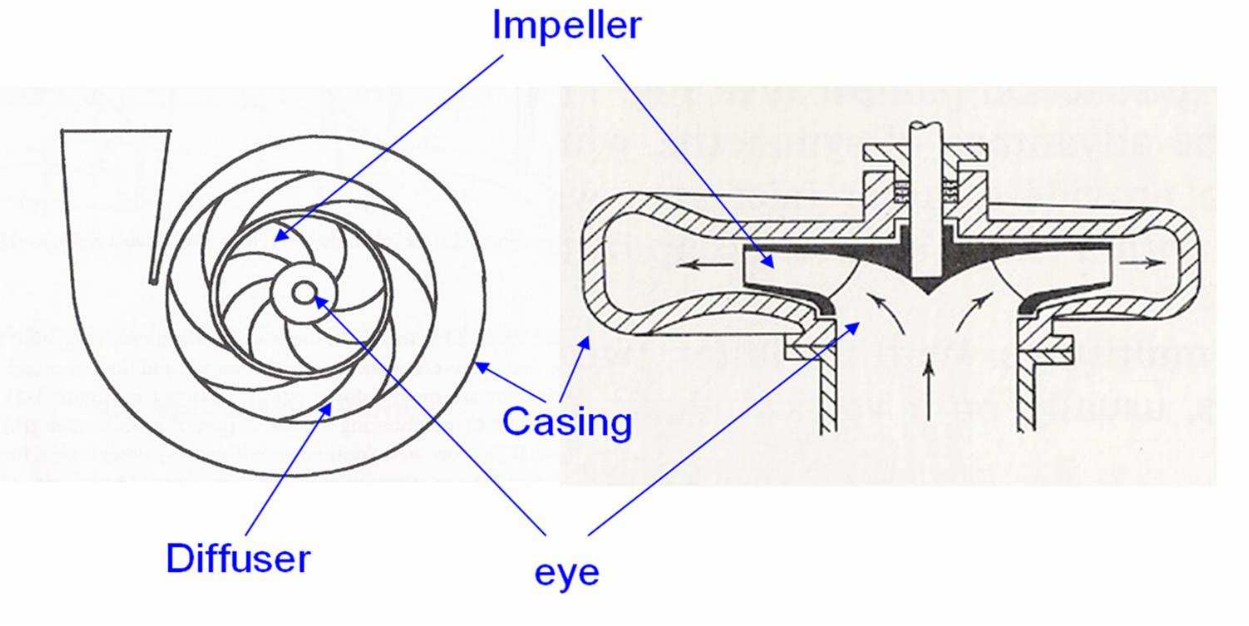

Figure 1.2: Centrifugal pump parts [3, 4]

The changes in the pressure and absolute velocity levels throughout different parts of the centrifugal pump are depicted in Figure 1.3 [3].

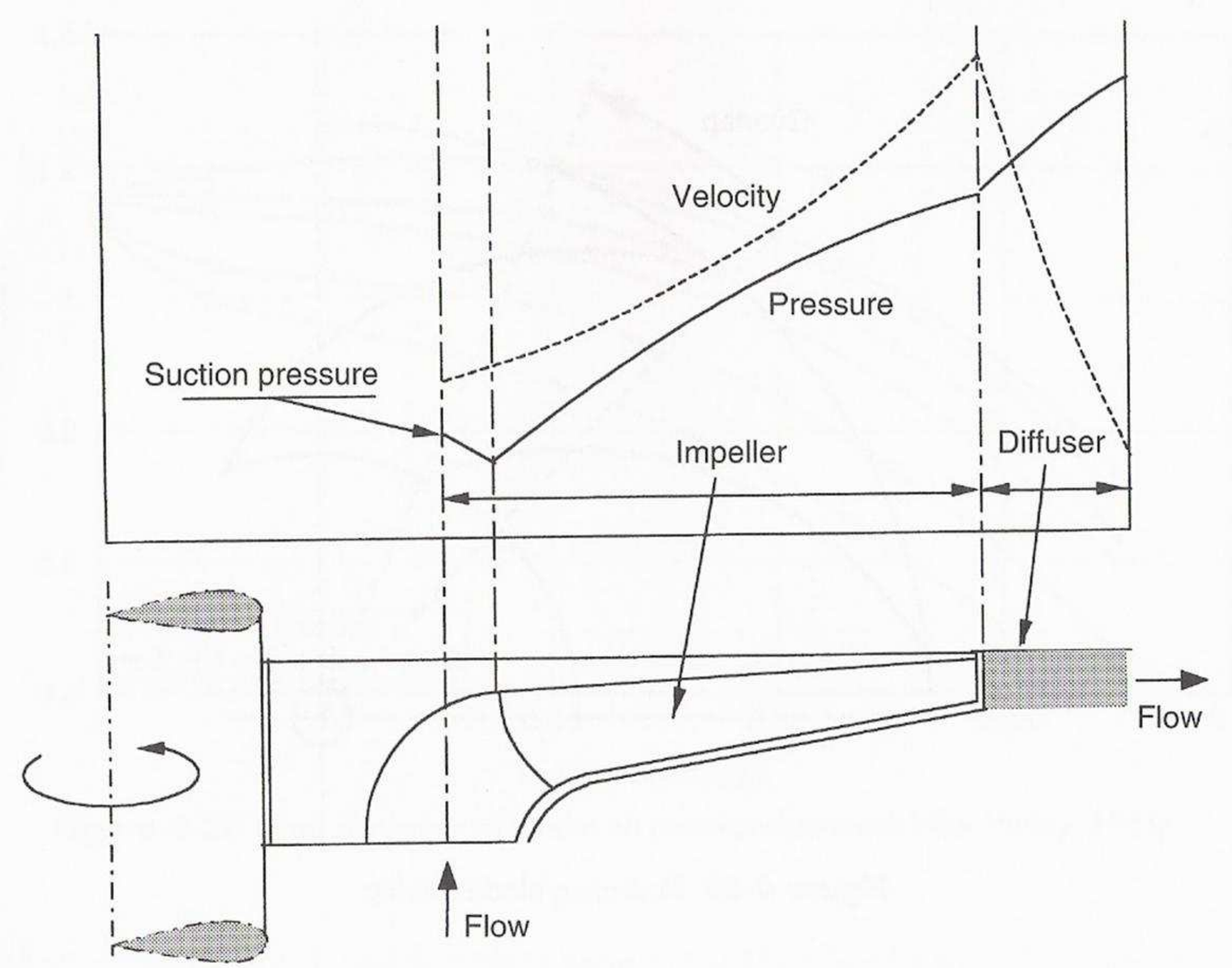

Figure 1.3: Effect of a diffuser on the exit pressure and velocity of a radial pump [3]

1.2.1 Centrifugal Pump Design and Performance Parameters

Improving the performance of a centrifugal pump can be accomplished by increasing the level of energy added to the fluid passing through the impeller channels. As this energy is transported by the work done by the impeller blades, better blade geometry design contributes to higher pump efficiency. Based on the application where the centrifugal pump is to be used, a special design of impeller blades is made. The main step is accomplished through an understanding of inlet and outlet velocity triangles (Figure 1.4).

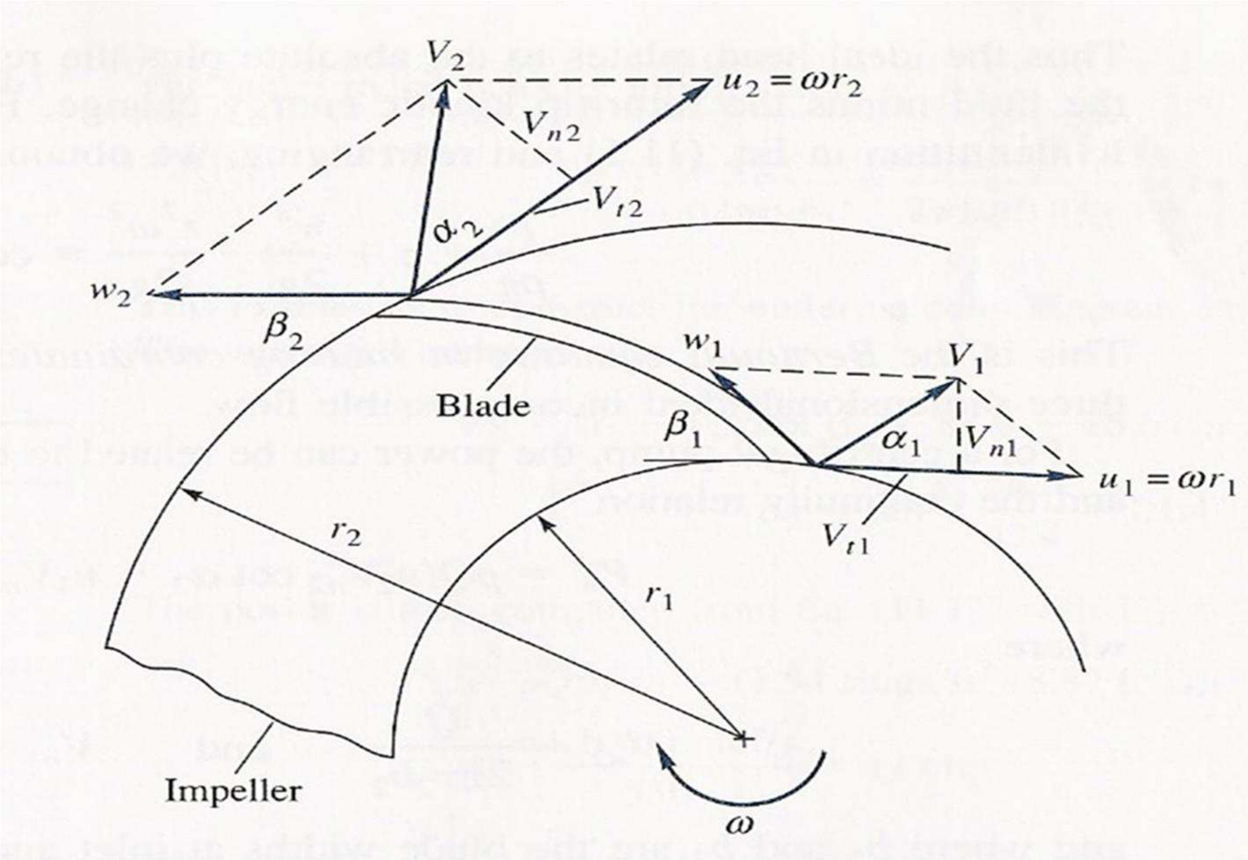

Figure 1.4: Inlet and outlet velocity triangles [1]

In Figure 1.4, ω is the angular velocity, β_1 and β_2 are the inlet and outlet physical blade angles, V_1 and V_2 are the absolute inlet and outlet velocity vectors, α_1 and α_2 are the inlet and outlet absolute velocity angles, u_1 and u_2 are the inlet and outlet tangential velocity, W_1 and W_2 are the inlet and outlet relative velocity and r_1 and r_2 are the inlet and outlet radius. The ideal power delivered to the fluid in centrifugal pumps (incompressible) is expressed by the Euler turbomachine equations

$$P_w = \rho Q(u_2 V_{t2} - u_1 V_{t1}) \tag{1.1}$$

$$H = \frac{u_2 V_{t2} - u_1 V_{t1}}{g} \tag{1.2}$$

where H is the change in fluid pressure head, V_{t1} and V_{t2} are the components of the absolute velocity in the tangential direction, Q is the flow rate through the pump, g is the gravitational force and ρ is the density of the fluid passing through the impeller [5]. By applying dimensional analysis to the centrifugal pump several parameters are extracted which are used to describe the pump. Those parameters are:

$$\text{Flow coefficient: } \varphi = \frac{V_m}{U_2} \tag{1.3}$$

$$\text{Head coefficient: } \psi = \frac{gH}{(U_2)^2} \tag{1.4}$$

$$\text{Specific speed: } N_s = \frac{\omega\sqrt{Q}}{(gH)^{0.75}} \tag{1.5}$$

1.2.2 Centrifugal Pumps Efficiency and Performance Curve

The efficiency of centrifugal pumps, as for other equipment, can be measured by computing the ratio of the output power to the input power. The output power in a centrifugal pump is the added power to the passing fluid while the input power is the one exerted by the driving shaft. The centrifugal pump efficiency is expressed as follows:

$$\text{Pump Efficiency: } \eta = \frac{\rho g Q H}{T\omega} \tag{1.6}$$

where T is the torque applied by the shaft to rotate the impeller. As mentioned above, for each application there is a pump design that works best for that application. Performance charts of centrifugal pumps for the application of interest are usually used. A typical performance chart of a centrifugal pump is shown in Figure 1.5.

The peak of the efficiency curve in a performance chart is called the best efficiency point (BEP) where all other performance parameters of interest are calculated.

The performance of the impeller could be greatly affected by several factors such as inlet and outlet blade angles, number of blades, fluid viscosity and percentage of design flow rate. It was demonstrated by Varley in [3] that values of β_2 greater than 27 degrees produce unstable pump characteristics. The effect of varying outlet angles from 15 to 88 degrees on head and flow coefficients are shown in Figure 1.6.

In the same study, it was also shown that blade numbers above six will give performance instabilities, Figure 1.7.

It should be mentioned that the results shown above only work for the specific impeller

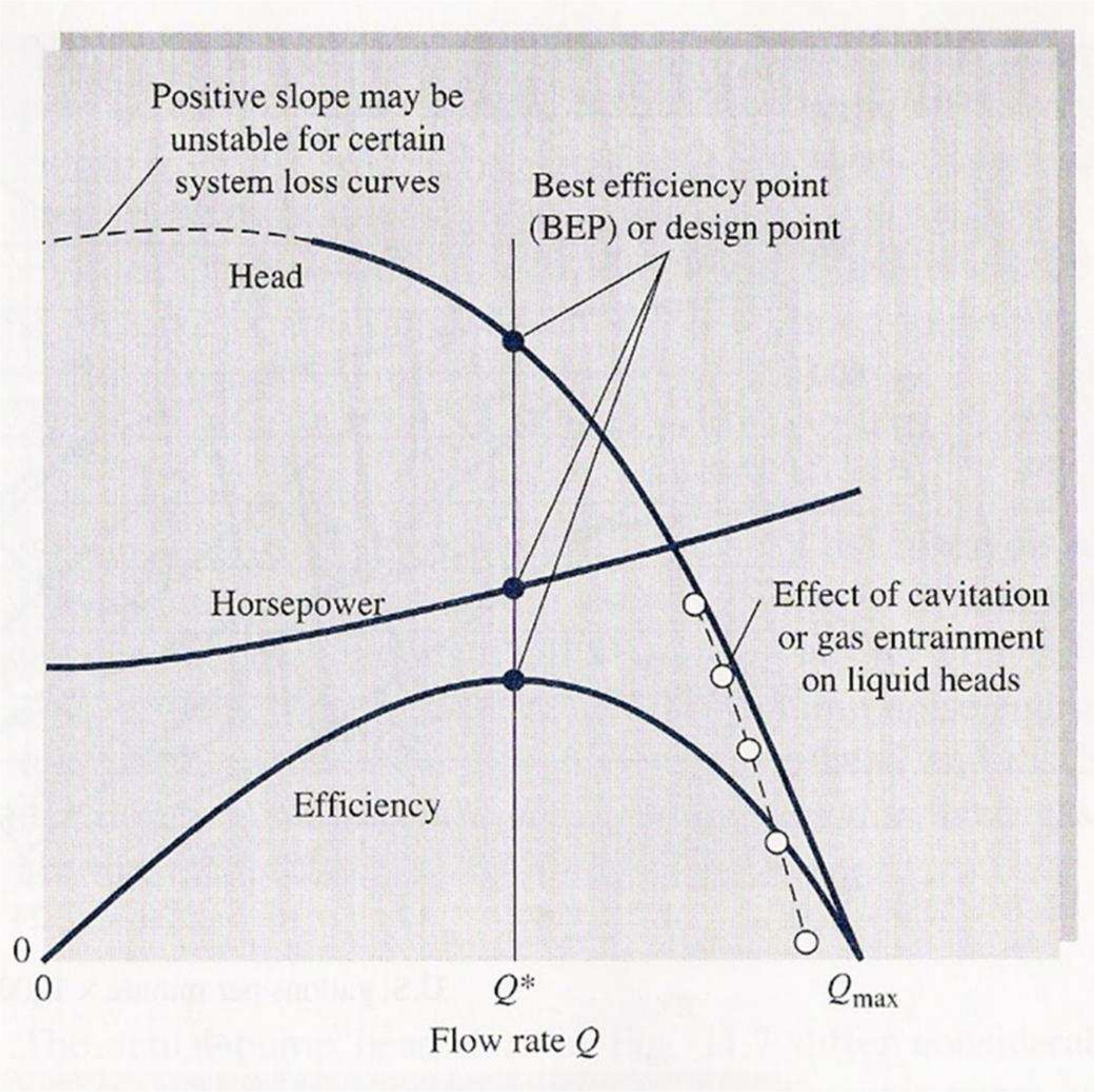

Figure 1.5: Typical pump performance curves [1]

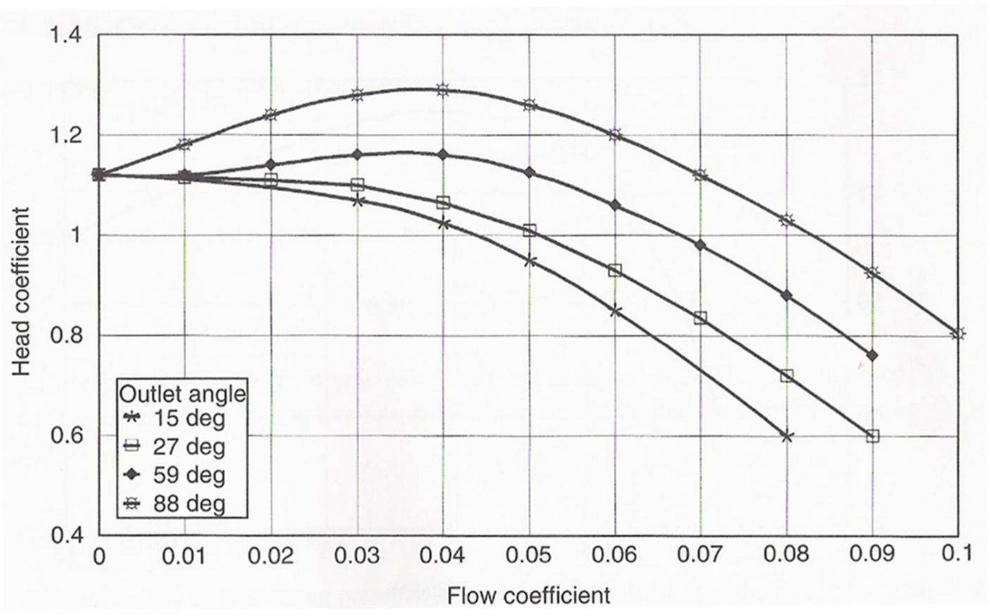

Figure 1.6: Effect of outlet blade angle on pump performance [3]

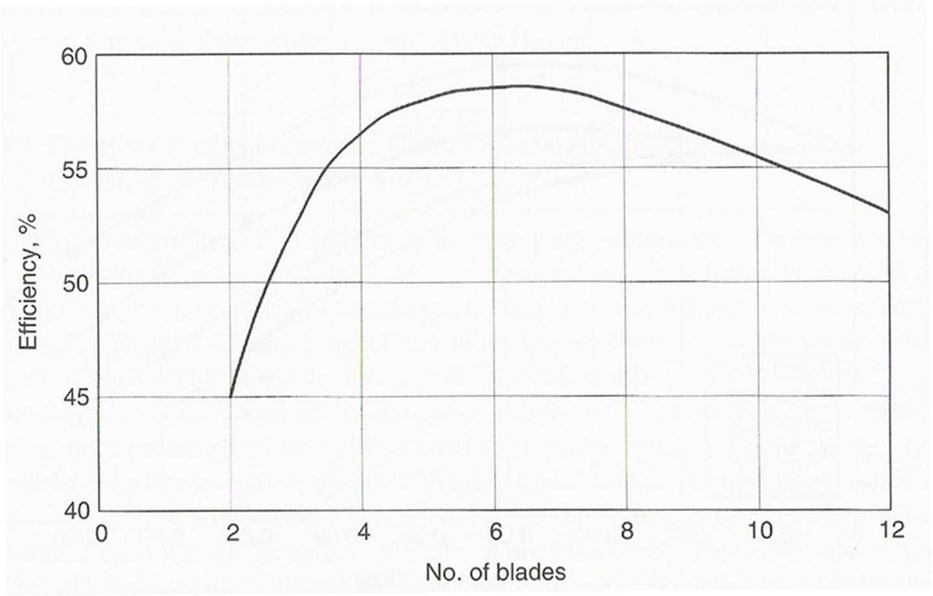

Figure 1.7: Effect of blade number on pump performance [3]

used in that study and the only reason it was mentioned here is to show that the number of impeller blades would definitely affect the pump performance. Furthermore, it was demonstrated that as the viscosity of the fluid increases, the centrifugal pump performance decreases. This is because high viscosity results in a rapid increase in the disc friction losses over the outside of the impeller shroud and hub as well as hydraulic losses in flow channels of the pump. It was also shown that for higher viscosity fluids, an impeller with fewer blades should be chosen.

Theoretically, when the fluid follows the blade angle (β_2) without deviation and no friction is encountered, the relation between the flow coefficient (φ) and the head coefficient (ψ) is expressed by the following equation [5]:

$$\psi = 1 - \varphi \cot(\beta_2) \tag{1.7}$$

Equation 1.7, which is a modification to the Euler Turbomachine Equation, shows the effect of the blade angle upon the energy rise in terms of head in the ideal case [6, 5]. The flow is said to slip due to the reduction of the blade curvature effect on the fluid direction at the channel exit. The ratio of the actual tangential velocity (V'_{t2}) over the ideal tangential velocity (V_{t2}), is known as the slip factor(σ) (Figure 1.8).

$$\sigma = \frac{V'_{t2}}{V_{t2}} \tag{1.8}$$

Several models evolved to include the effect of fluid slip in the form of a slip factor into Equation 1.7. For this experiment where the curvature of the impeller blade is 30 degrees,

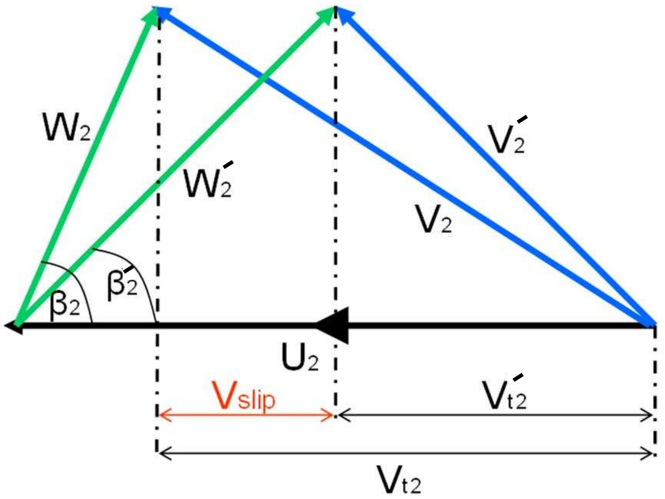

Figure 1.8: Slip model and hypothetical velocity diagrams at outlet of backward swept impeller

a model developed by Wiesner (1967) was used [7]. The slip factor and head and flow coefficient using the Wiesner model are as follows:

$$\text{slip factor:}(\sigma) = \frac{1 - \sqrt{\sin(\beta_2)}}{Z^{0.7}} \tag{1.9}$$

$$\psi = \sigma - \varphi \cot(\beta_2) \tag{1.10}$$

An application of this model will be presented in Chapter 4.

1.2.3 Flow Behaviour Inside Centrifugal Pump Channels at Design Flow Rate

Predicting the flow behaviour inside centrifugal pump channels is the key to improving the pump efficiency. Any change in a flow parameter could affect the flow behaviour and the pump efficiency. Designing a pump to efficiently handle a wide range of flows away from the BEP is relatively difficult. Two types of flow contribute to the final flow pattern inside an impeller channel. The first is the primary flow which follows the direction of the blade passage centre line. The second type of flow is the secondary flow which is the velocity field transverse to the primary flow. Changing the flow parameters and the values of the primary and secondary flows produce several unsteady behaviours. Stationary unsteadiness such as flow separation and wakes are associated with pressure gradients, secondary flow and boundary layer stability in the channel [8]. When the boundary layer encounters a sufficiently large adverse pressure gradient, the fluid flow becomes detached from the surface of the channel's blade and flow separation occurs. Vortices which are the swirling of the fluid in the area of the lower pressure gradient occur in the separation area close to the channel's blade. Rotating stall and cyclic flow inside the channel are known as periodic unsteadiness. Stall usually consists of areas of recirculating fluid inside an impeller channel that cause significant velocity and pressure fluctuations which block the impeller's channel. A stall that alternates between the impeller channels is called a rotating stall. Due to impeller rotation, the Coriolis forces affect the primary flow and so generate the secondary flow [1]. Also viscous effects and the blade curvature play an important role on the primary flow path [8]. If a local velocity, for example at the tip of the blade in the inlet, is high enough and the pressure is reduced to lower than the fluid's vapor pressure, the liquid will then vaporize at that location and very tiny bubbles are formed. When the fluid moves to a region with higher pressure, those bubbles will condense or collapse. This phenomenon is known as cavitation which is another form of fluid flow instability [4].

Based on the Euler turbomachine equations which assumes ideal flow in an infinite number of blades [1], the flow pattern inside an impeller should follow the blade geometry. On the other hand, Petermann and Pfleiderer [9] concluded that the flow pattern inside an impeller passage which is governed by the Euler turbomachine equation is actually a combination of two different flow scenarios. The first scenario is the relative eddy that results from the flow of a fluid inside a completely closed impeller channel when the impeller is rotating. This relative eddy is rotating in an opposite direction to that of the impeller Figure 1.9 a. The other scenario is when a fluid is passing through a channel of a stationary impeller where the flow pattern will follow the blade curvature Figure 1.9 b. Combining these two flow behaviours would generate a flow pattern as the one shown in Figure 1.10.

In Figure 1.10, it is shown that the flow streamlines move towards the suction side (SS) at the inlet and towards the pressure side (PS) when they approach the channel outlet. Due to the high pressure gradients which decrease when moving from the pressure side to the suction side, the relative velocity gradients are higher on the suction side than on the pressure side. This flow pattern was explained in 1928 by Busemann using the mean line analysis [10].

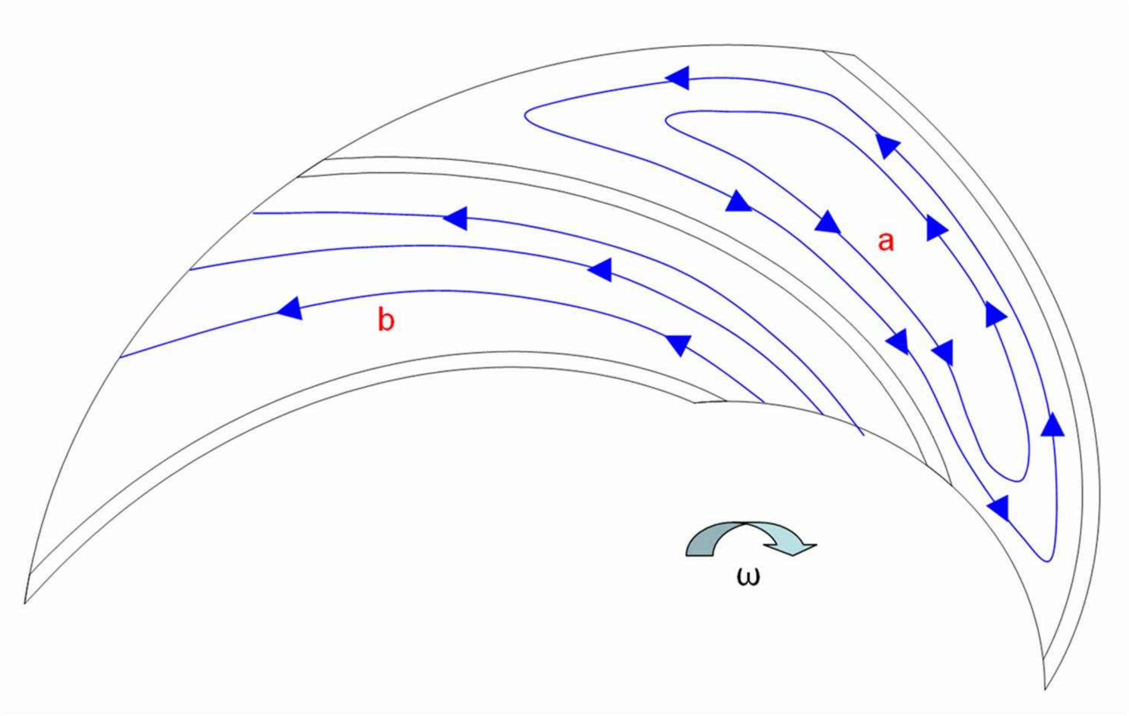

Figure 1.9: Components of potential flow pattern in a rotating impeller

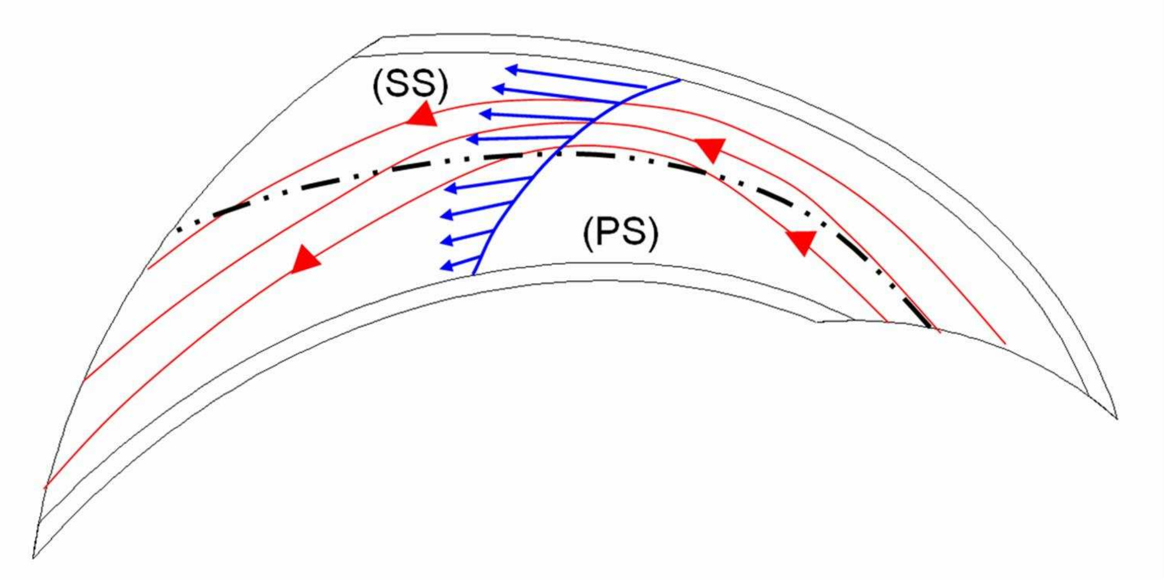

Figure 1.10: Resultant flow behaviour based on Petermann and Pfleiderer [9]

1.2.4 Flow Behaviour Inside Centrifugal Pump Channels at Off-Design Conditions

Running an impeller at flow rates different from the design flow rate greatly affects the flow patterns inside the impeller channels. Stall formation, vortices, alternating channel stall and cavitation are different possible results of reducing the flow rate which causes degradation in the impeller efficiency.

Krause and Pap [11] explained the formation of flow separation and stall inside impeller channels. At design flow rate, the stagnation point of the flow is located on the blade leading edge in which the fluid flows around both sides of the impeller blade(Figure 1.11 a). If the flow rate is reduced, the meridional component of the relative velocity, W_m, also decreases. As a result, the flow angle of attack rises and the stagnation point moves to the pressure side of the blade. When the angle of attack exceeds a certain threshold, the flow on the suction side will detach and stall can appear (Figure 1.11 b). The static pressure inside the stall region is smaller than that in the surrounding flow; therefore, small vortices can appear in that region.

Vortices appear in the separation region because the static pressure inside the stall region is smaller than in the surrounding flow. With the existence of several vortices in the stall region, they start growing until the complete channel is blocked. If a channel is blocked, this means that the flowing fluid will have to pass through the following channel, channel 3 in Figure 1.11 c. As stated before, the stagnation point of the relative velocity will be moved in channel 3 of Figure 1.11 and a new separation region will be formed in this channel.

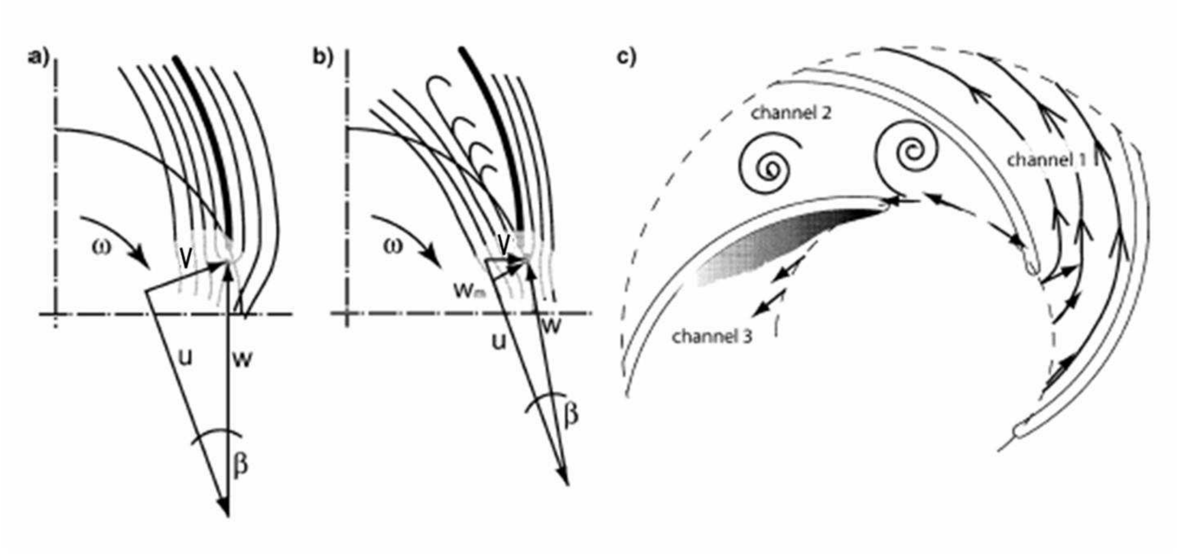

Figure 1.11: Velocity components and flow around the blade at a) design condition b) off-design condition and c) stall formation in a centrifugal impeller [11]

If channel 3 is blocked, the flow in channel 2 will reattach and the flow conditions in this channel will improve. Repeating the same scenario, the stalled channels rotate opposite to the impeller rotation. However, it is important to note that stall formation and movement inside the impeller channel differs from one impeller to another and also as the flow condition changes. This theoretical description of the rotating stall phenomenon was first published by Emmons (1955).

1.3 Particle Image Velocimetry

In 1984, Particle Image Velocimetry was evolved by Meynart [12] as a result of several experiments using laser illumination to produce Young's interference fringes out of displaced laser speckles. Known earlier as Laser Speckle Velocimetry, the PIV technique underwent several stages of development to accurately and quantitatively measure fluid velocity vectors at a very large number of points at the same time. The PIV technique is a non-intrusive measurement technique to study the velocity of particles in some type of flow that could be either gas or liquid.

Briefly, in a PIV application, carefully selected tracer particles are seeded in the flow to represent the flow pattern and behaviour of the original medium (seeding). These tracer particles are illuminated in a plane of the flow at least twice within a short time interval Δt (illumination). The light scattered by the particles is recorded either on a single frame or on a sequence of frames using special cameras via high quality lenses (image recording) as shown in Figure 1.12. A processor is used to assure the image is captured at the same time the plane is illuminated (synchronization). To be able to handle the great amount of data collected employing the PIV technique, sophisticated post-processing is required using special software and a computer. The displacement of the particle, Δd, between the light pulses is determined through evaluation of the PIV recordings. The evaluation process of the PIV recording divides these recordings into small sub areas called ”interrogation areas”. The local displacement vector for the images of the tracer particles between the first and second illumination is determined for each interrogation area by means of statistical methods (correlation). The data collected must be verified to remove any incorrect velocity vectors, outliers, resulting from the correlation step (validation). Following these steps, the PIV technique will eventually provide an instantaneous whole field map represented as velocity vectors. The magnitude of each velocity vector is calculated using the following equation:

$$V = M(\frac{\Delta d}{\Delta t}) \tag{1.11}$$

where M is the scale factor of the actual test dimension and the image size.

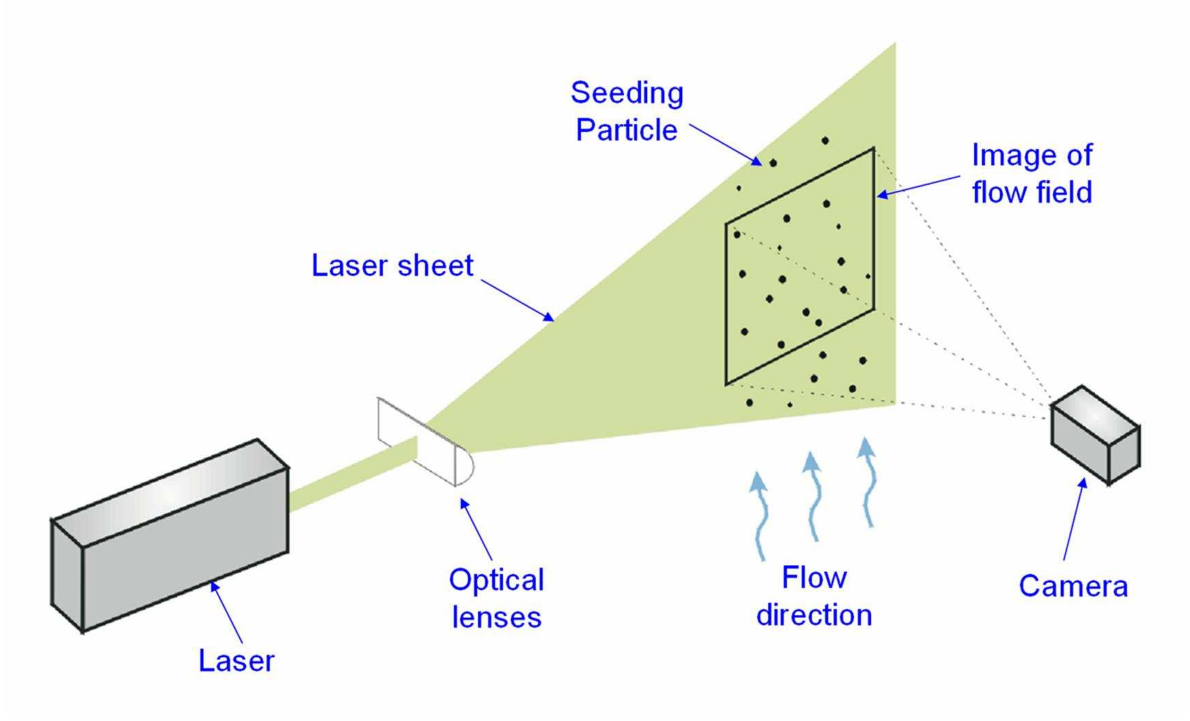

Figure 1.12: Typical 2-D PIV setup

1.4 Literature Survey

In this section, literature survey observations will be presented for subjects related to flow behaviour inside centrifugal impeller channels at both design and off-design conditions. This will include, but not be limited to, researches done with techniques other than PIV. Research concerning the application of particle image velocimetry (PIV) will also be provided.

1.4.1 Centrifugal Pump Flow Behaviour

Krause et al. [11] used the PIV technique to determine the velocity fields in a 5-blade backswept radial pump impeller with a specially designed volute. At design conditions, higher velocity gradients at the suction side were found as opposed to lower velocity gradients close to the pressure side. This matches the flow behaviour described in section 1.2.3. A standing stall cell was formed at an off-design flow rate of 50 % in only one channel. The stall cells were observed in several channels of the impeller as the flow rate was decreased to 41 %. It was noted that the stall cells were rotating in an inverse direction of the impeller movement. For flow rates of 35 % of the design condition and lower, a continuous rotation of the stall cells was observed which appeared to be repeated at a steady sequence.

Johnson et al. [13] used Laser Doppler Velocimetry (LDV) to measure velocity components in the passages of a 6-blade backswept low specific speed centrifugal pump and its volute region. The measurements were taken at both design and off-design conditions. The results showed a well behaved flow pattern at the design flow rate while an alternating stable stationary stalled and un-stalled passages were observed at an off-design flow rate of 25 %. At design flow rate, the peak relative velocities were the highest near the suction side of the blade at the middle of the passage while the highest relative velocities at the exit of the passage were observed near the pressure side of the blade. At a flow rate of 25 %, an alternating stall was evident in which reverse flows were observed at both the suction and the pressure sides of the blade with different percentages throughout the passages which does not coincide with most of previous studies.

Johnson and Onwuama [14] used PIV to investigate the internal flow structure and flow separation in the rotating passage of a low specific speed centrifugal pump impeller using a glass cover on one of the impeller's 8 blade backswept passages at design conditions. Their results indicated the existence of a transient separation near the suction surface at the impeller exit. Also a distorted prerotated inlet velocity profile and high velocity fluctuation were observed. At design flow, an increase in the primary velocity which followed the blade curvature was noticed from the inlet to outlet of the passage along both the suction and pressure side. A distorted inlet velocity profile due to the sudden direction change in the flow direction at the inlet was observed. Their results were supported by the calculation of turbulence intensity (TI) inside the impeller passage using the following equation:

$$TI = \frac{\sqrt{0.5(\overline{W_x'^2} + \overline{W_y'^2})}}{\sqrt{W_x^2 + W_y^2}} \tag{1.12}$$

An increase in the turbulence intensity from the inlet to the exit of the passage along the pressure side was observed [14].

Abramian and Howard [8] used LDV to study a low specific speed impeller with eight blades. It was found that at design and off-design conditions, the relative flow in the impeller passage was subjected to stationary and periodic unsteadiness. At the design flow rate, the flow at the inlet was non-uniform and its behaviour was three dimensional and distorted. They suspected the distortion may be associated with flow separation and recirculation at the inlet near the shroud, where the flow turned from axial to radial, through the sealing ring. The flow recirculation resulted in a dead-water "blocked" zone concentrated at the passage mid-height near the shroud. At the middle portion of the passage, the flow was not affected by the inlet distortion and, generally, followed the blade passage with no significant three-dimensional non-uniformity. At the exit region of the passage, the flow followed the passage without any significant axial or tangential distortion from hub to shroud. Near the pressure and the suction sides of the passage, the flow followed the blade with no significant deviation. Mid-way between the two surfaces of the passage the flow deviated towards the pressure side. This indicates that at the inlet of a radial centrifugal impeller it is difficult to predict the fluid flow behaviour due to the sudden change of the flow direction from axial to radial which is not the case at the outlet. As a result, comparing similar studies at the inlet of an impeller is not always meaningful.

At 50 % flow rate, the pressure gradient near the hub was much stronger resulting in much higher velocities along the suction surface and unlike the design flow rate, the flow near the shroud was affected by the pressure gradient and forced the flow along the pressure side away from the blade. Flow separation occured near the pressure side at the middle portion of the passage extending up to 85 % of the passage where the flow reattached with no further extension of a low energy wake region. The separation zone was confined along the pressure side where low velocities were observed with no distinct flow recirculation. At the passage exit, the separated flow along the pressure side was reattached, resulting in a uniform exit flow free from distortion and wake. The turbulence intensities were determined from the average tangential and radial fluctuations using Equation 1.12 above. An increase in intensity from 10 % to 20 % was noticed when moving from the suction side to the pressure side [8].

In a flow visualization study using the hydrogen bubble technique, Howard and Herman [15] studied the flow pattern partially inside an impeller placed in a casing with a single throat volute and another with double throat volute. A volute is the housing around the impeller that collects the fluid coming out of the impeller channels and guides it through a discharge nozzle to the downstream piping. In a double volute design, the discharge nozzle is split into two cavities receiving the discharged fluid from different halves of the impeller as shown in Figure 1.13. The flow pattern showed a tendency toward stall and separation on the pressure surface of the blade, becoming more severe at reduced flow rates in the case of no volute. The volute introduced a cyclic pattern to the flow which was most intense at very low flow rates where the entire passage opposite to the volute tongue (Figure 1.14) was filled with backflow at low flow rates. Recent papers and research work indicate that separation starts at the suction side rather than the pressure side in centrifugal impellers.

A similar study to understand the flow patterns inside centrifugal pumps was conducted by Choi et al. [17] using the PIV technique with two different types of very low specific speed impellers. The first was a 6-radial-blade un-shrouded impeller (A) while the second was a conventional 4-blade backward swept un-shrouded impeller (B). Both were tested at design flow and off-design flow rate of 25 %. At design flow rate, the flow pattern inside impeller A passages was very complex and exhibited reverse flow flowing radially inward in the passage. Also, strong secondary flow perpendicular to the radial flow was noticed. At off-design condition(25 % Q) in impeller A, large vortices and reverse flows appeared

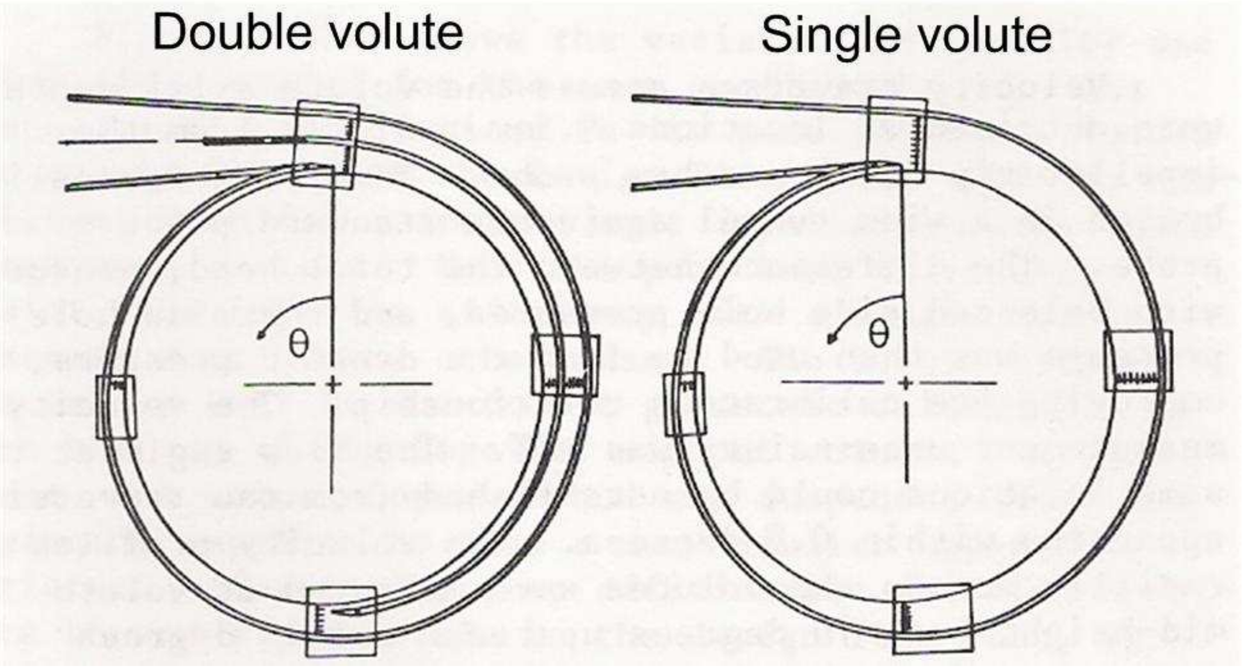

Figure 1.13: Single and double volute design [15]

near the pressure side of the blade in which the vortices were associated with an increase in the magnitude of the reverse flow. When the flow rate was increased to more than the design flow rate, all the passage vortices disappeared. Inside the passages of impeller B, the flow pattern was following the contour of the passages in a smooth pattern along both the pressure and suction side of the passage at the design flow rate. At flow rates of 25 % there were no vortices formed and no strong reverse flow was observed as opposed to impeller A. At 150 % flow rate a remarkably smooth flow pattern was observed. It is important to note that leakage over the blades tip in un-shrouded design makes the flow pattern, specially the reversed flow, incomparable to that of the closed type centrifugal impeller [17].

The flow inside shrouded and un-shrouded impeller passages running at off-design flow rate was visualized by Lennemann and Howard [18] using the hydrogen-bubble technique.

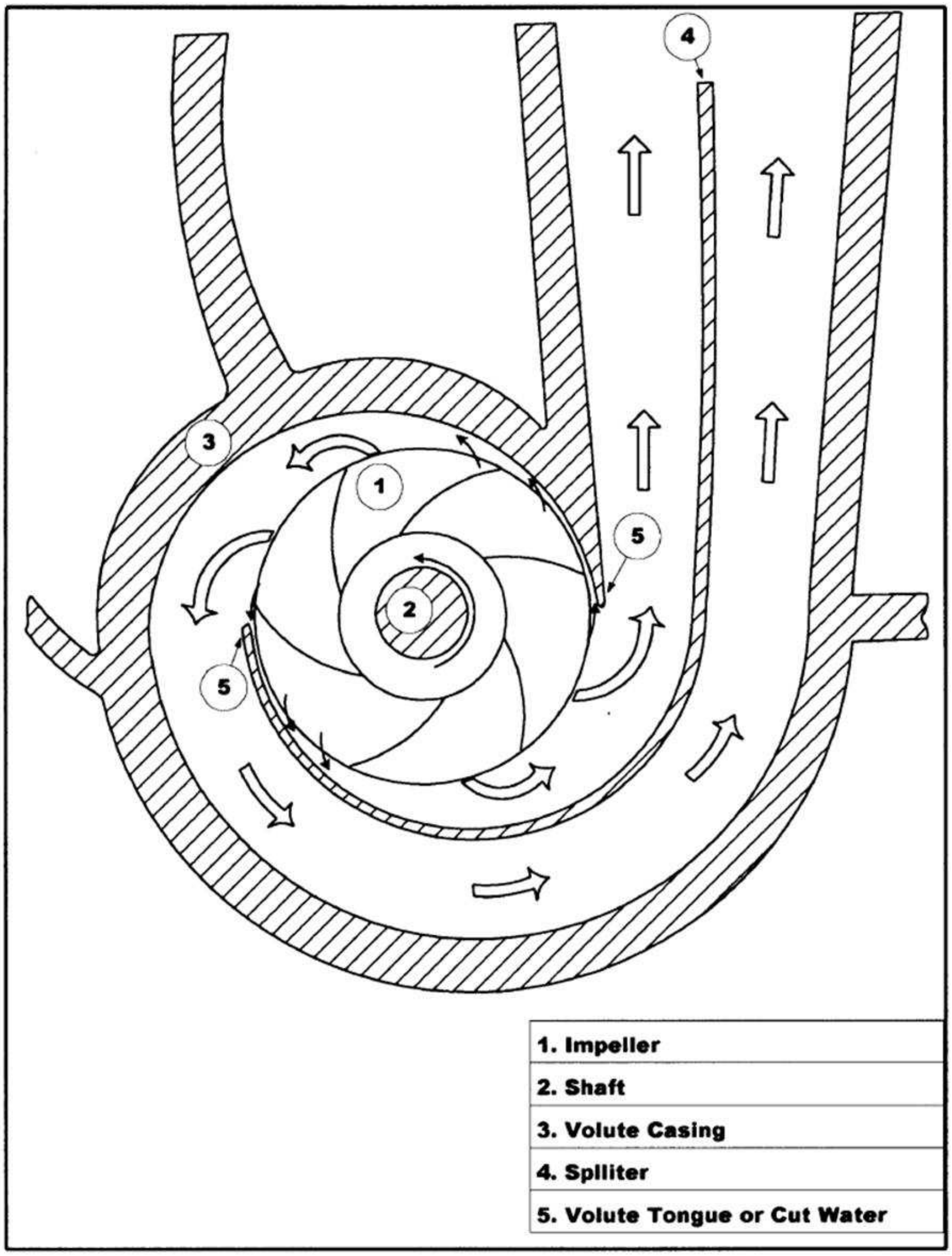

Figure 1.14: Sketch of volute components [16]

The impeller studied consisted of 14 backward swept blades with inlet and outlet blade angles of 20 and 26 degrees, respectively. At off-design condition for the shrouded impeller, it was observed that the boundary layer on the blade suction side separated and backflow occurred along the suction side blocking off the passage discharge side and reversed the flow direction in the passage. The fluid in the passage accelerated towards the passage entry moving out of the passage into the inducer. It was observed that, due to this motion, the boundary layer at the pressure side of the downstream passage part separated. The secondary flow pattern was also obtained and it was concluded that the fluid inside the passage was transported toward the blade suction side. Under the increased adverse pressure gradient along the blade, the suction side boundary layer separated before the pressure side did. At zero flow rate, a relative eddy was noticed inside the impeller passages which rotated opposite to the direction of the impeller rotation. This fact agrees with the flow behaviour explained in section 1.2.3 where an assumption was made that the channel passages were closed. For the un-shrouded impeller at off-design flow rate, the boundary layer separated on the blade pressure side as opposed to that in the shrouded impeller. A strong back flow existed that was supported by a relative eddy where the fluid moved out of the passage towards the inducer.

Howard and Kittmer [19] visualized the flow pattern inside a shrouded and un-shrouded configuration of a radial flow impeller using the hydrogen bubble technique where they measured the secondary flow velocities using a hot-film probe. At design flow condition the primary flow pattern was well behaved in both configurations with no evidence of separation even at the passage exit. A secondary flow pattern started as a single vortex at the entry of a shrouded impeller passage and developed into a dual vortex system at the hub and shroud surfaces sweeping towards the suction side. The slipped flow (the portion of fluid escaping in a different direction as opposed to the general flow pattern) between the blade tip and shroud in the un-shrouded impeller strongly affected the secondary flow in the passage. In contrast to previous studies by Howard [8, 15], the tendency of flow separation in this study occurs at the suction side rather than the pressure side. The difference in the blade curvature design, in which a very small inlet blade angle with big increase at the outlet blade angle in the previous studies, was proposed as the reason for this change in flow separation location.

Choi et al. [20] used hot-wire probes and surface mounted pressure transducers on a seven bladed back swept centrifugal water pump impeller to study the unsteady behaviour pattern and the noise generated from the flow inside the impeller channels. High velocity components were found on the pressure side at the discharge part of the impeller. An unsteady flow separation at the suction side was noticed along the blade where a movement of the flow from the pressure side at the exit of the passage towards the low-pressure region present at the suction side was detected. Periodic pressure fluctuation on the blade surfaces were measured using a pressure tube installed on the impeller surface which caused a rotating stall pattern close the impeller discharge.

Pedersen et al. [21] used PIV and LDV to investigate the flow pattern inside a six blade backswept impeller without a volute at both design flow and quarter design flow. At the design flow rate, a very similar well-behaved flow pattern was observed inside all the six channels of the impeller except at the inlet because of the local curvature effect. At one quarter of the design flow rate, alternating stalled and un-stalled passages were observed. Stalled passages were blocked at the inlet by a large recirculation cell. The remainder of the passage was dominated by a strong relative eddy causing backflow along the blade pressure side close to the exit. The un-stalled passages were characterized by relatively well-behaved flow patterns. The stall formation was stationary and not rotating though the impeller passages.

Li [22] used LDV to study the effect of fluid viscosity on centrifugal pump performance and the flow pattern in the impellers where the fluids used were water and viscous oil with kinematic viscosity of 1 and 48 mm^2/s, respectively. It was observed that the pump efficiency dropped when using the viscous oil and this is due to the fact that the disc friction losses over the outsides of the impeller shroud and hub as well as the hydraulic losses in the flow channel of the pump increased rapidly. It was also observed that the flow patterns near the impeller outlet were less affected by the viscosity of the fluids in best efficiency and off-design conditions, but the flow patterns near the impeller inlet were greatly affected by viscosity. There was a wide wake near the blade suction side of the centrifugal pump impeller and no jet flow near the blade pressure side which resulted in a flow pattern that was different from the well known jet-wake model.

Choi et al. [23] performed PIV analysis of five different types of pump settings. Among them was a four backswept blade un-shrouded impeller inside a volute. At the design flow rate, the flow behaved as mentioned in section 1.2.3. Specifically, the velocity gradient increased towards the suction side at the middle of the passage while it increased again at the pressure side along the passage exit as shown in Figure 1.15.

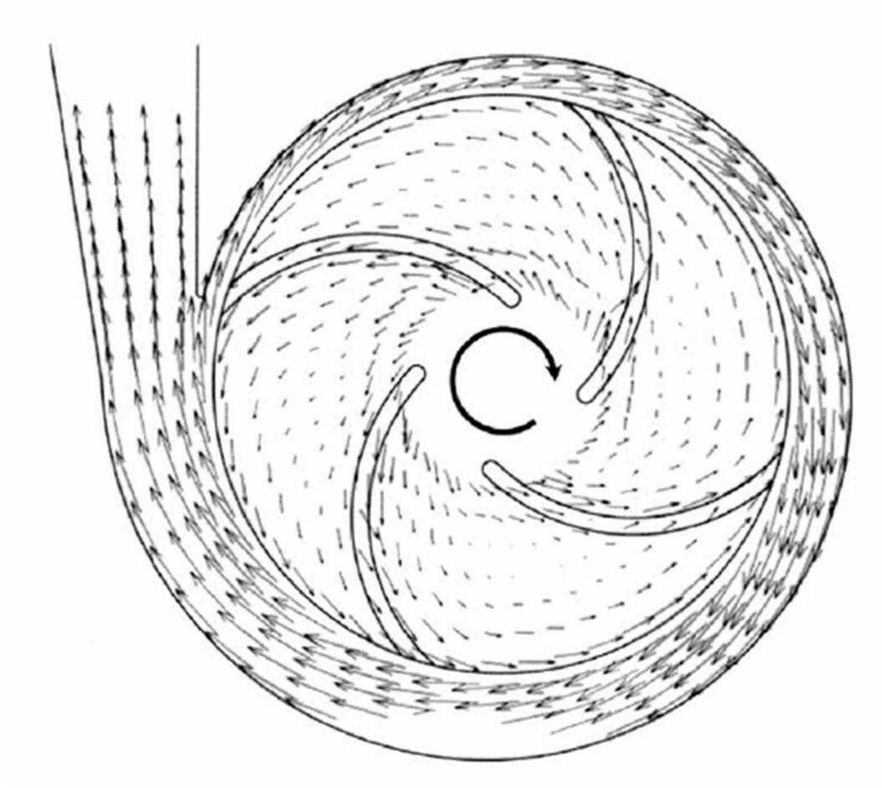

Figure 1.15: Velocity vector map at design flow in a centrifugal impeller [23]

When using the PIV technique in any experimental setup, results accuracy depends on the proper selection of different PIV parameters (section 1.3) that compose the technique. It was demonstrated by Dong et al. [24] that if the particle density and magnification are chosen such that each window (interrogation area) contains at least 8 pairs of particles in both frames, the uncertainty can be kept at about 1 %. In general, it was concluded that as the number of particles in the interrogation area increases, the accuracy in determining the exact value of the velocity in that interrogation area increases. Also the effect of particle size, in terms of pixels, on the overall accuracy of the velocity determination was studied and it was found that as the particle size increases the relative errors (difference between the exact velocity value and computed one) decrease. The application of PIV took place to measure the velocity within the volute of a centrifugal pump at different impeller blade orientations.

1.5 Objective

The objective of this research was to study the flow behaviour inside an 8-blade backward swept centrifugal impeller using the particle image velocimetry technique. The impeller efficiency and performance parameters were measured as it is newly constructed and compared with theoretical pump curves. Flow behaviours including separation, stall formation and turbulence intensity were studied at the design flow rate (100 % Q), 75 % Q, 50 % Q, 40 % Q, 30 % Q and finally at 25 % of the design flow rate which were considered as off-design conditions. Profiles of primary velocity components and secondary velocity components at 6 different locations along the impeller passage were analyzed to support any flow behaviour observed. The results found in this research work were compared with previous results found in the literature.

The detailed analysis of the flow behaviour inside the centrifugal impeller is expected to enhance the overall understanding of centrifugal pumps performance at different operating conditions. The results of this research should contribute to a better design and understanding of centrifugal pumps operation at the design and off-design conditions.

Chapter 2

Experimental Apparatus

The experimental layout will be presented in this chapter. It consists of the experimental rig, the test impeller manufacturing steps, the supporting instruments, the calibration process and preparation. The procedure of conducting the impeller performance measurement and the modifications and repairs done to the experimental rig will also be presented.

2.1 Experimental Test Rig

The experimental test rig used in this research is a closed circuit system in which water is the fluid used. This rig was previously used by Abramian [8], Hesse [25], Onwuama [26] and Behseta [27]. A plan and side view of the experimental rig are shown in Figure 2.1.

As shown in Figure 2.1, the test rig circuit consists of a water reservoir with an approximate capacity of 2.5 cubic meters. Two inlet pipes connect the reservoir tank to a settling tank below the test impeller. The water is drawn from the lower settling tank to the upper

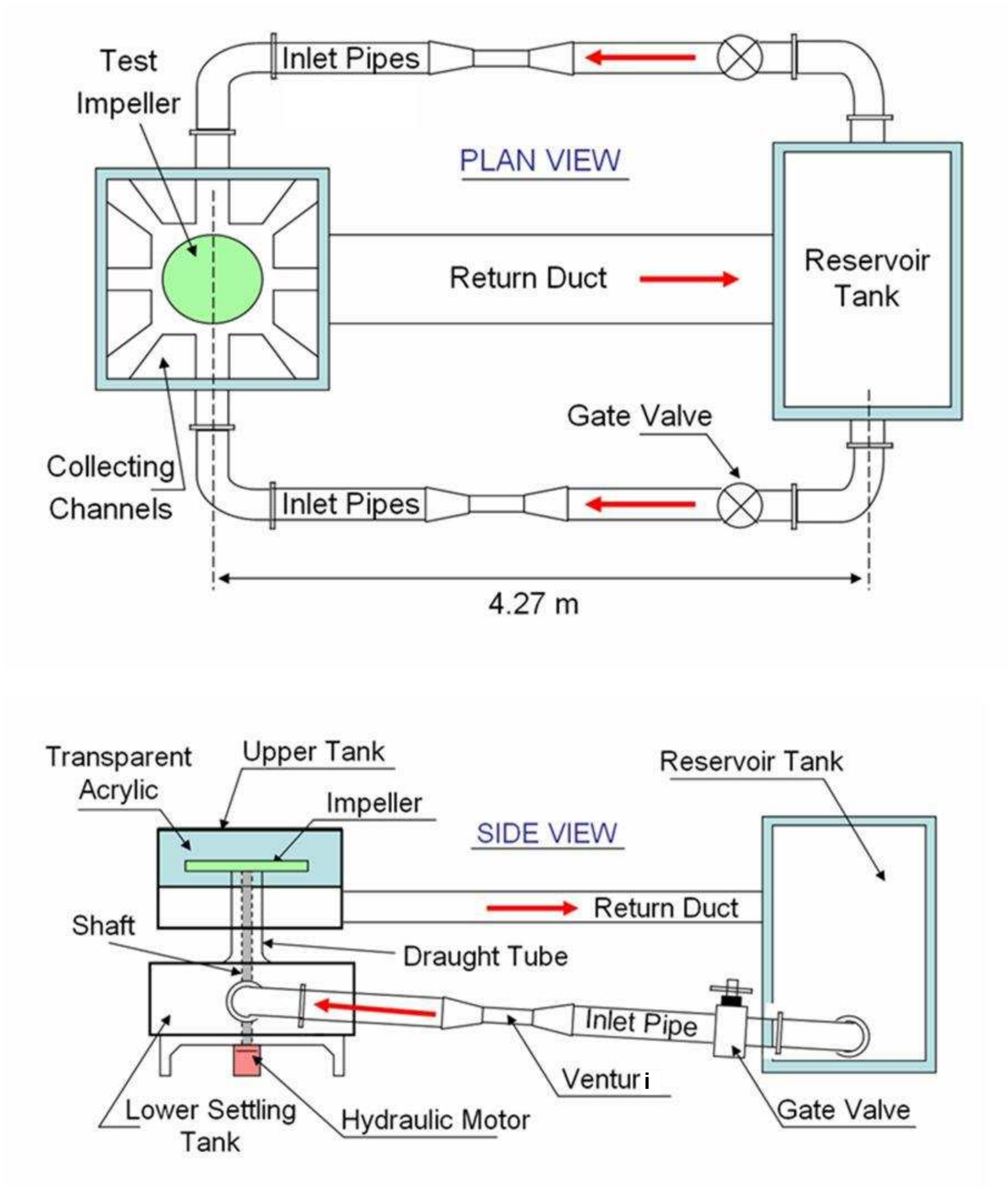

Figure 2.1: Plan and side view of the experiment test rig

tank through a vertical draught tube using the test impeller. The impeller is connected to a hydraulic pump mounted below the lower settling tank using a shaft. There is no volute used around the test impeller. The rotational speed generated by the hydraulic motor can be controlled by a manual controller that varies the flow of the oil pumped to the hydraulic motor. The upper tank is fabricated from transparent acrylic sheets that facilitate the penetration of laser light for visualization purposes. The water goes back from the upper tank (outlet of the impeller) to the reservoir tank through a rectangular duct. Both the upper tank and the reservoir tank are open to the atmosphere. The water flow rate is controlled using a gate valve installed on each inlet pipe. Assuming leaks in this closed circuit system are prevented, the water and the seeding particles used for PIV visualization purposes are conserved. A detailed explanation of the supporting instruments used will be presented in section 2.2.2.

To summarize the water cycle in the experimental rig, the water flows from the reservoir tank through the two inlet pipes to the lower settling tank and then it is drawn from the lower settling tank through the draught tube into the inlets of the impeller channels and pumped out to the upper tank before it goes back to the reservoir tank through the rectangular return duct.

2.2 Test Impeller Design and Manufacturing

A new 8-blade, backward swept radial impeller was manufactured for this research. The test impeller was entirely manufactured using acrylic sheets to facilitate flow measurement and visualization inside all the channels. A similar impeller design was used in Hesse [25], Onwuama [26] and Behseta [27]. To maintain a blade angle of 30 degrees from the tangent of impeller rotation through out the whole channel (log spiral blade profile), Equation 2.1 was used:

$$\Theta(r) = 99.12 \ln(\frac{r}{0.114}) \tag{2.1}$$

where Θ = is the angle between radius r and inlet radius r_1 and r = radius as shown in Figure 2.2.

The impeller's blades were not tilted relative to the impeller axis. The impeller geometry and blade dimensions are shown in Figure 2.3 and summarized in Table 2.1 below.

Inlet radius, r_1	111 mm
Outlet radius, r_2	248 mm
Shrouded inner radius, r_s	124 mm
Inlet blade height, b_1	25.1 mm
Outlet blade height, b_2	19.5 mm
Shrouded blade height, b_s	21.9 mm
Blade thickness, t_b	6 mm
Number of blades, Z	8
Inlet blade angle, β_1	30 °
Outlet blade angle, β_2	30 °
Blade rake	0 °
Hub thickness, t_1	13 mm
Shroud thickness, t_2	10 mm

Table 2.1: Impeller geometry and dimensions

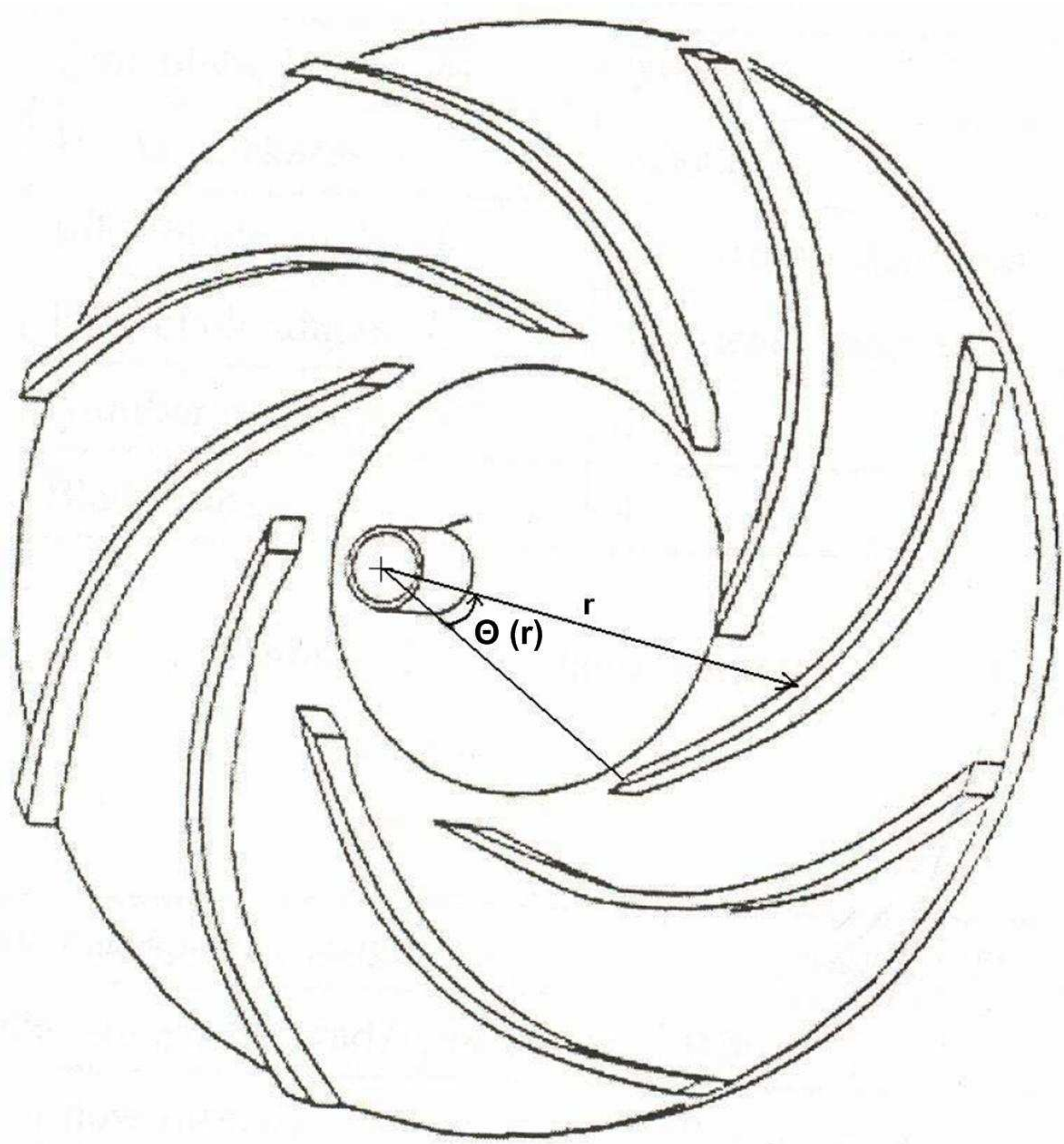

Figure 2.2: Schematic of the impeller blades [27]

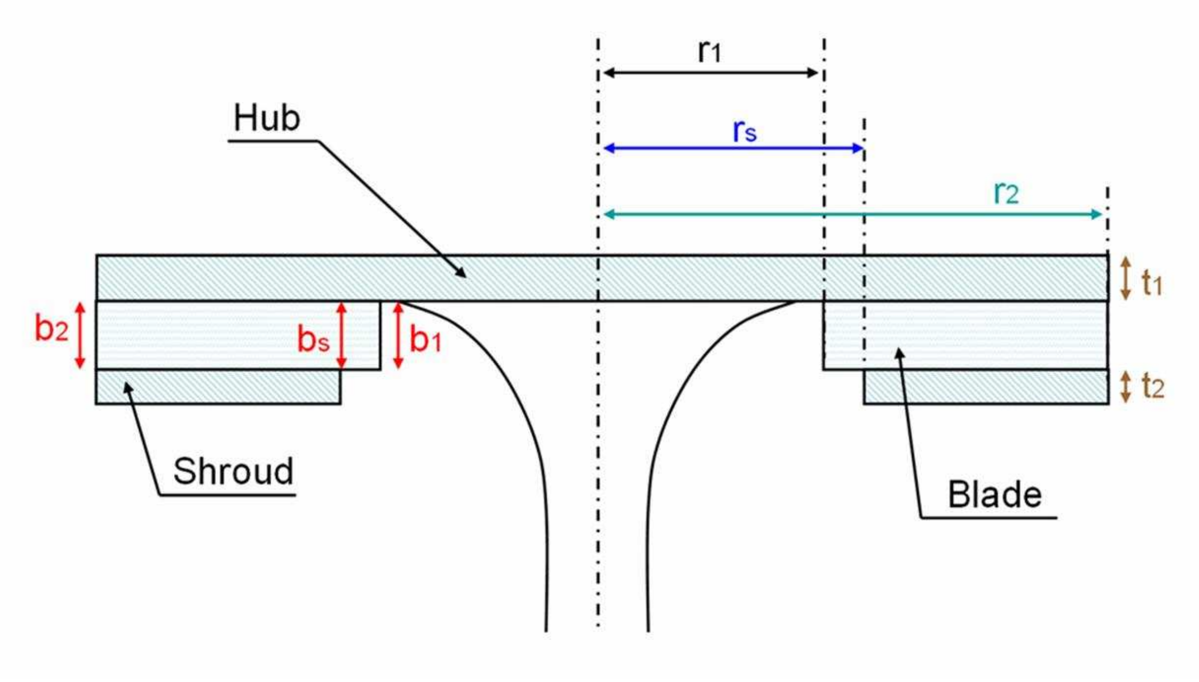

Figure 2.3: Schematic of the test impeller dimensions

2.2.1 Manufacturing of The Test Impeller

Equation 2.1 was plotted in AutoCad to generate a one to one scale drawing. The drawing was programmed into a CNC cutting machine and an acrylic sheet was cut with the same diameter, r_2, shown in Table 2.1 above. Grooves were made in the hub using CNC machine for the blades to be inserted. The shroud was fixed into a milling machine and machined from the start of the shroud, r_s, to the end, r_2, according to the shroud height, b_s, and outlet height, b_2. After that, the same grooves made in the hub were cut in the shroud plate. A wooden mold was fabricated with the same blade profile presented by Equation 2.1 in which heated acrylic strips of thickness 6 mm were bent against the wooden mold to form the blades curvature. The blades were glued into the grooves of the hub and the shroud was painted black to prevent any light reflection. A transition metal piece that slides on the shaft was connected to the impeller hub using four countersunk bolts. A picture of the impeller is shown in Figure 2.4 below. Metal shims were installed between the transition piece and the hub to balance the impeller and remove any vibration.

Figure 2.4: A picture of the newly constructed test impeller

2.2.2 Impeller Performance Measurement and Dimensionless Parameters

The test impeller was manufactured specifically for this research study. It differs from the previous impellers used in Hesse [25], Onwuama [26] and Behseta [27] in terms of the material used but not the general design. However, manufacturing differences might cause the performance of this impeller to be different from the previous ones. For this reason, it was essential to determine the impeller performance by conducting several test runs at a rotational speed of 150 rpm to find the following:

- flow rate through the impeller (Q),
- the total head output the impeller would produce (H) and
- the hydraulic torque in terms measured (T) and tare torque(T_{tare}).

To calculate the impeller efficiency the following equation is used:

$$\eta = \frac{\text{Output Power}}{\text{Input Power}} \times 100\% = \frac{\rho g H Q}{(T - T_{\text{tare}})\omega} \times 100\% \tag{2.2}$$

where η = the impeller efficiency,

ρ = the fluid density,

H = the head across the impeller,

Q = the flow rate,

T = measured torques,

T_{tare} = tare torque,

and ω = angular velocity.

The dimensional parameters of the impeller are calculated using the following formulas:

$$\text{Flow coefficient:}\varphi = \frac{Q}{b_2(\pi D_2 - Zt_b)} \times \frac{1}{r_2\omega} \tag{2.3}$$

$$\text{Head coefficient:}\psi = \frac{gH}{r_2^2\omega^2} \tag{2.4}$$

$$\text{Specific speed:}N_s = \frac{\omega\sqrt{Q}}{(gH)^{0.75}} \tag{2.5}$$

where b_2 = blade height at the exit,

D_2 = impeller exit diameter,

Z = number of blades,

t_b = thickness of the blade.

2.2.2.1 Flow Rate

To eliminate any inconsistency, especially at low flow rates, two transit-time ultrasonic flow meters (Uniflow 990 System) were used to measure the flow rate across the impeller. These ultrasonic flow meters are non intrusive clamped-on type that are clamped on the two inlet pipes (Figure 2.5).

These ultrasonic flow meters consist of four major parts, which are the mounting tracks,

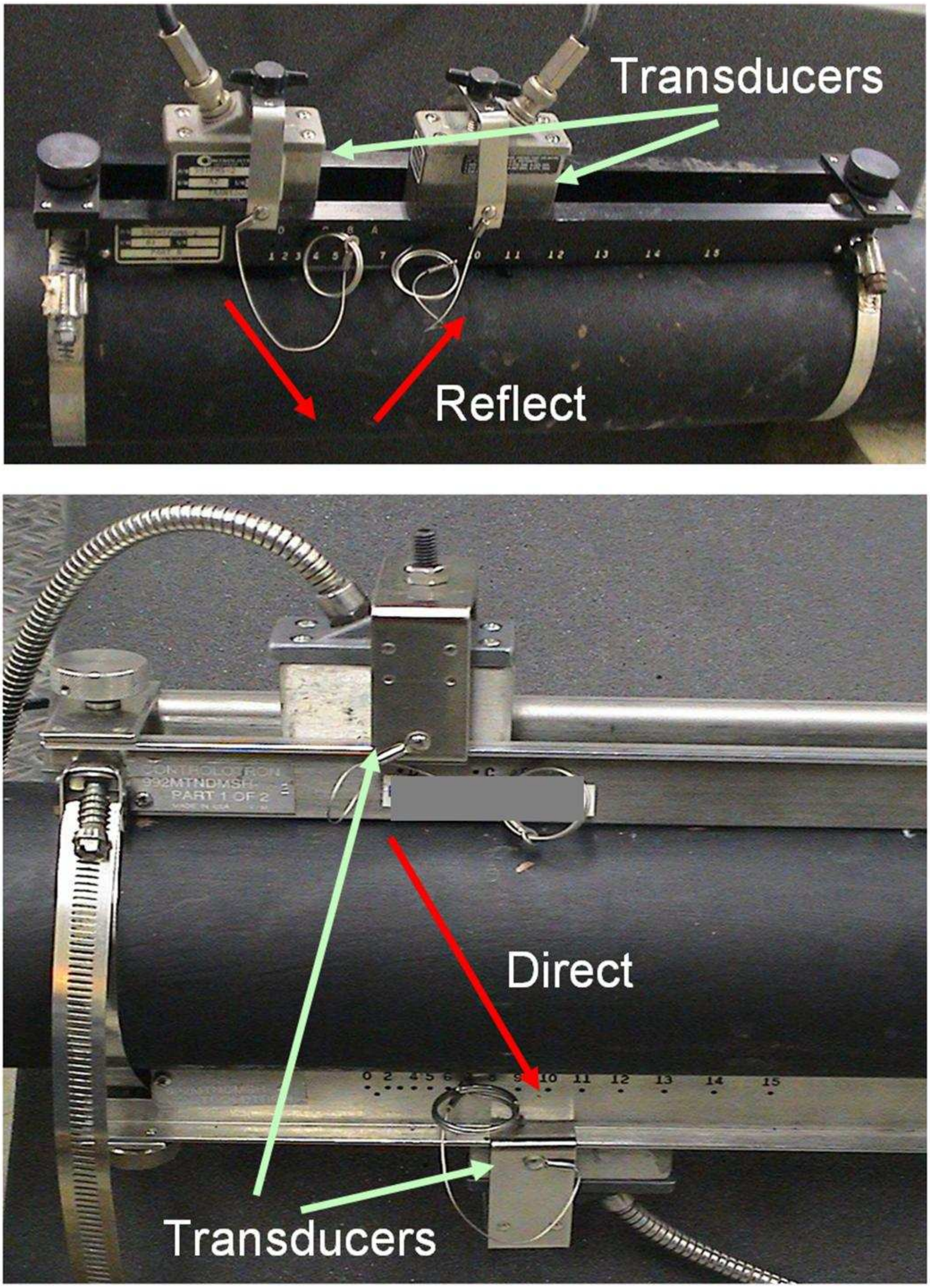

Figure 2.5: Ultrasonic flow meters components configuration

two transducers, the flow display computer and a handheld control and display unit. The basic principle of measuring the flow of the medium is based on the phenomenon that a sound wave changes frequency when it is reflected by moving discontinuities in a flowing liquid. In this system, one transducer sends an ultrasonic sound wave to the other transducer through the inlet pipe with flowing liquid inside, and the discontinuities in the liquid reflect the ultrasonic wave with a slightly different frequency, which is directly proportional to the rate of flow of the liquid [28].

The mounting tracks are fixed to the pipe using adjustable metal rings. This location in the experiment rig should not be directly after a pipe fitting that might cause disturbances in the water flow and so affect the flow rate readings. The transducers are installed in the mounting tracks at certain positions that are determined by testing the acoustic wave signal using the ultrasonic flow computer. The contact surfaces between the transducers and the pipe's outer wall must be very clean and free of debris to avoid any discontinuities which are not part of the flow where a special industrial gel is applied to improve signal transmission. The transducer could be connected either in direct or reflect layout as shown in Figure 2.5. The result of the wave frequency that passes between the transducers is sent through coaxial cables to the flow display computer. This computer consists of a power circuit with an on/off switch that provides a series of serial data port modules with the required power to calculate the signal received from the coaxial cable through connection sockets and then displays the desired information on an LCD digital display. A schematic of the flow display computer is shown in Figure 2.6.

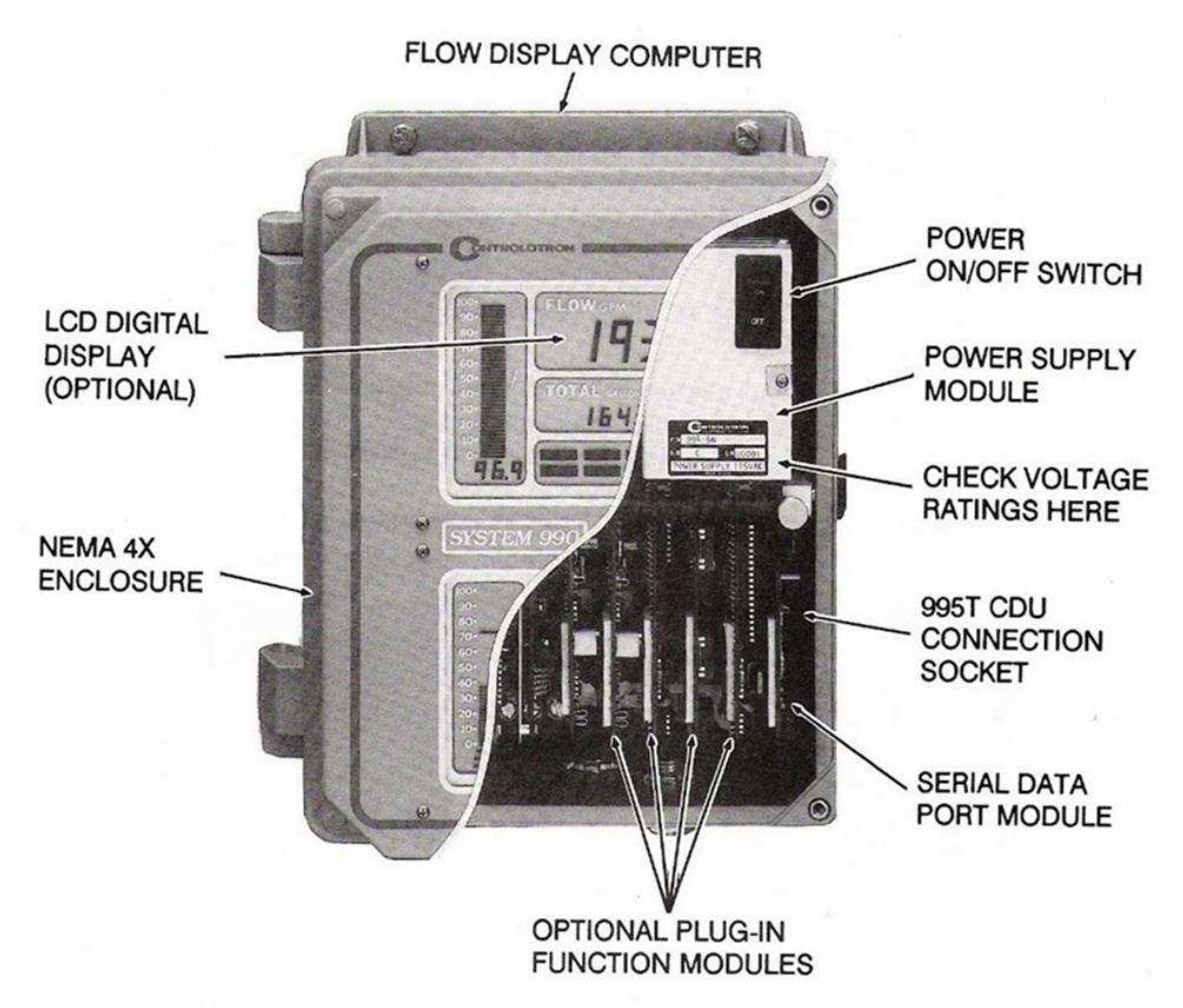

Figure 2.6: Uniflow ultrasonic flowmeter flow display computer [28]

The flow display computer calculates the flow rate in liter per second and produces a pre-scaled signal that ranges from 4mA to 20mA which is collected in a data acquisition system. The handheld control and display consists of a keypad that allows the user to enter the site parameters and also an LCD screen with four lines of alphanumeric display that serves as a data display. Figure 2.7 shows a schematic of the handheld control and display unit.

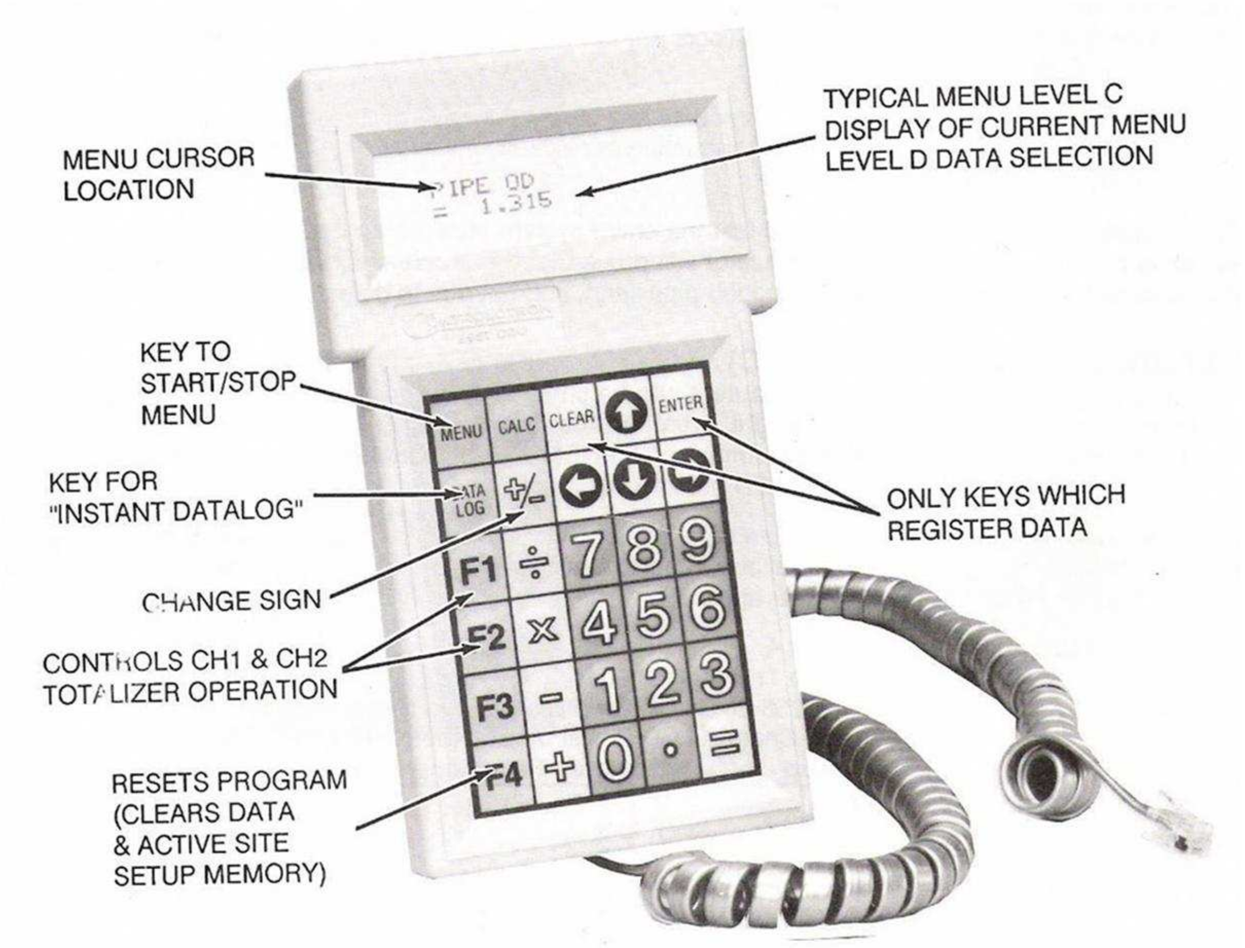

Figure 2.7: Uniflow ultrasonic flowmeter hand held control and display unit [28]

Different information could be entered using the handheld control and display unit based on the user's application. The data entered in the flow display computer for our case is presented in Table 2.2

Pipe Material	Copper
Pipe outside diameter	101.6 mm
Pipe wall thickness	1.91 mm
Liquid used	Water
Liquid temperature	20 C / 68 F
Sound velocity in copper	$2,270.76$ m / s
Sound velocity in Water	$1,482$ m / s

Table 2.2: Fluid parameters used to calculate the water flow using the ultrasonic flowmeter

The sound wave velocity is calculated using the ultrasonic computer and installed in the system's input as required. According to the instrument operation manual, the flow rate measured using these ultrasonic flow meters has a maximum uncertainty of 3%. For more information refer to the brief operation manual [28].

2.2.2.2 Head Rise

To calculate the head rise across the test impeller, the stagnation pressure at the inlet and outlet of the impeller should be measured. Two Kiel probes were used: in the draught tube (inlet) and downstream of the impeller channel (outlet). The position of the Kiel probe inside the draught tube was adjusted horizontally to read the highest pressure while the other Kiel probe at the discharge of the impeller was also adjusted to record the highest pressure. A picture of the Kiel Probe is shown in Figure 2.8.

The differential pressure from both probes was measured using a Validyne 5 psi range

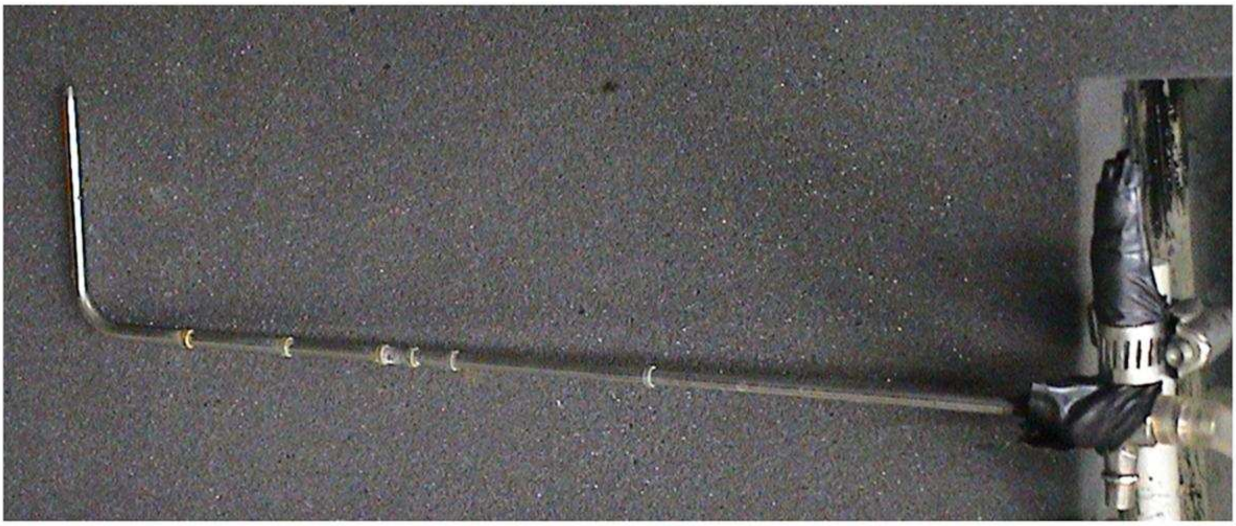

Figure 2.8: Kiel probe used to measure the pressure across the impeller

pressure transducer. This pressure transducer consists of a stainless steel diaphragm clamped between two stainless steel blocks. Each block has a pressure port, to which the Kiel probe is connected, linking to a cavity which has a coil assembly embedded on its surface. With no differential pressure, the diaphragm is centred with equal gaps between the two embedded coils and providing equal reluctances. If a pressure in one of the ports is higher than the other, the diaphragm deflects towards the cavity with the lower pressure decreasing the gap between it and the embedded coil in the low pressure cavity. As a result, the inductance of that coil is increased as the magnetic reluctance varies with the deflection of the diaphragm. This inductance variation in the transducer's coils is transmitted through an AC bridge circuit to give an AC signal output that varies linearly with the variation of the diaphragm deflection that represents the pressure difference between the two cavities [29]. A schematic and a picture of the pressure transducer are shown in Figure 2.9.

The AC output signal goes from the Validyne pressure transducer to a Validyne model

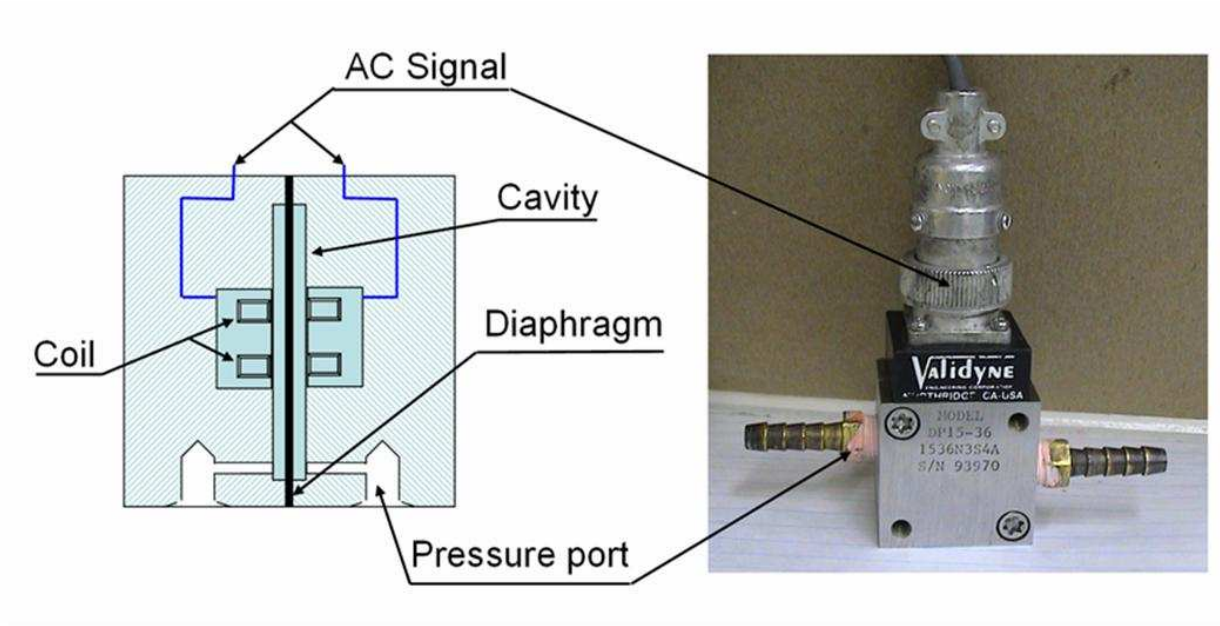

Figure 2.9: A schematic and picture of the Validyne pressure transducer used

CD15 sine wave carrier demodulator. This device helps in calibrating the pressure transducer and also produces a voltage signal that is proportional to the reluctance variation sent to the data acquisition system. To calibrate the pressure transducer, one of the pressure ports is connected to an air source that is linked to a Heise pressure gauge and water column pressure gauge at the same time (Figure 2.10). The signal output of the pressure transducer is sent to the data acquisition system through the Validyne demodulator where the reading of the output signal in the data acquisition monitor is calibrated using the knobs in the demodulator [30]. Figure 2.10 shows a schematic diagram of the instrument connections to calibrate the pressure transducers.

According to the instrument operation manual, the differential pressure is measured using this pressure transducer with an uncertainty of 0.25%. The calibration results are shown in section 2.3.

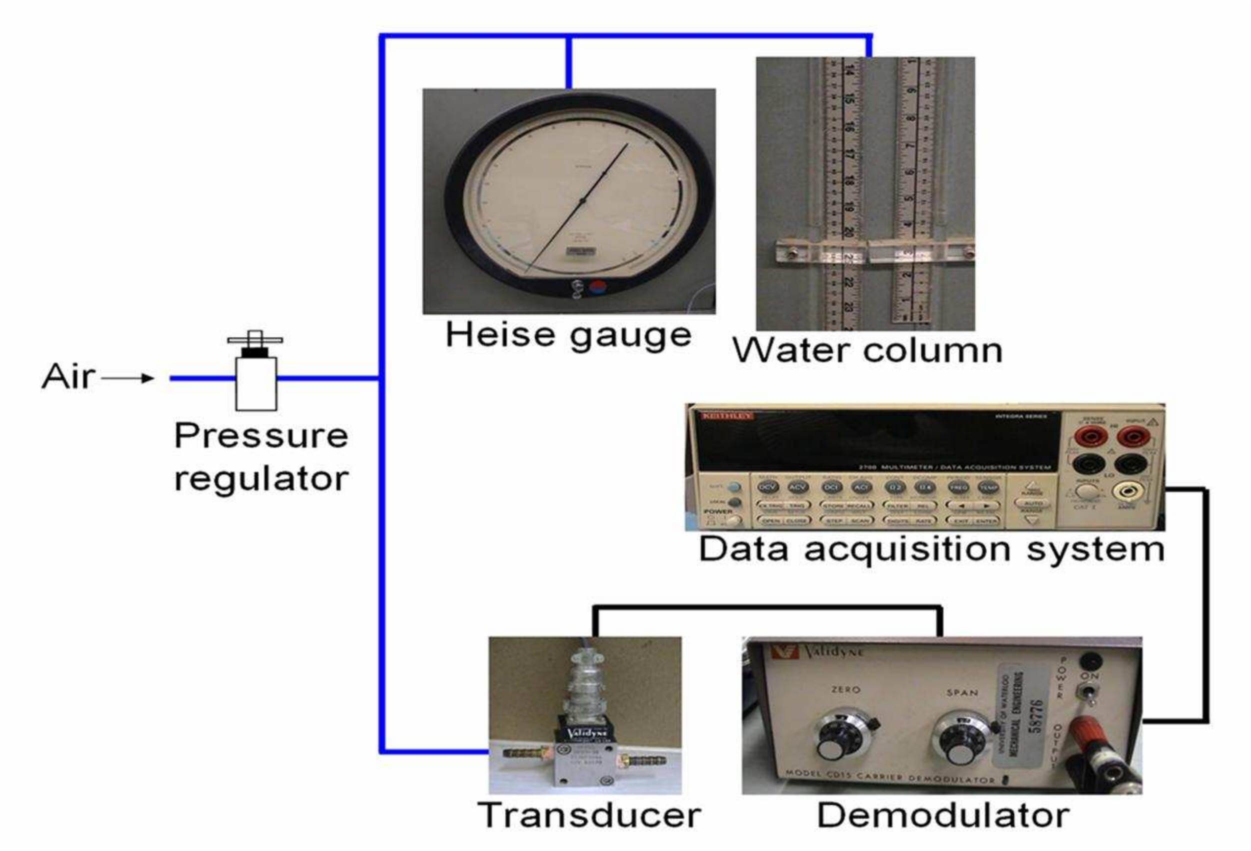

Figure 2.10: A schematic of the pressure transducer calibration process

2.2.2.3 Torque

To be able to calculate the impeller efficiency, the required torque to rotate the impeller was measured using a torque meter (Lebow Products Inc.) mounted between the hydraulic motor and the shaft connected to the impeller. The output of this torque meter is sent to a Daytronic (model-3278) strain gauge indicator. Also an integral speed sensor installed in the torque meter provides the rotational speed of the impeller [31]. When the hydraulic motor applies a rotational force on one end of the torque meter, the surface of the shaft at that end of the torque meter will experience compression and tension that are different from the other end which is connected to the shaft and so the impeller strain gauge elements mounted on the torque meter shaft will be able to detect the deflection in both ends of the sensor shaft and its output signal is converted to a modulated pulse frequency as shown in Figure 2.11.

To ensure accuracy in the measured torque, the torque meter is calibrated before installing it using weights, the Daytronic strain gauge indicator and the data acquisition system. An arm with known length is clamped on the torque meter shaft and weights are applied to one side in which the torque in (in.lb) was calculated by multiplying the arm length in inches by the weight added to that arm. With each weight increment, the torque reading changes in the Daytronic strain gauge indicator to represent it. Following the manufacturer's procedure and using the knobs on the Daytronic strain gauge indicator [31], the measured reading on the indicator represents the calculated torque applied to the arm. The output of the strain gauge indicator is sent in terms of voltages to the data acquisition system which will be used to form a linear relation between the voltage and the torque measured. The calibration

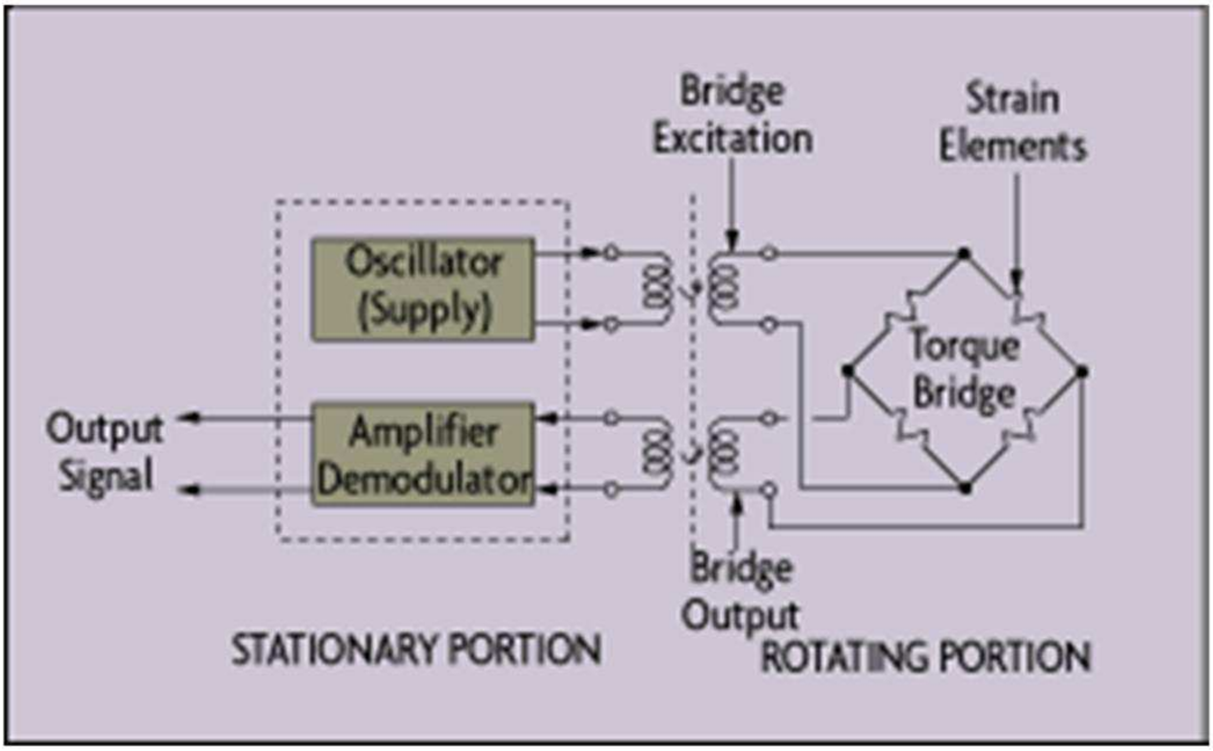

Figure 2.11: Electric circuit configuration of the torque meter used [31]

results are shown in section 2.3.

Usually, the torque reading that is measured when the experiment is running is stored for the desired rotational speed at every flow rate. This torque includes the load from the frictional forces applied to the rotational part and the load exerted on the impeller due to the water passing through it. The torque of interest is the one that is a result only from the water hydraulic forces. For this reason, the tare torque, which is a result of the frictional forces, is measured first without having any water flowing through the impeller. This tare torque is subtracted from the total torque when the water is flowing through the impeller passages to get the value that will give the impeller efficiency. According to the instrument operation manual, the torque is measured using this torque meter with an uncertainty of 1.0%.

2.2.2.4 Data Acquisition System

The flow rate data, the torque meter reading, the differential pressure readings are read and collected by the Keithley data acquisition system [32] which is controlled using XLINX software.

2.3 Instrument Calibration

Measuring instruments used in this research are all calibrated before any data acquisition occurred.

2.3.1 Pressure Transducer Calibration

The pressure transducer was connected to a Heise pressure gauge and its electrical signal output was connected eventually to the data acquisition system in order to be calibrated (Figure 2.10). Before the calibration took place, the pressure transducer was dismantled and the diaphragm was cleaned using alcohol to remove any dirt sticking on it from previous experiments. The calibration results are represented in Table 2.3 and Figure 2.12.

Heise (kPa)	Heise (PSI)	Keithley (V)
28.8	4.2	4.27
26.5	3.8	3.91
24.5	3.6	3.62
22.2	3.2	3.27
20.2	2.9	2.98
18.0	2.6	2.66
16.0	2.3	2.36
14.1	2.0	2.08
12.1	1.8	1.79
10.1	1.5	1.48
8.1	1.2	1.19
6.0	0.9	0.89
4.0	0.6	0.59

Table 2.3: Pressure transducer calibration results

During the experimental run, the data acquisition system is set to take 100 differential pressure reading in terms of voltage for each flow rate at 150 rpm. The above chart could be represented by the following equation:

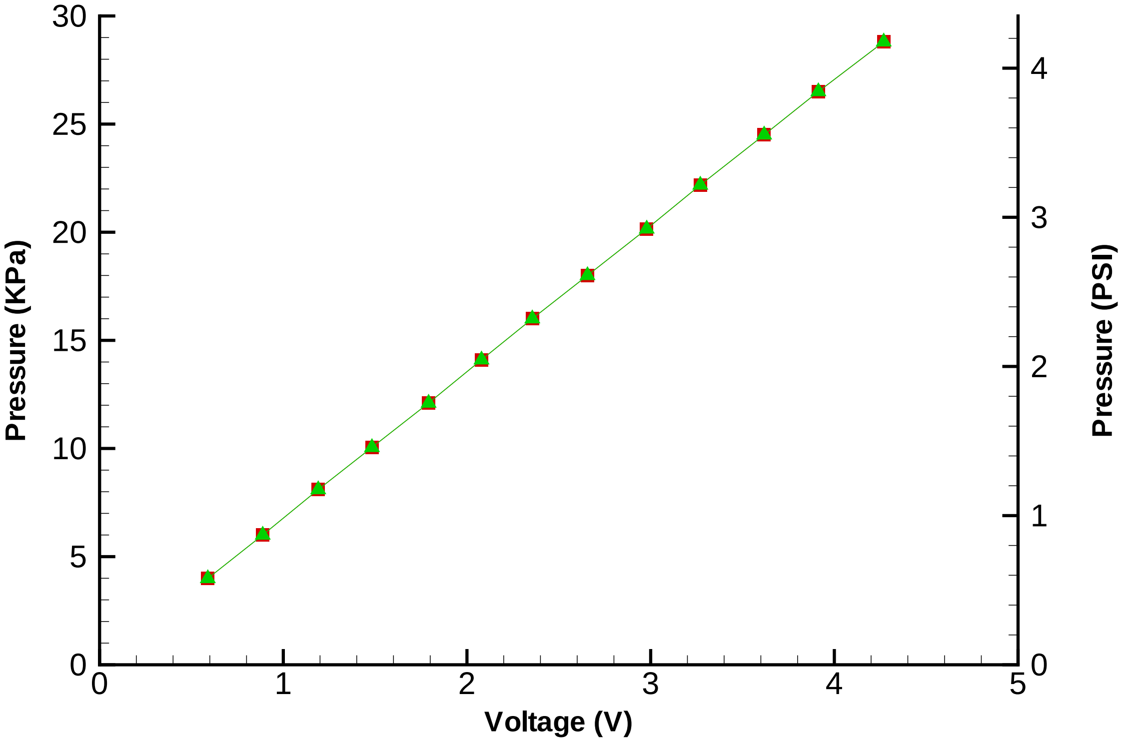

Figure 2.12: Pressure transducer calibration readings (pressure vs. voltage)

$$\text{Differential Pressure} = (\text{Voltage Reading} \times 0.978) + 0.01 \tag{2.6}$$

An average of 100 voltage readings is used to calculate the differential pressure.

2.3.2 Torque Meter Calibration

The torque meter is calibrated to represent the torque measured. Comparison between the calculated torque as a result of adding weight to a 0.305 m long arm and the measured weight in the Daytronic strain gauge indicator and the voltage displayed in the data acquisition system is shown in Table 2.4 and Figure 2.13.

During the experiment run, the data acquisition system is set to take 100 torque readings in terms of voltage for each flow rate at 150 rpm. The above chart could be represented by the following equation:

$$\text{Torque} = (\text{Voltage reading} \times 39.95) - 0.096 \tag{2.7}$$

An average of 100 voltage readings is used to calculate the resultant torque.

Weight (lb)	Calculated Torque (in.lb)	Torque Reading (in.lb)	Voltage Reading (V)
5.16	62.09	62.10	1.56
6.71	80.72	80.80	2.02
7.49	90.05	90.20	2.26
8.26	99.38	99.54	2.49
9.04	108.72	108.90	2.73
9.43	113.38	113.64	2.85
9.82	118.05	118.30	2.96
10.10	121.44	121.70	3.05
10.38	124.84	125.14	3.14
10.49	126.16	126.50	3.17
10.60	127.48	127.80	3.20
10.62	127.75	128.10	3.21
10.73	129.07	129.40	3.24
10.84	130.39	130.70	3.28

Table 2.4: Torque meter calibration results

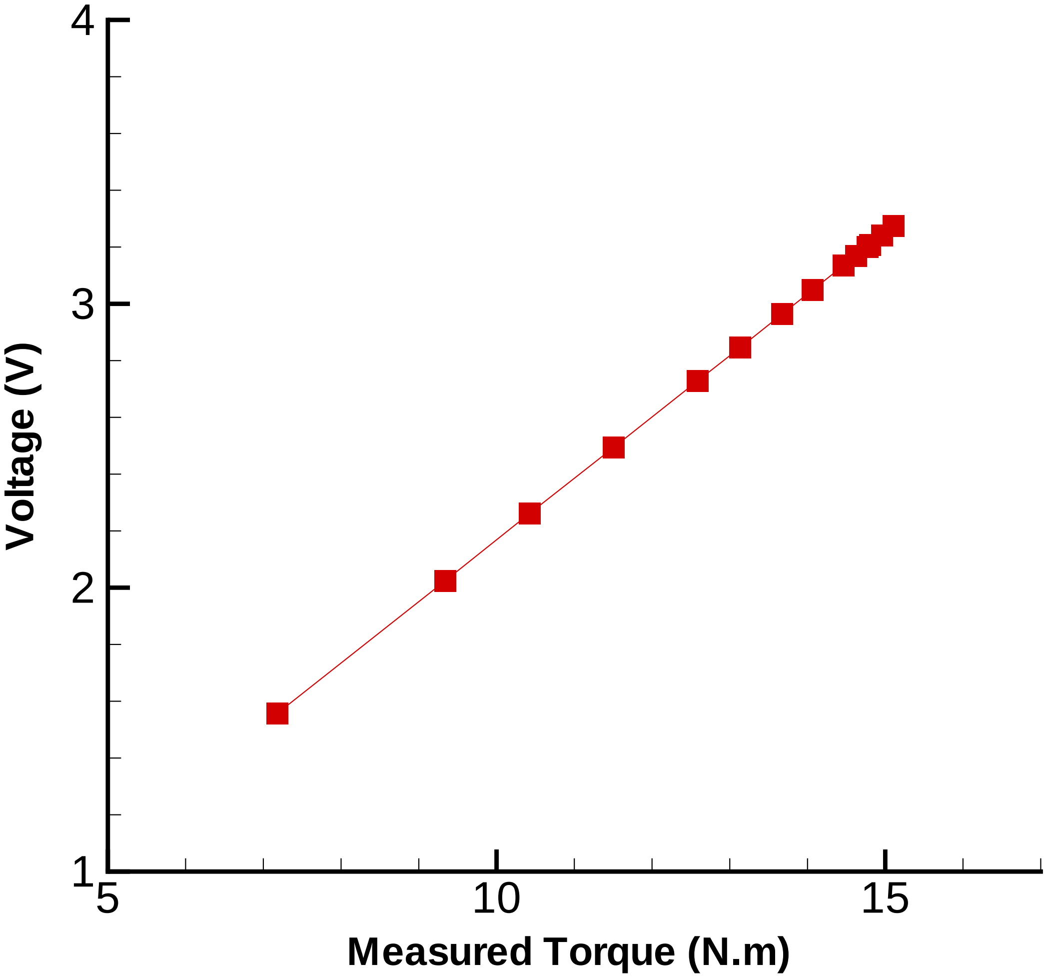

Figure 2.13: Torque meter calibration readings (voltage vs. torque)

2.4 Experimental Apparatus Repairs and Modifications

The experimental rig used in this study is over 35 years old and several repairs were done to restore it to working condition. The reservoir tank was cleaned and cuts in the inner insulation lining were fixed to prevent water leakage. Also, the flanges connecting the inlet pipes to the reservoir tank were leaking and a waterproof silicon sealant was used to stop the leakage.

Several cracks and pinholes were sealed using special waterproof putty material and also a waterproof aluminum tape. The corroded parts (rods and bolts) in the upper tank, where the impeller is installed, were replaced by stainless steel and copper parts. To reduce the effect of water vortices that result from the impeller rotation, two transparent acrylic sheets were manufactured to fit the upper tank with holes to allow the installation of the trigger plate and vent water bubbles that accumulate under the acrylic sheets. Also a wiper was installed under the acrylic sheet that facilitates the removal of tiny water bubbles that stick under the sheet without interrupting the experiment run. An acrylic mask to allow camera images to be taken clearly was manufactured. The upper tank transparent side walls and the acrylic cover were treated with special acrylic cleaners and scratch removers that would improve the visibility through the sheets and increase their smoothness in an effort to reduce bubbles or particles sticking on them during the experiment run. Metal arms to hold the camera in a vertical position above the test impeller were also manufactured. Sliding holders were installed to smoothly slide the camera to the desired positions over the impeller. Pressure taps upstream and downstream of the impeller were also cleaned and new water tubes were installed. A new trigger sensor was fabricated to ensure a signal is received whenever the trigger passes through the trigger sensor at every impeller revolution.

Foam sheets were cut and installed just under the impeller to prevent any water leakage (recirculation) from the test location back to the inlet of the impeller. Also at the top of the draught tube, thin sheets of foam were installed to smoothen the flow movement from the draught tube to the inlets of the impeller channels. A pressure tap installed in the draught tube was cleaned and leakage in its neck was stopped using silicon sealant.

The torque meter was dismantled and cleaned before installing it is again. The whole shaft was dismantled and its original 35-year-old bearings were changed. Also one of the shaft stages was slipping over the other due to the worn out coupling metal ring. A new one was fabricated and fixed in place of the old one and the shaft was fixed back in place. The hydraulic motor was dismantled from the experimental rig and cleaned and fixed again at the bottom of the rig.

Chapter 3

Experimental Technique

The particle image velocimetry (PIV) technique is used in this study to measure the relative velocity components inside the centrifugal pump impeller described in Chapter 2. An overview of the technique and the theory behind it, the steps of applying it, the uncertainties involved, and the experimental setup will be discussed in this chapter.

3.1 Introduction

To improve the efficiency in turbomachines such as centrifugal pumps, clear understanding of the flow phenomena occurring within the rotating passages is required through precise measurement of the flow velocity components in the whole passage. Particle Image Velocimetry (PIV) facilitates the measurement of instantaneous velocity vectors in the flow field of interest.

When using PIV, finding the velocity vectors of the flow of interest depends on precisely determining the distance traveled by an illuminated particle in a specific time interval where successive frames of the flow are captured at the beginning and end of this time. This means that the velocity of each particle is represented by the following equation:

$$V_{\text{particle}} = \frac{\Delta d}{\Delta t} \tag{3.1}$$

where V_{particle} is the particle velocity representing the actual flow velocity. Particle displacement is represented by Δd and Δt is the time interval over which the particle displacement occurs.

3.2 PIV Properties and Process Steps

The following points support the general understanding of the PIV technique and its unique features.

- Unlike other flow measurement techniques that require the installation of some instruments, like pressure probes, which might disturb the flow field, PIV is a non-intrusive technique that depends on the visual accessibility to the field of flow to be studied. This ensures results free of disturbance especially at the locations close to equipment walls where the flow may be disturbed by the presence of probes. However, having transparent walls to apply PIV requires manufacturing of test equipment out of transparent material like glass and acrylic which is challenging and costly in some cases.
- The PIV technique measures the velocity of a fluid indirectly by measuring the velocity

of the tracer particles seeded in the flow. This requires proper representation of the flow by those particles to avoid any velocity lag between the flow and the particle velocities [33].

- Unlike other techniques that provide velocity measurement of the flow at a single point, PIV is a whole field technique where velocity measurements of large parts of the flow field are the results of analyzing the captured images of those parts.
- In the standard PIV technique, the illumination of a plane of the flow means that only two (in-plane) components of the velocity vector can be determined. This will be the technique used in this research. Other techniques such as dual-plane, holographic recording PIV [33] and stereographic imaging techniques [34] can measure the third component of the velocity vector.

The steps of applying the PIV technique in different experiments including the one in this research are demonstrated in Figure 3.1.

First, the flow to be examined is seeded with the proper particles. Once the flow is seeded, the area of interest is illuminated by a light sheet which is generated usually by a laser and a system of optical components. The duration of the light pulse is very short such that the particle does not move significantly during its exposure to the light pulse. This will produce a stroboscopic effect, freezing the movement of the seeded particles. During the illumination step, the seeded particles scatter the light which is captured by a charge coupled device (CCD) camera. This camera is usually positioned at a right angle to the light sheet and focused to capture images at the plane of interest (Figure 3.2).

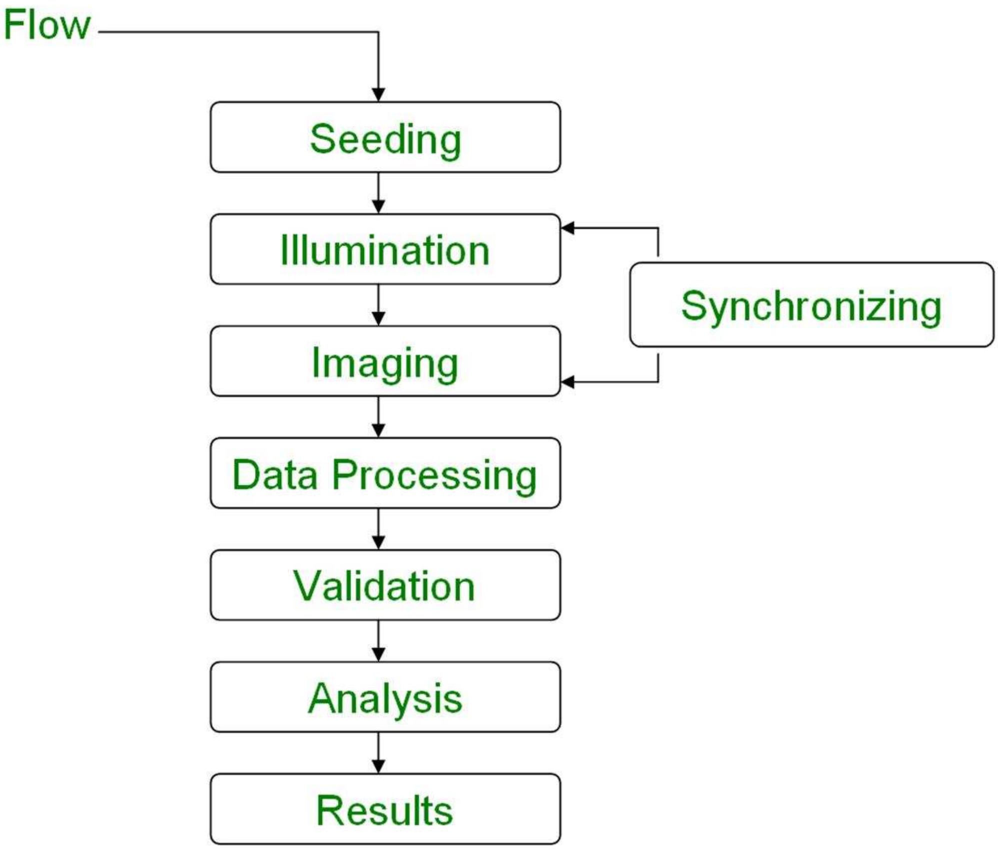

Figure 3.1: PIV process steps

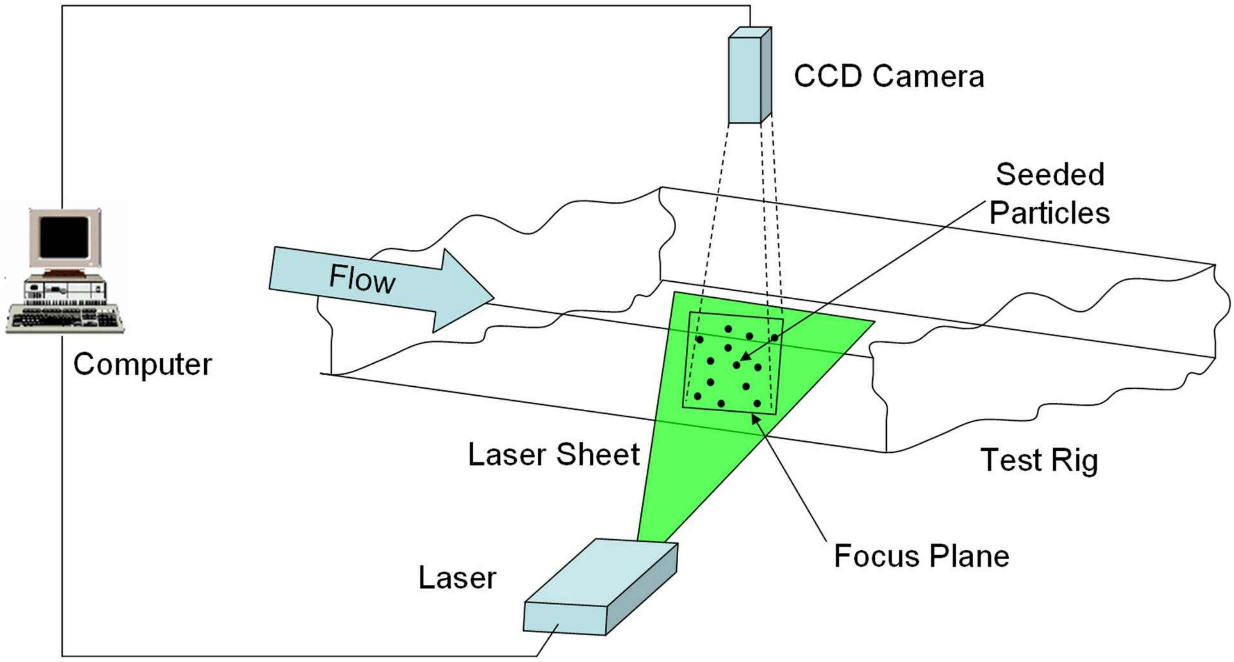

Figure 3.2: General PIV setup

The CCD camera and the pulsing light sheet, or laser bursts, are synchronized using an internal processor. As a result of this, two different images, A and B, of the flow field are captured which are separated by a pre-selected time Δt represented by equation (3.1). Usually the particles' positions appear as light specks (white dots) on a dark background in each image. Figure 3.3 shows a typical PIV image (1008 x 1018 pixels) of a blade separating two impeller channels.

The camera images are divided into smaller square regions known as interrogation areas. The correlation takes place between images A and B for the same interrogation area to give a vector representing the particle displacement. This process is repeated for all the interrogation areas to give a vector map of the particle displacements in the whole flow field which represents the fluid flow. Figure 3.4 represents a typical PIV vector map.

Figure 3.3: Typical PIV image of seeded flow

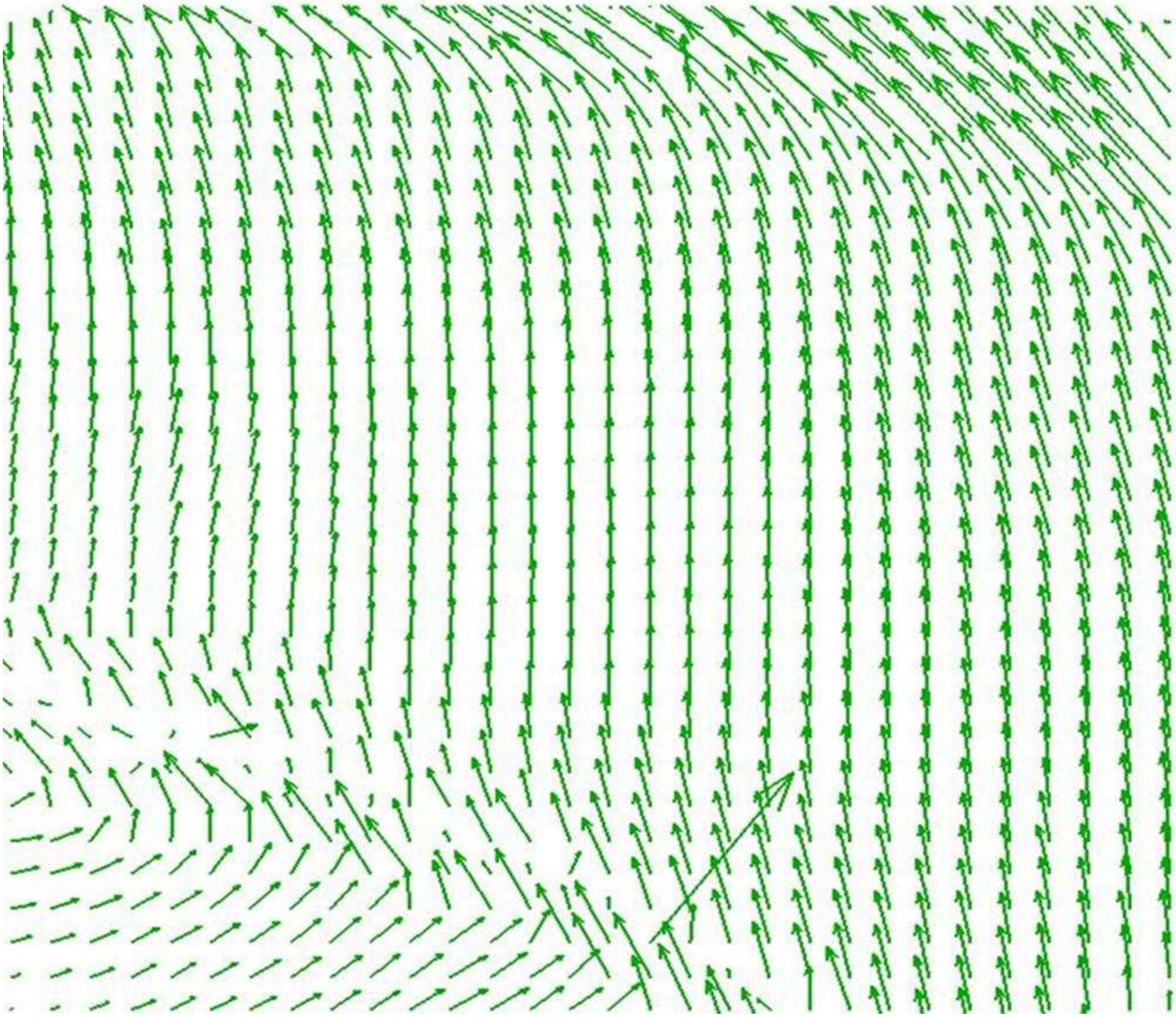

Figure 3.4: Typical PIV vector map

The cross-correlation process is usually carried out using Fast Fourier Transform (FFT) techniques. The FFT calculation is carried out in the software program and will give results regardless of the quality of the images taken. For this reason, it is important to validate the vector map that results from the cross-correlation. Outliers are incorrect vectors resulting from noise peaks in the correlation function. Validation methods used in PIV will recognize the valid vectors. The validation methods reject and remove outliers and may substitute them with other vectors based on the method used. Different validation methods exist such as peak height ratio, velocity range and moving average validation which will be discussed later in this chapter.

3.3 PIV Components

As noticed from the previous discussion of the PIV technique, the basic components of a two dimensional PIV system are as follows:

- tracer particles (seeding),
- laser (illumination),
- cameras (imaging),
- synchronization and image processing, and
- result validation.

3.3.1 Tracer Particles

The PIV technique estimates flow velocity by measuring the velocity of the seeded particles.Thus, an adequate representation of the fluid by the tracer particles is required. Generally, the motion of tracer particles are affected by:

- relative density of particles,
- particle size,
- particle shape,
- concentration of particles in the fluid, and
- body forces.

3.3.1.1 Relative Densities

The tracer particles' density must be very close to the density of the fluid particle to avoid incorrect velocity representation. For instance, if the particles' density is lower than the fluid density, the tracer particles will float and drift upwards affected by buoyancy forces. In contrast, if the tracer particles are too heavy and higher in density than the fluid, they will sink in the fluid due to gravitational forces. In both cases, a misleading representation of the fluid flow is the result.

Assuming spherical particles in a viscous fluid at a very low particle Reynolds number, the velocity encountered due to the gravitational forces (U_g) from Stokes drag law is represented by Raffel [33] as follows:

$$U_g = d_p^2 \frac{\rho_p - \rho}{18\mu} g \tag{3.2}$$

where d_p is the diameter of the tracer particles, g is the acceleration due to gravity, μ is the dynamic viscosity of the fluid, ρ is the density of the fluid particles and ρ_p is the tracer particle's density.

The velocity lag which is the difference between the tracer particle velocity, U_p, and the fluid velocity, U_f, could be represented as follows:

$$U_s = U_p - U_f = d_p^2 \frac{\rho_p - \rho}{18\mu} a \tag{3.3}$$

where a is the particle acceleration [33].

3.3.1.2 Particle Size

Boundaries for choosing the proper particle size exist. From equations (3.2) and (3.3) above, it is noticed that smaller particles will improve the overall particle tracking by reducing the gravitationally induced velocity and the velocity lag. This means the smaller the tracer particles the better the velocity representation. However, the light scattering capability of the tracer particles is affected as the particles become smaller which affects the quality of images acquired. Raffel [33] considered the light scattered by tracer particles as a function of the ratio of the refractive index of the particles to that of the surrounding medium, the particles size, shape and orientation.

Melling [35] represented the light scattering capability of tracer particles as a function of both the total scattered power P_s and the laser intensity I_0 to give the scattering cross section C_s where

$$C_s = \frac{P_s}{I_0} \tag{3.4}$$

Figure 3.5 demonstrates the effect of the ratio of particle diameter d_p to the laser wave length λ on the scattering cross section for spherical particles with refractive index equal to 1.6. The refractive index of a medium is a measure of how much the speed of light (or other waves such as sound waves) is reduced inside the medium.

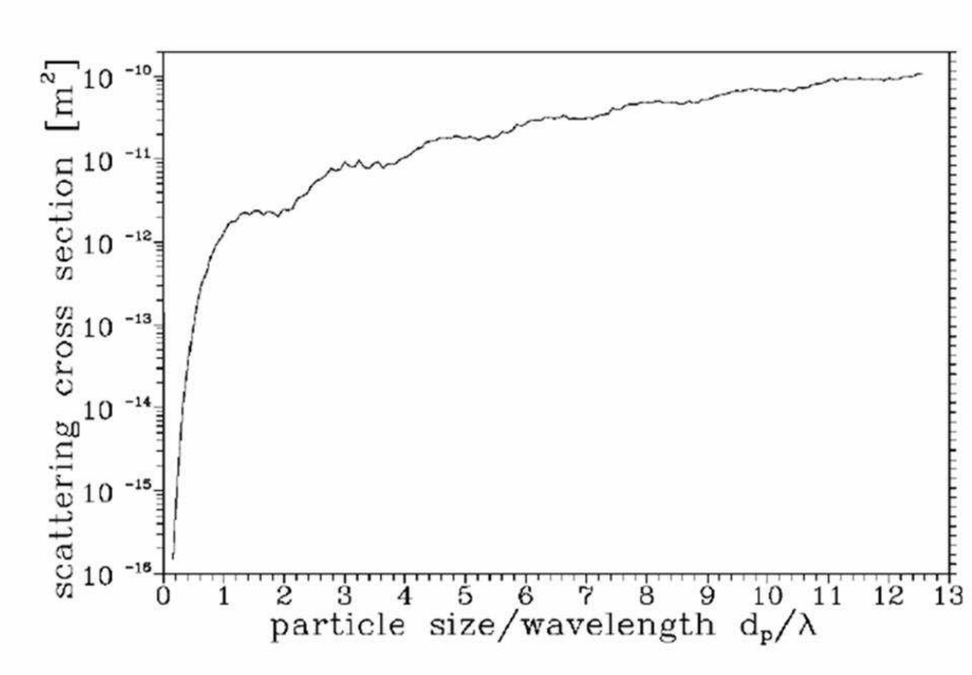

Figure 3.5: The effect of the ratio of particle diameter to the laser wave length on the scattering cross section for spherical particles [35]

It can be noticed from Figure 3.5 that the bigger the particle the better the scattering cross section. It must be mentioned that choosing the proper size of the particles to increase the image intensity is more effective and economical than increasing the laser power. To reduce the drag between the tracer particles and the fluid, spherical particles are normally used in PIV application.

Other general properties of tracer particles that must be considered [36]:

- non toxic, non corrosive, non abrasive,
- conveniently generated,
- cheap,
- non-volatile,
- chemically inactive, and
- clean

The particles used in this experiment were provided free of charge in support of this research by Eliokem Inc. and are called Pliolite VT. They are white in color and spherical with a specific gravity of 1.03. The particles were put through a sieve to ensure a size that ranges from 75 to 105 μm. This size satisfies the recommendation provided by Dantec, the manufacturer of the PIV systems used [36].

3.3.2 Illumination

Illuminating the seeded particles is an essential part of the PIV technique. Illuminating the particle in the PIV technique is done either by using two pulsing laser beams or a continuous wave laser such as argon-ion. Usually, in both types, a system of optical lenses is used to generate a sheet of laser light. In this research, a laser system consisting of two pulsing beams from a double-cavity Q-switched Nd:YAG laser were combined and formed into pulsing light sheets using optics. More information on advantages and disadvantages of both types is provided in the Dantec User Manual [36]. Figure 3.6 shows the layout of the double cavity laser used.

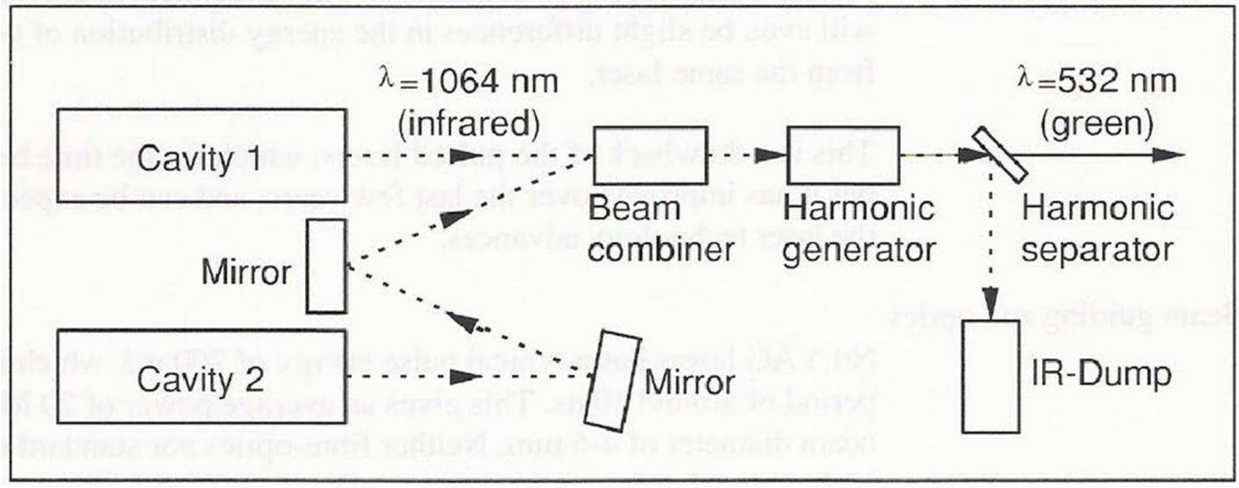

Figure 3.6: Layout of a double cavity laser [36]

The importance of the illumination part of the PIV technique could be appreciated through the following points:

- the single laser pulse duration should be small so that the particle does not move significantly during its exposure,
- the time between the two laser pulses should be controlled precisely to be short enough that the flow field and so the traced particle does not move significantly.

- the laser intensity must be high enough to produce scattered light from the particles that could be recorded on the camera.

The pulse duration of the Nd:YAG laser used is 5 ns. This exposure time will not allow the particle to shift its position in the image while it is taken. The frequency at which pairs of the laser pulses can be emitted is 15 Hz. The Nd:YAG laser was capable of producing two laser pulses with 120 mJ/pulse at a wavelength of 532 nm. The thickness of the laser sheet and its position inside the test impeller was determined by using a fabricated metal piece to fit inside the impeller channel with a 1 mm thick horizontal line placed exactly in the mid height of the entrance.

3.3.3 Imaging

In the PIV technique, the camera was used to capture the initial and final position of the particles in which a displacement vector from these positions can be processed. Special cameras are usually used in the PIV technique that are capable of taking multiple frames of the flow field separated by a very short time interval. A charged coupled device (CCD) camera was used in this research to take images of the flow since it provides an instantaneous digital signal of the image map of seeding particle positions. These CCD cameras are comprised of arrays of pixels that are charged when detecting the light reflected off the particles. The more pixels in the CCD image frame, the more the details of the flow in that frame are available. Usually, the background of the images appears darker while charged pixels that represent particles produce white pixels in the captured image. In cross correlation, the image of the first position of the seeded particles are recorded in the first frame of the camera which will be advanced by a selected time (Δt) and then, the final positions of the particles are recorded in the second camera frame [36].

In this research a Kodak Megaplus 1K x 1K CCD camera was used to capture images of the seeded particles. An 18-108 mm and $F/2.5$ zoom lens manufactured by Navitar Inc. was fixed to the camera. To reduce the noise from the ambient lab light, a 532nm optical notch filter was used to allow only laser wavelength light to charge the camera pixels.

Using cross correlation algorithms, the two frames were processed to obtain the vector map of the flow field. Each vector produced in the vector map represents an area in the image that is called an interrogation area. The interrogation area is measured by the number of pixels of each side which is determined by the researcher. Typical interrogation area sizes are 32 x 32 and 64 x 64. The smaller the number of pixels that represents the dimensions of the interrogation area, more vectors represent the vector map and so more details of the flow field are captured. Also, the researcher can specify the overlap between the interrogation areas which will enable the program to capture particles that might move into or out of the interrogation area. A 50 percent overlapping means that for a 32 pixel interrogation area, the cross correlation will be repeated every 16 pixels (Figure 3.7).

In this research, the images captured had 1008 rows of pixels and 1018 columns of pixels. Each interrogation area was chosen to be 32 x 32 pixels. The overlapping of the interrogation area was 50 percent. To get the number of the vectors produced in the image, the following formula was used:

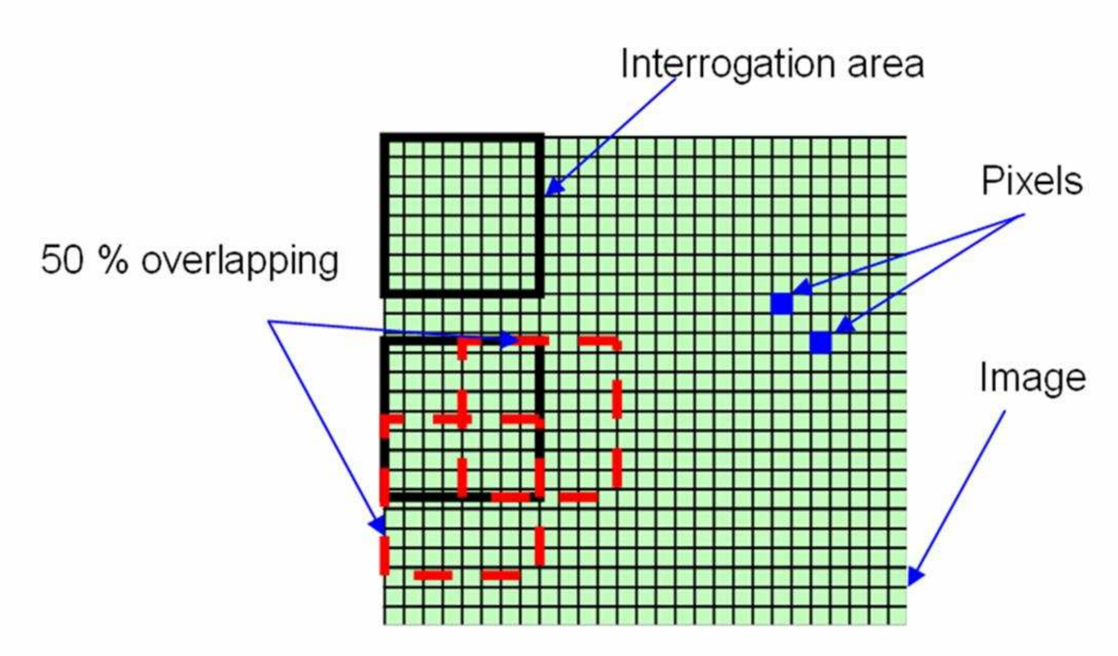

Figure 3.7: Interrogation area and overlapping inside capture PIV image

$$\text{size of image} = \frac{\text{number of pixels in CCD row}}{(1 - \%\ \text{overlapping} \times L_{\text{int}})} \times \frac{\text{number of pixels in CCD column}}{(1 - \%\ \text{overlapping} \times L_{\text{int}})} \quad (3.5)$$

where L_{int} is the dimension of the interrogation area in pixels.

Applying the above equation to this research means that each image of the flow field is represented by a vector map that consists of 62 x 62 vectors.

A scale factor, M, which is the number of pixels in the image that represent a measured unit in the flow field must be determined and used in the cross correlation program to generate valid results. Figure 3.8 shows the image recording steps from the flow field to the pixel of each interrogation area [36].

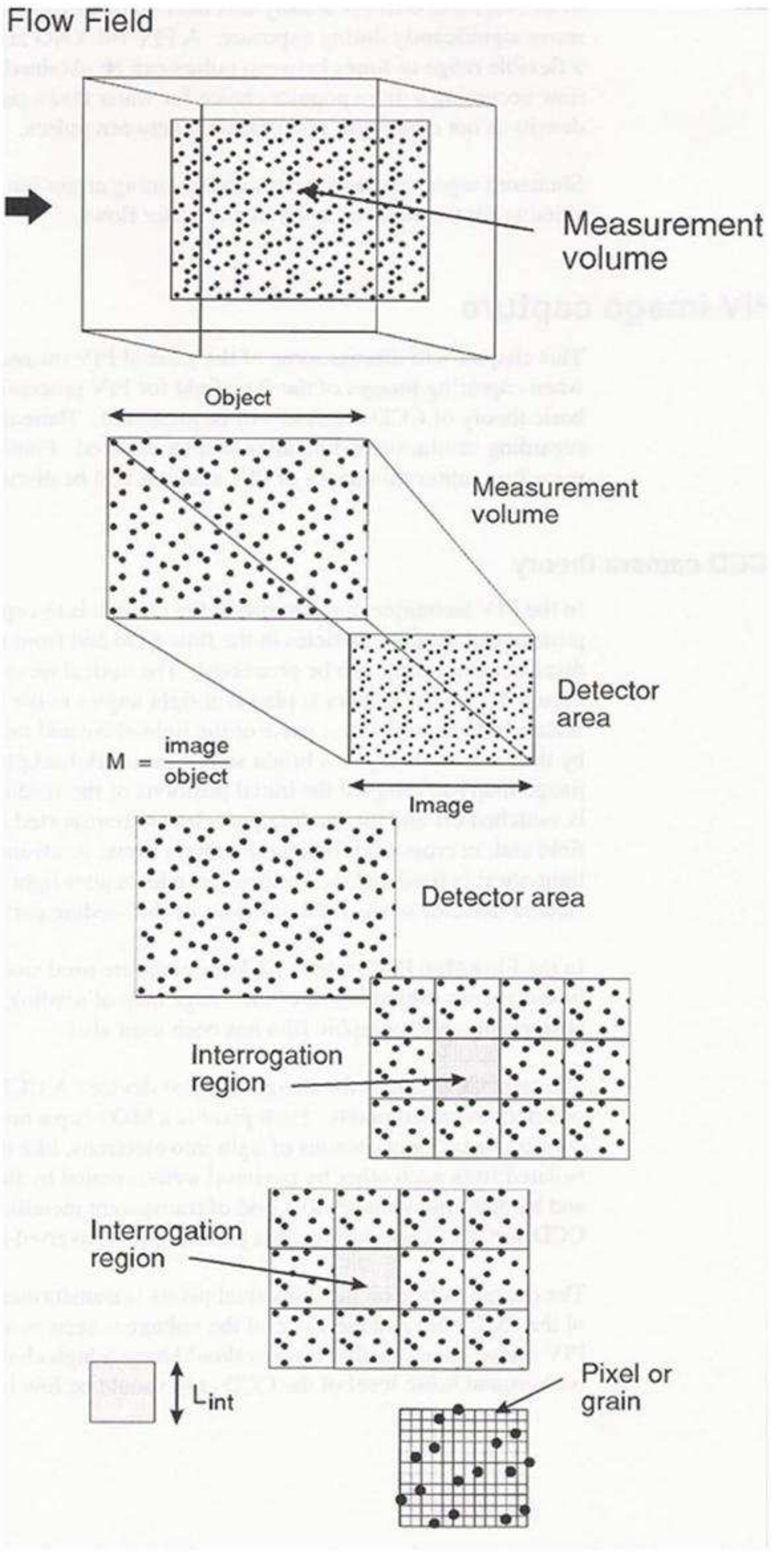

Figure 3.8: Image processing steps in the PIV process [36]

3.3.4 Synchronization and Image Processing

The laser beam and the camera are synchronized to work at the same time in order to capture images of the seeded particles at their initial and final positions. Usually, a computer is used to do this step in which the researcher determines the required time between the two images. In this research, this step was done using a FlowMap PIV 2100 processor.

Image processing using cross correlation algorithms was done using Flow Manager Program provided by Dantec [36]. The captured images are divided into smaller interrogation areas where cross correlation using FFT techniques takes place. Figure 3.9 shows the numerical processing flowchart of the PIV images.

Usually the velocity represented by each vector is calculate using the following equation

$$\vec{V} = M\frac{\vec{d}}{t} \tag{3.6}$$

where M is the scale factor used, $\vec{d}$ is the distance covered in the 2 dimensional plane and t is the time between the initial and final position of the seeded particle.

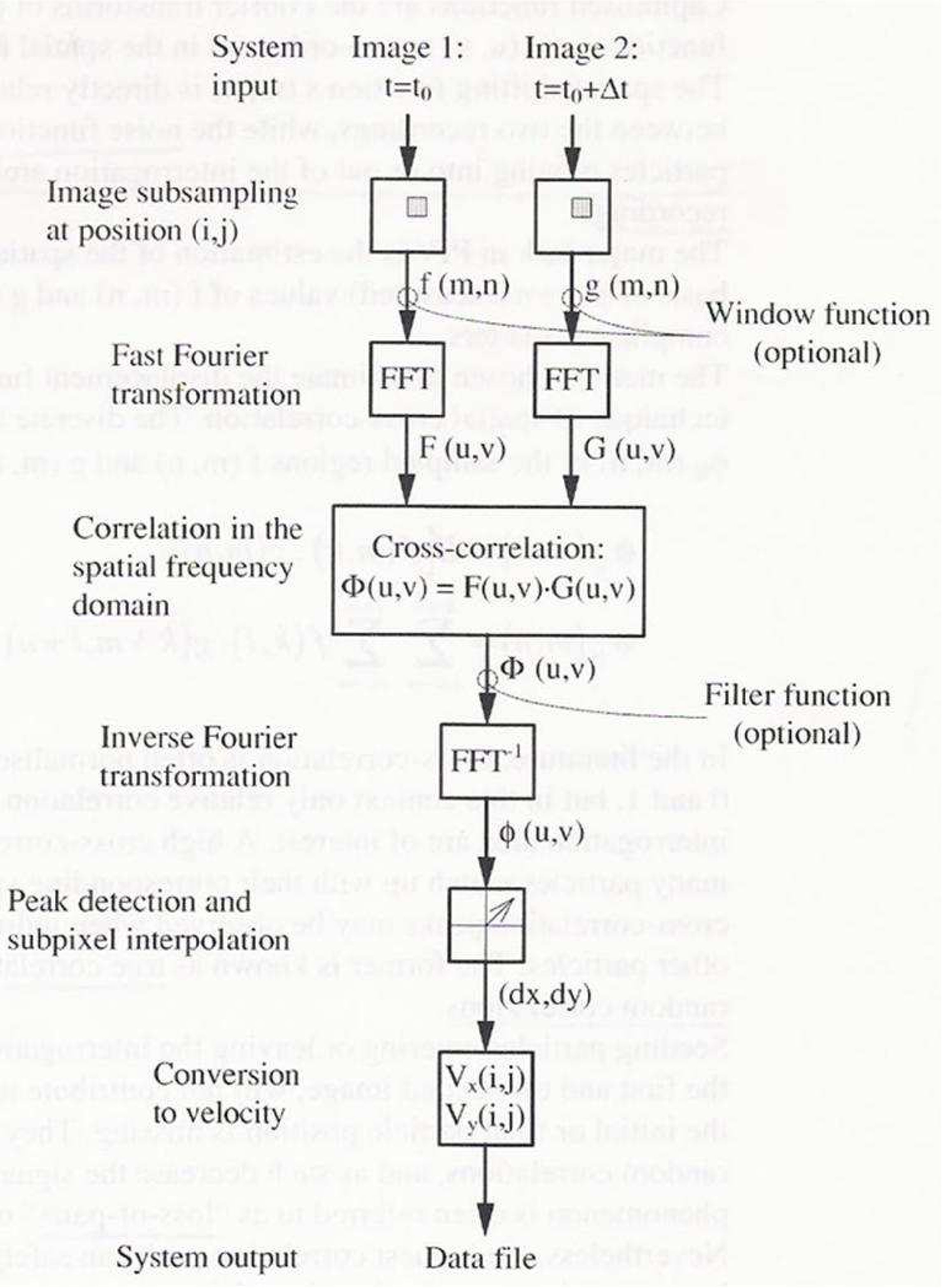

Figure 3.9: Numerical processing flowchart of PIV images using FFT [36]

3.3.5 PIV Validation

Three different methods to validate the results are provided by the Flow Manager Program [36]. These methods are peak height ratio validation, velocity range validation and moving average validation. Outlier vectors are vectors that do not represent the real flow and are either removed or replaced by another vector based on the validation technique used.

In peak height validation the vector that represents each interrogation area is validated based on the value of the peak height in the correlation plane where the vector (particle displacement) is measured. The processor calculates the ratio of the highest peak to the second highest peak in the correlation plane and compares it to a certain value which is know as the detectability criteria [36, 37]. In this method, outliers are removed from the vector map. This method was used in this research study.

In velocity range validation method, vectors are rejected if they fall out of a certain velocity range. The limits of this range are usually determined based on the knowledge of the expected velocity in the location where measurements take place. The velocity limits are considered for x and y axes of the two dimensional plane. There is no substitution of outliers in this method.

Moving average validation method validates vectors based on a comparison between adjacent vectors. In this method, the average of the velocity components in the neighboring interrogation areas is calculated and multiplied by an acceptance factor and then compared with the vector of interest. Outliers in this method are usually replaced by the average of the surrounding vectors in the averaging area.

3.4 Sampling Size

A proper sample size (number of images taken of the flow in this case) is the key in providing an accurate representation of the experiment. In experiments which conditions and parameters do not change significantly, increasing the sample size reduces the differences between the sample and the actual experiment characteristics [38].

In this experiment, the case of the design flow (13.4 L/s) was considered as a steady case where the characteristics of the fluid flow, mainly the primary velocity components' direction and magnitude, do not change significantly. To determine a proper number of images to be captured, samples of 100, 250, 500, 750 and 1000 images were collected. The x component of the relative velocity at those sets of images was compared at 4 random locations in the outlet frame where this analysis took place. In Figure 3.10, the relation between the number of images taken and the effect on the magnitude of the velocity measured is demonstrated. At four randomly selected locations (Figure 3.10 a), b), c) and d)), it was noticed that the velocity magnitude measured in samples of size 100 ,250 and 500 images were changing and oscillating with no clear attenuation to an average value observed. At samples of size 750 and 1000 images, an attenuation was noticed in the magnitudes of the velocity calculated averaging to values falling between those measured from 100, 250 and 500 images samples. Based on these observations, sets of 1000 images were collected for each flow condition of this experiment. Increasing the sample size to more than 1000 images would be very time consuming and expected to produce results close to those found in the sets of 1000 images.

It is important to note that in unsteady flow conditions, such as those of 50%, 40%, 30%

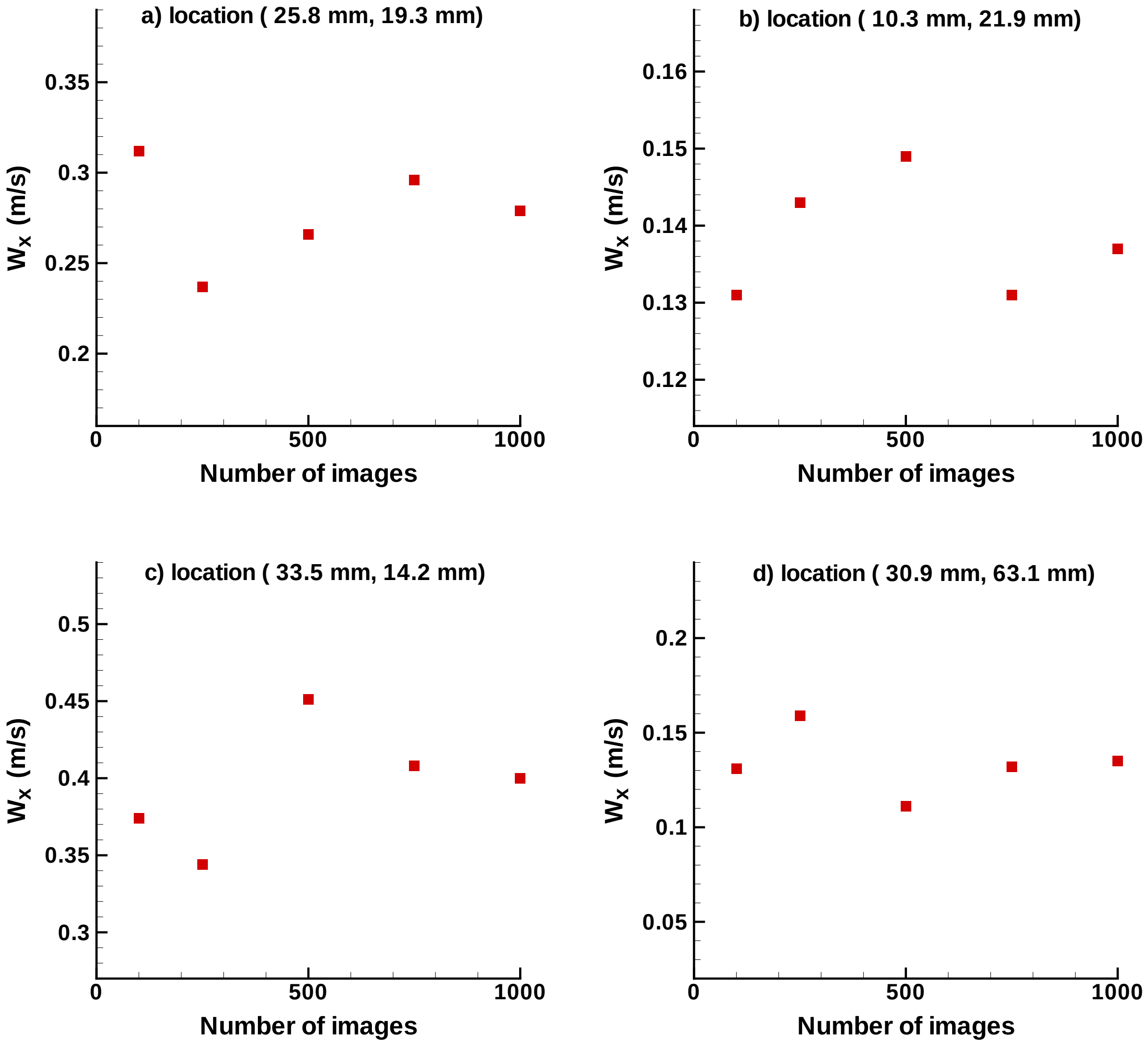

Figure 3.10: Effect of number of images taken on the magnitude of velocity measured

and 25% of the design flow rate, variations in the flow behaviour in terms of relative velocity magnitude, relative velocity direction and locations of vortices and eddies inside the impeller channel are present. This means that averaging larger number of images does not produce representative vector maps of the actual flow behaviour at those low flow rates. Furthermore, single instantaneous images do not represent the flow behaviour except at the time in which that image was taken. This will be demonstrated in section 4.3.2.2 . On the other hand, the general flow pattern and locations where fluctuations in the magnitude of the velocity measured could be noticed as can be seen in turbulence intensities calculations presented in section 4.3.3.

3.5 Errors in The PIV Technique

In the PIV technique, errors in the velocity measurement exist as in every other measurement technique. Several factors contribute to the errors in the velocity measurement which could be expressed in the following equation

$$\text{Error} = V_{\text{mes}} - V_{\text{act}} \tag{3.7}$$

where V_{mes} is the measured velocity using the PIV technique and V_{act} is the actual velocity of the fluid particles.

Particle size contributes to the accuracy of the image captured and so does the processing of those images. If the particle size is too small (smaller in diameter than the width of one pixel) to fully excite and charge one pixel which is the smallest part of the image, the location of this particle will be mis-represented inside the pixel. This will generate an error in calculating the real distance covered and so the velocity at which the particle was traveling. For this reason it is suggested by Boillot and Prasad [39] that the size of the particles used in the experiment should be nearly equal to the width of two pixels. This is clearly demonstrated in Figure 3.11.

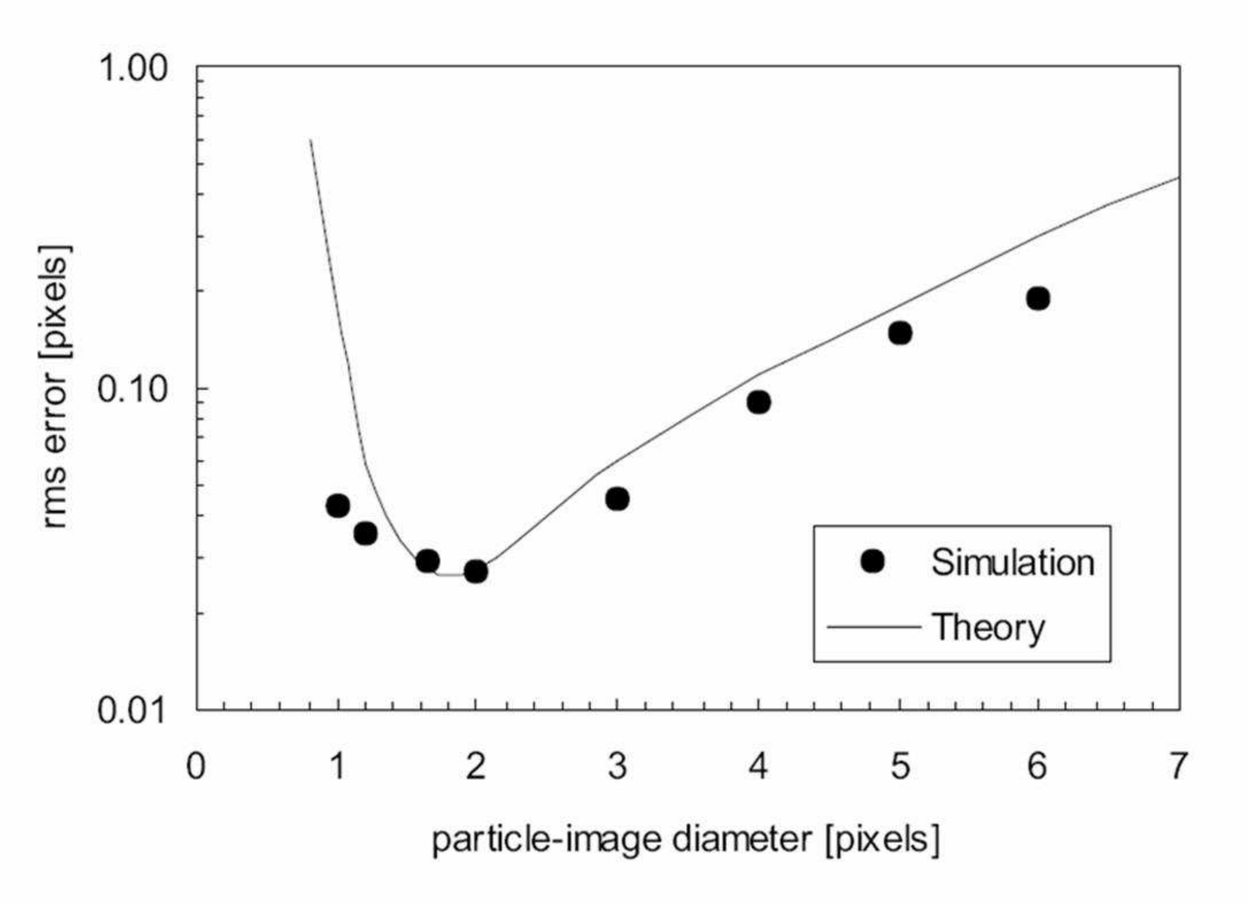

Figure 3.11: Error in determining displacement (in pixels) as a function of the particle image diameter [39]

Selecting relatively large sized particle in the flow decreases the ability of the particle to track the flow behaviour. The response of the particles in turbulent flow is believed to be reduced as the particle size increases as shown in Figure 3.12 [35].

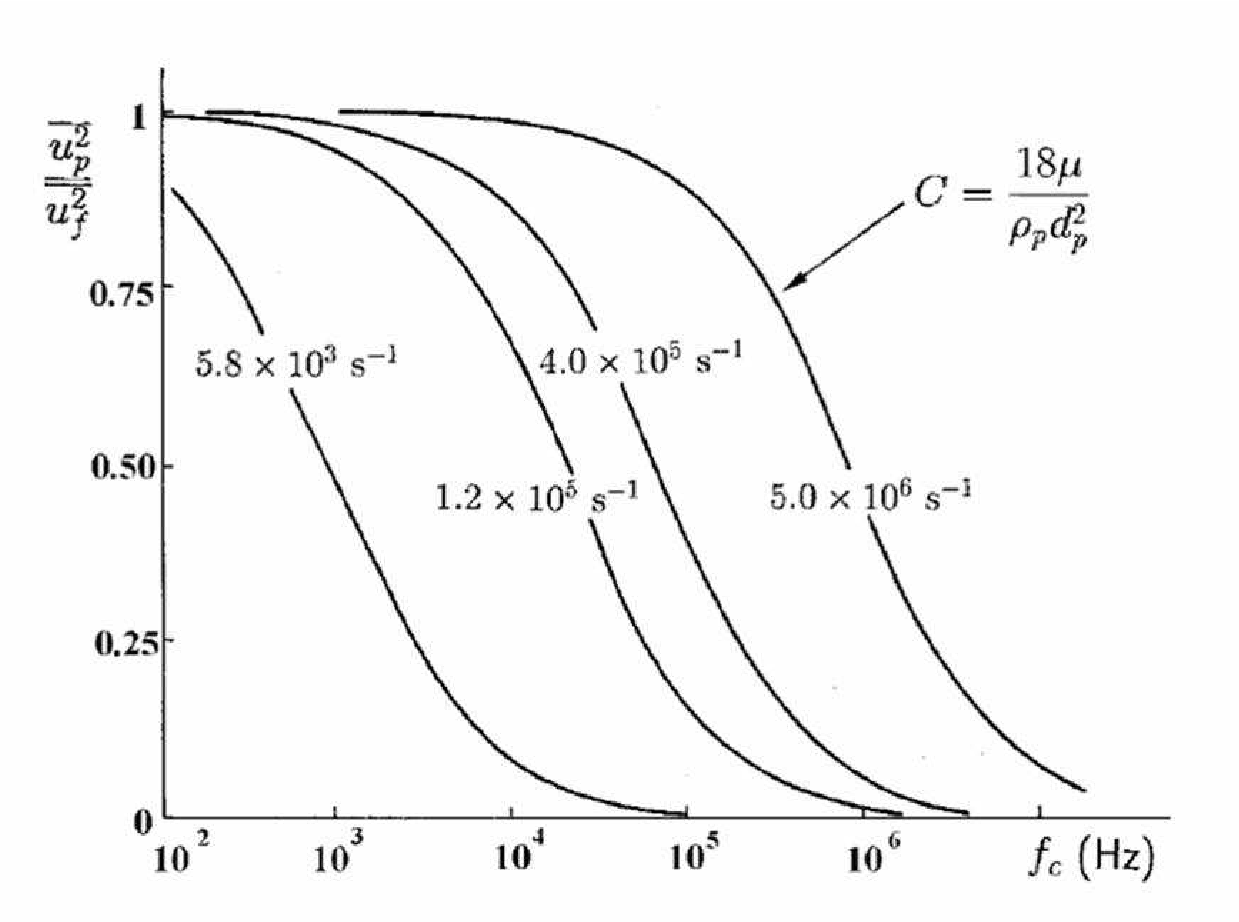

Figure 3.12: The response of particles in turbulent flow [35]

It was shown in section 3.3.1.1 that the density of the particles should be very close to the density of the fluid to avoid a sinking or floating effect. Having high density particles will affect the dynamics of the flow and so generate what is called a tracking error. This was represented by the complex calculation done by Basset [35]. If the volume fraction of the seeded particles to the actual fluid is less than 10^{-6}, the effect of the tracking could be neglected as per Elgosboshi [40].A primary source of error is the influence of gravitational forces if the densities of the fluid particles, ρ, and the tracer particles, ρ_p, do not match.

This effect was also studied by Agui and Jimenez [41].

Huang et al. [42] found a relation between the number of particles in the interrogation area and the error encountered in processing the PIV images called the particle number density error. As shown in Figure 3.13, more than 10 particles in the interrogation area would result in a relatively low level of errors.

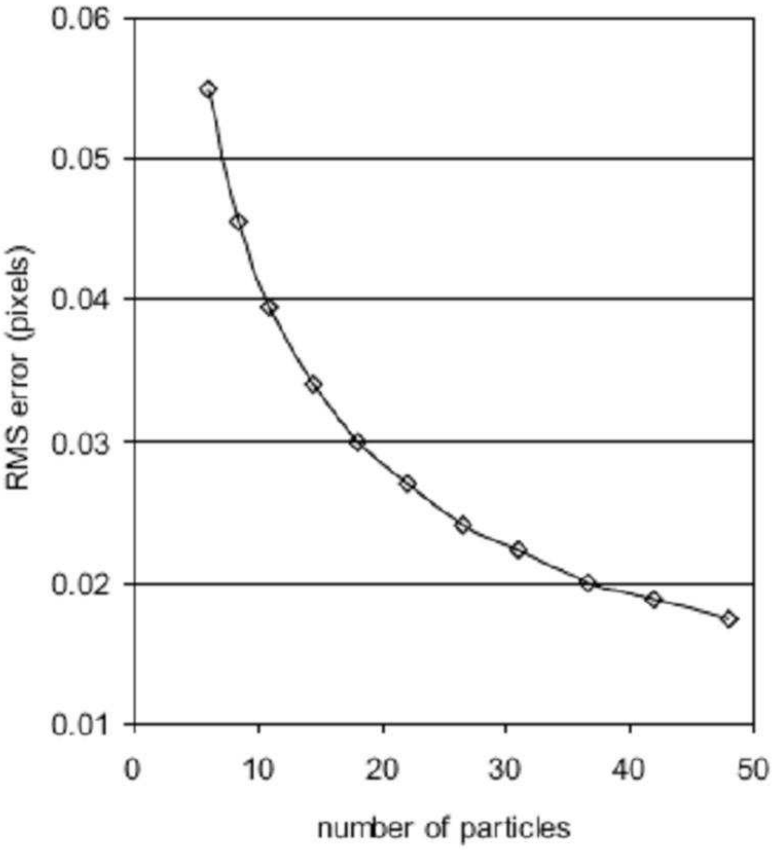

Figure 3.13: Error in determined displacement (in pixel) as a function of the particle number [42]

In the Dantec user manual [36], it was recommended to have on average of 10 particles per interrogation area in the case of auto correlation and 5 particles per interrogation area in the case of cross correlation based on Monte Carlo simulations. Dong et al. [24] concluded that if the particle density and magnification are chosen such that each window (interrogation area) contains at least 8 pairs of particles in both frames, the uncertainty can be kept at about 1 %. In general, it was concluded that as the number of particles in the interrogation area increases, the accuracy in determining the exact value of the velocity in that interrogation area increases.In this research an average of 7 to 8 particles were present in each interrogation area.

Guezennec and Kiritsis [43] studied the effect of both the particle size and the number of particles in the interrogation area on the error defined as the difference between the measured and the actual location of the particle. With an assumption that larger particles will increase the probability of overlapping and so counting overlapped particles as only one particle, they presented Figure 3.14 which shows that as the average particle size increases the average error increases.

In two dimensional PIV the velocity of the seeded particles is represented in one plane while the actual movement of the particles is in a 3-D volume. If the laser sheet where images of the particles are captured is thick, the successive frames might capture the movement in the third dimension which is then included in the planar velocity components causing parallax error. To avoid this error, the laser sheet must be maintained to its smallest possible thickness at the plane of interest. As explained before, a metal piece was manufactured to fit in the impeller channel with a 1 millimeter thickness line where the laser sheet was focused.

The ratio of the brightness of the particles to the brightness of the background must be

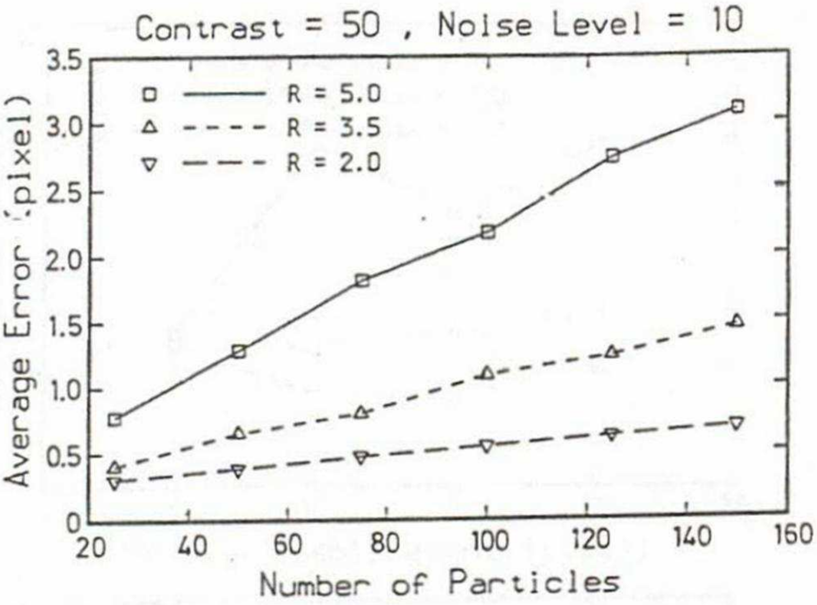

Figure 3.14: Relation of average error (in pixel) to particle size and number [43]

high. This ratio is called the signal to noise ratio (SNR). More noise in the background of the image means a brighter background and so lower SNR which makes it harder to distinguish between the particles themselves and the background causing a serious error in measuring the particles displacement called image contrast error. If the SNR is more than 100 counts in contrast, which refers to the difference between the particle intensity and the background intensity, the effect of the background noise might be neglected [43].

In 1991, Adrian [34] suggested that random error increases proportionally to particle size due to irregular particles and the imperfection of the film or CCD camera. In general, random errors are caused if the measurements fall above and below the true value of the parameter with equal probability and could be reduced by averaging large number of sample measurements. This type of error includes errors caused by the researchers such as disturbance to the equipment (such as focus of the camera or laser intensity) or fluctuating experimental conditions.

The inaccuracy of the peak-finding schemes, when trying to determine the sub-pixel accuracy of the particle displacement on the correlation plane, results in the bias error. As the resolution of the peak decreases, the accuracy of finding schemes deteriorates. The resolution is the worst when the particle size is smaller than one pixel [44].

The velocity calculated in the field of flow is represented by a map of vectors. Each vector represents an entire interrogation area which might hold different velocity gradients inside it other than that vector which causes the velocity gradient errors. Reducing the size of the interrogation area, especially when a high velocity gradient is expected, will help in minimizing the effect of this error [42].

The calculation of the velocity components in the PIV technique is based on the distance covered by the particle in a certain time. It is assumed that the particle maintains a constant velocity and not accelerating simply because we can not take an intermediate measurement. The absence of this acceleration in calculating the velocity gradient causes what is called by Boillet and Prasad [39] an acceleration error.

Some particles might move out of the laser plane and some might be introduced to it in the second frame which might cause a three dimensional error that could be avoided as per Adrian [34] if a particle displacement of less than a quarter of the interrogation area is considered.

Overlapping the interrogation areas when cross correlation processes take place helps in reducing the error that is caused by particles coming to or going out of the interrogation area as shown in Figure 3.15.

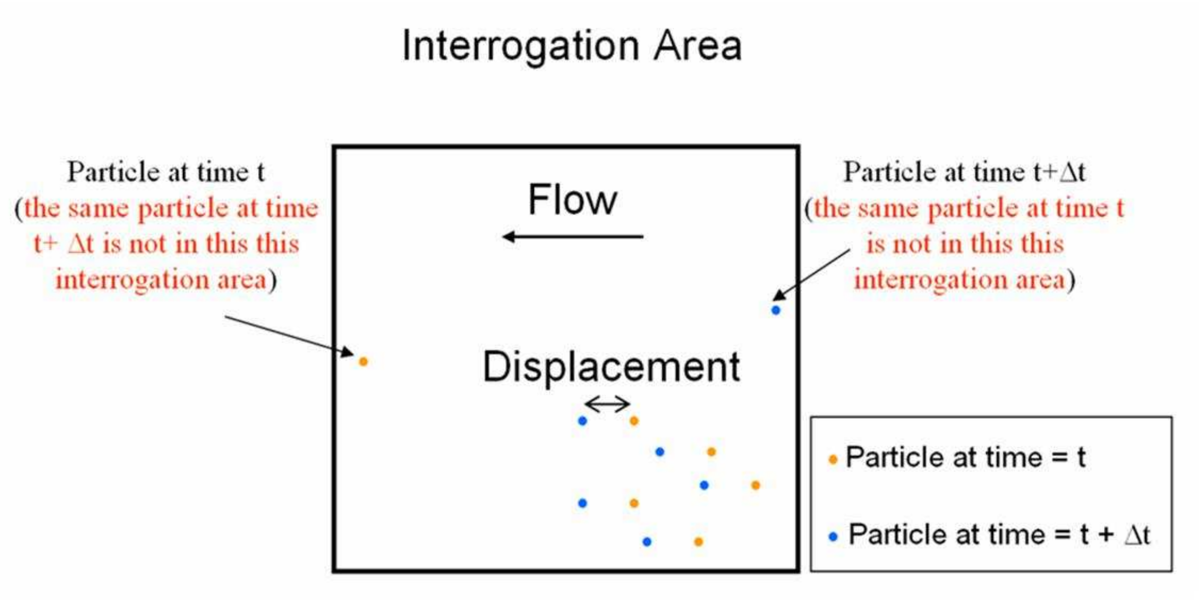

Figure 3.15: Particles moving in and out of the interrogation area

Chapter 4

Results and Discussion

4.1 Introduction

This chapter includes the results found in this research work. The performance measurement results of the impeller described in Chapter 2 will be presented including the pump performance curves. This will be followed by PIV results at the inlet and outlet of the impeller channel which support the flow behaviour phenomena at the design flow rate explained in Chapter 1. The development of flow separation and stall formation inside the impeller channels will be presented using consecutive PIV images including flow streamlines. This flow behaviour will be studied at the design flow rate, 75%, 50%, 40%, 30% and 25% of the design flow rate where the last is considered as an extreme off-design condition. The instantaneous behaviour of the flow at off-design conditions will be presented. Results of turbulence intensities calculation inside impeller passages at the flow rates mentioned above will be presented.

The change of the primary and secondary velocity profiles along the channel passage will be presented. A comparison between the results found in this research work and previous work in literature for similar impeller designs is provided.

4.2 Performance Results

To analyze the newly manufactured pump performance, dimensionless parameters such as pump efficiency, head coefficient, flow coefficient and pump specific speed were calculated. These dimensionless parameters were calculated using the results of measuring the flow rate passing through the impeller, the head across the impeller, the rotational speed and the torque and tare torque applied by the impeller. Also, information such as the fluid density, the impeller exit diameter, blade height at the exit, blade thickness, and number of blades (mentioned in Chapter 2) were used to determine the impeller overall performance.

Based on previous studies for a similar pump design [26, 27], the best performance for this impeller design was achieved at 150 revolutions per minute. At this speed, the flow rate was reduced gradually from 17.0 L/s to 3.0 L/s and pump efficiency and dimensionless parameters were calculated (Table 4.1). In Table 4.1, the highest pump efficiency occurs at 64.8 % when the flow rate is 13.4 L/s. The pump performance curves are illustrated in Figure 4.1. Figure 4.1 compares well to the typical centrifugal pump performance curve shown in Figure 1.5. As the pump approached the shut-off condition (zero flow rate), the efficiency approaches zero. Also, at higher flow rates, both the efficiency and the head reach zero values but this could not be performed due to the capacity limit of the inlet pipes. The peak value of the pump efficiency which is 64.8 % corresponds to a head of 0.76 m.

Flow rate (L/s) (Q)	Efficiency (%) (η)	Specific Speed (N_s)	Flow Coefficient (φ)	Head Coefficient (ψ)
17.0	60.7	0.54	0.15	0.39
15.4	64.1	0.47	0.14	0.44
13.4	64.8	0.40	0.12	0.49
11.8	62.0	0.37	0.11	0.51
10.9	61.9	0.34	0.10	0.53
8.5	54.5	0.31	0.08	0.53
5.6	44.3	0.25	0.05	0.53
4.1	36.3	0.21	0.04	0.53
3.0	31.4	0.18	0.03	0.53

Table 4.1: Pump performance parameters at 150 rpm

The curves of the impeller efficiency and head coefficient versus the flow coefficient are shown in Figure 4.2 and Figure 4.3. In Figure 4.2 and Figure 4.3, it is clear that as the flow coefficient increases, the efficiency increases and the head coefficient decreases. The impeller performance coefficients for the design flow rate are shown in Table 4.2. The uncertainty in the impeller efficiency measured is presented in Appendix A.

Figure 4.4 shows a comparison between the ideal Euler case, the ideal case with slip factor included and the actual experimental head and flow coefficient curves where the best efficiency of this impeller was measured at flow coefficient equal to 0.12. An obvious decline was noticed in the actual head and flow coefficient curve where the effect of actual velocity slip and frictional losses were included. This proved the existence of a significant angle deviation that will be demonstrated later in section 4.3.4.

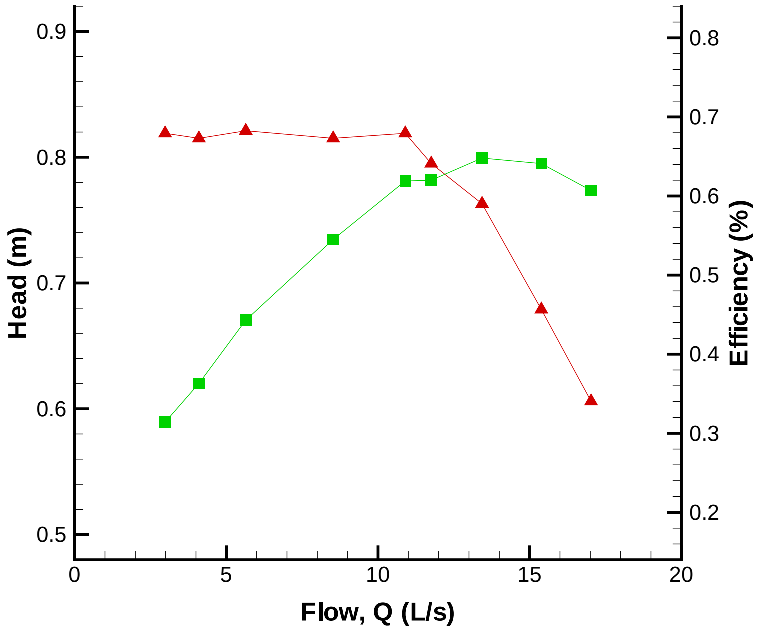

Figure 4.1: Pump performance curve

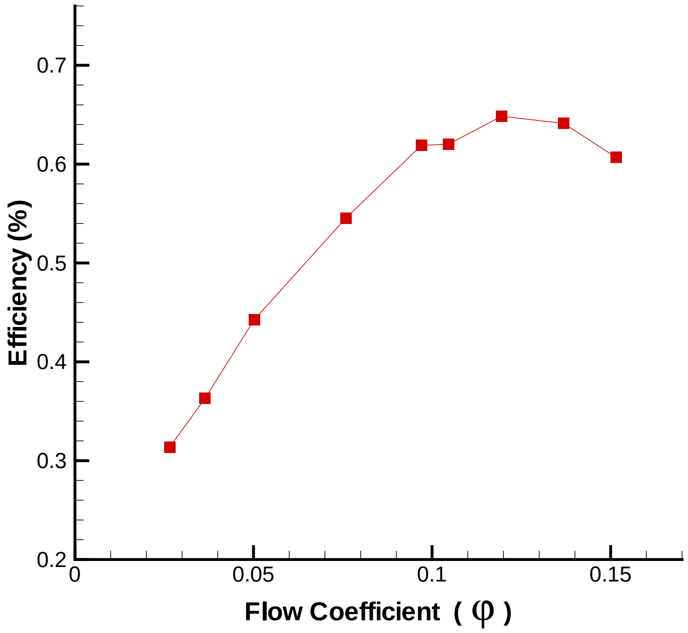

Figure 4.2: Pump efficiency versus flow coefficient at 150 rpm

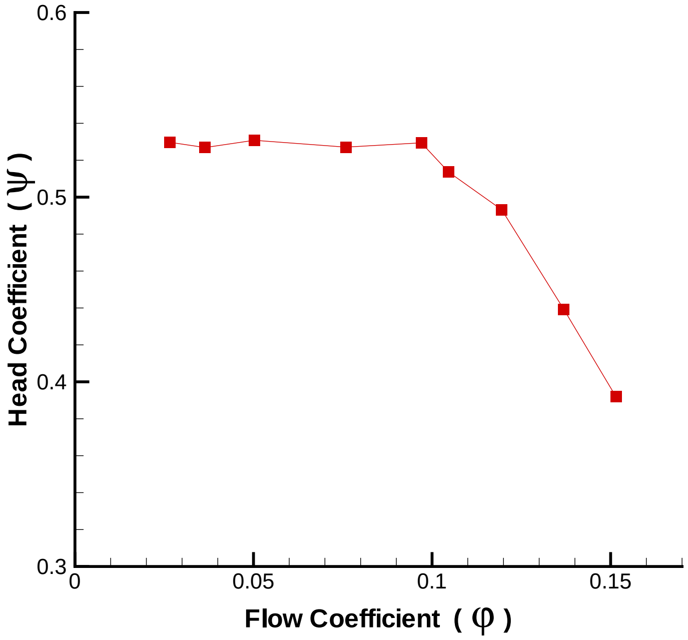

Figure 4.3: Pump head coefficient versus flow coefficient at 150 rpm

Angular Velocity (ω)	15.7 rad/s (150 rpm)
Design flow rate (Q)	13.43 L/s
Design Head rise (H)	0.76 m
Design Specific Speed (N_s)	0.4
Design Head Coefficient (ψ)	0.49
Design Flow Coefficient (φ)	0.12
Design Efficiency (η)	0.648

Table 4.2: Impeller performance parameters at the design flow rate

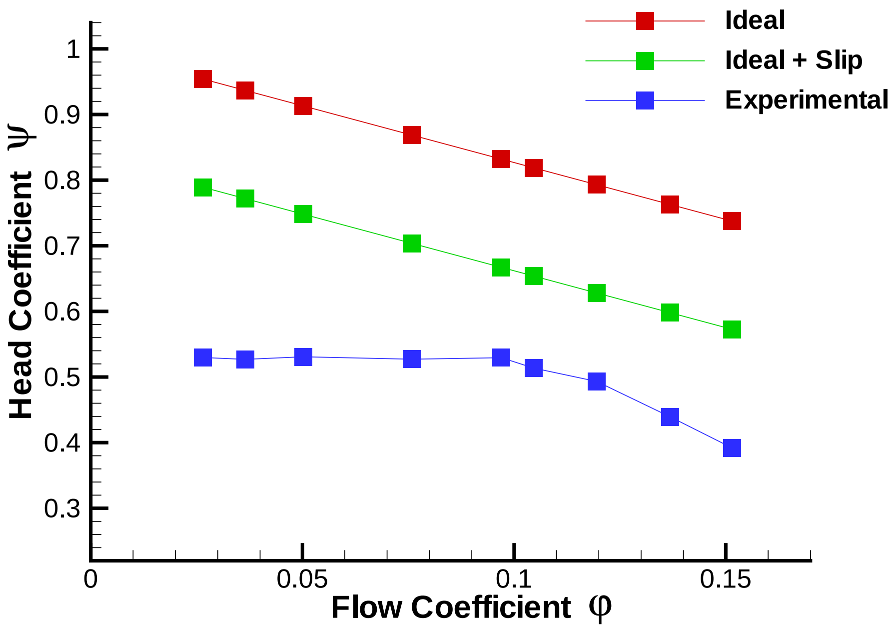

Figure 4.4: Comparison of actual, Euler (ideal) and ideal with slip head and flow coefficient curves

4.3 PIV Results

All PIV images were taken at the mid-height of the impeller channel (10.5 mm). This position was precisely determined by using a prefabricated metal cube that fits perfectly inside the channel with the laser sheets focused on a groove made on the mid-height of that cube. This was the case for all flow rates and throughout the whole channel passage.

4.3.1 Flow Behaviour at Design Flow Rate

4.3.1.1 Mean Relative Velocity and Streamline

Images were taken at two locations in the impeller passages. These locations are shown in Figure 4.5.

As described in Chapter 1, the flow behaviour at the design flow rate entered the channel from the impeller eye and moved towards the suction side of the blade when passing the mid channel and then moves back towards the pressure side when approaching the passage exit (Figure 1.10). A total of 1000 images were captured at each location (inlet and outlet). Samples of raw images at both inlet and outlet are shown in Figure 4.6. The size of each of these images frames is 81 mm by 82 mm (1008 x 1018 pixels)

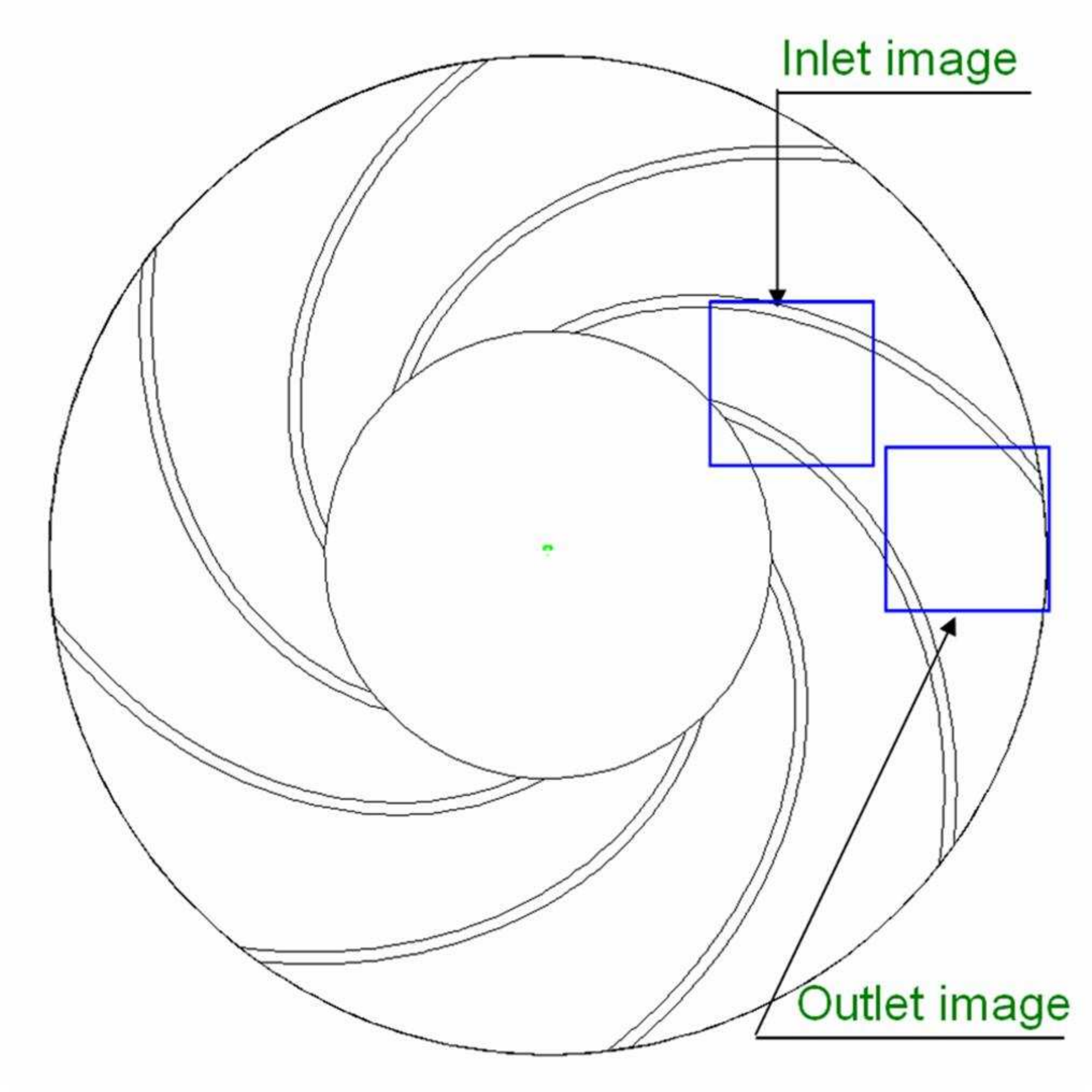

Figure 4.5: Locations of PIV images at the inlet and outlet of the impeller channel

a) Inlet

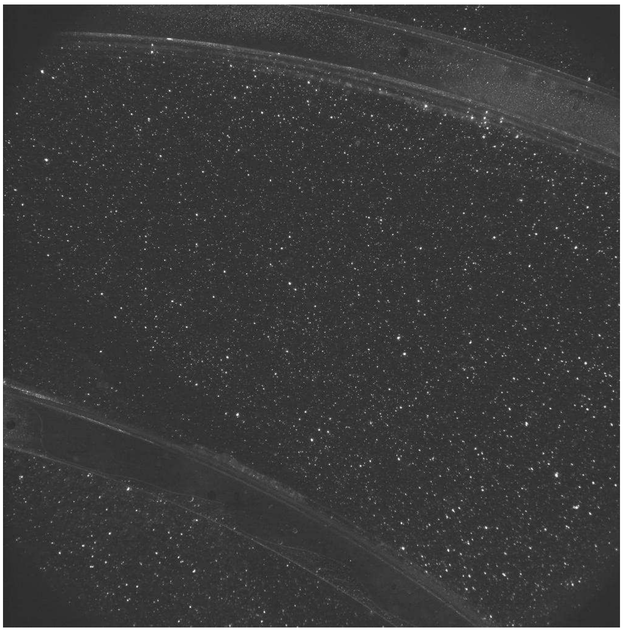

b) Outlet

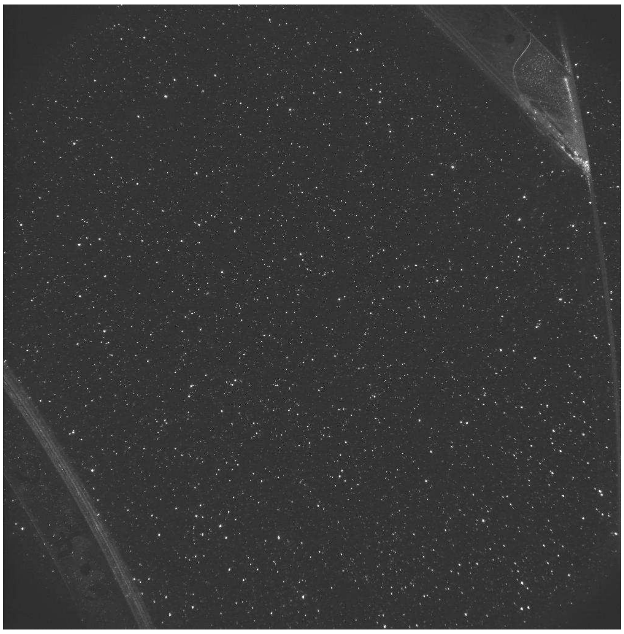

Figure 4.6: Raw image of flow seeded at a) the inlet and b) the outlet of the impeller channel

The result of performing cross-correlation (vector map) on instantaneous image pairs captured using the PIV technique shows flow velocities ($\overline{V}$) in the direction of the rotation of the impeller since the rotational velocity ($\overline{U}$) was dominant over the relative velocity ($\overline{W}$) inside the channel (Figure 4.7).

$$\overline{V} = \overline{U} + \overline{W} \tag{4.1}$$

The local rotational velocity is subtracted from all the vectors (3844 vectors) that compose the PIV vector map. The mean relative velocity vectors obtained by averaging each set of 1000 images at design flow rate are shown in Figure 4.8 for a) the inlet and b) the outlet.

Streamlines inside the impeller channel at both the inlet and outlet are drawn and presented in Figure 4.9.

It is obvious from Figure 4.8 and Figure 4.9 that the water flowing inside the impeller channel moved towards the suction side at the mid passage of the channel and moved back again towards the pressure side the exit of the channel which agrees with the flow behaviour phenomena at the design flow rate explained in Chapter 1. The streamlines show no separation throughout the whole channel.

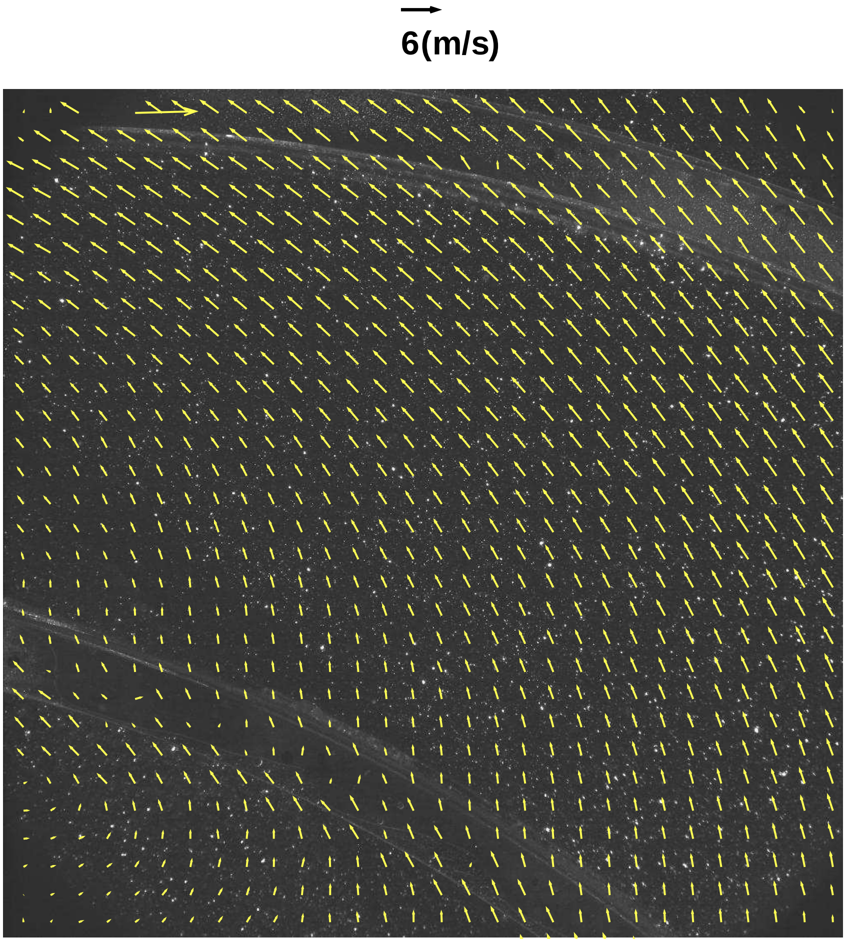

Figure 4.7: Vector map of instantaneous image at the inlet with rotational velocity

a) Inlet

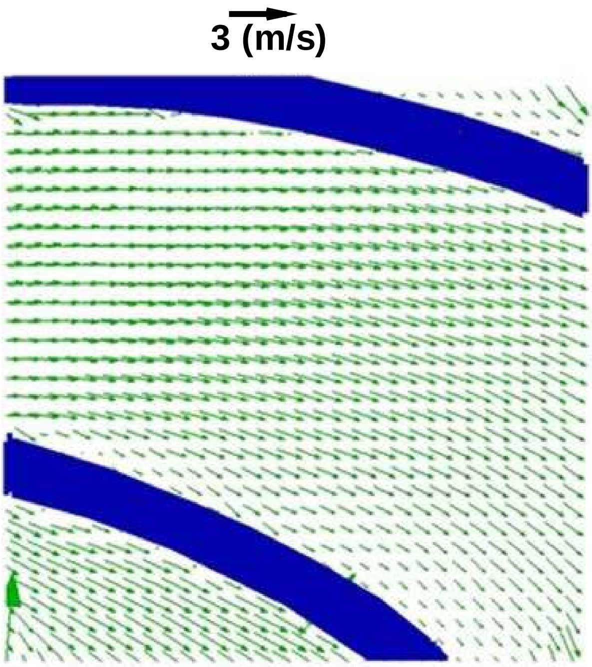

b) Outlet

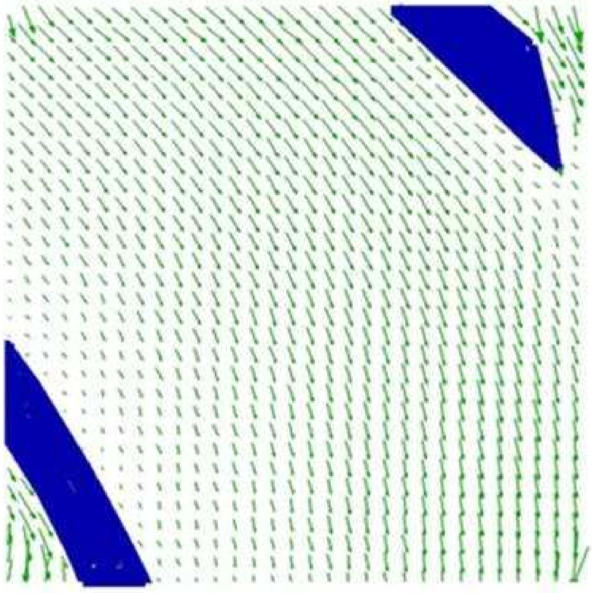

Figure 4.8: Mean relative velocity vectors obtained by averaging 1000 instantaneous images at design flow rate at a) the inlet and b) the outlet of the impeller channel

a) Inlet

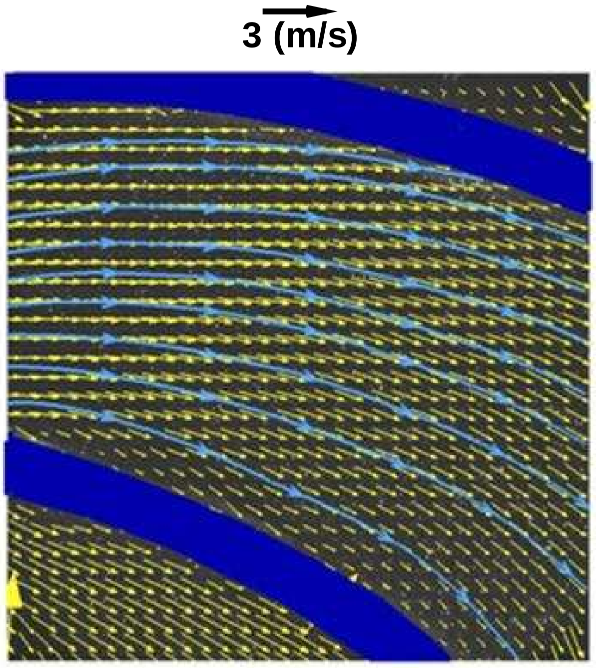

b) Outlet

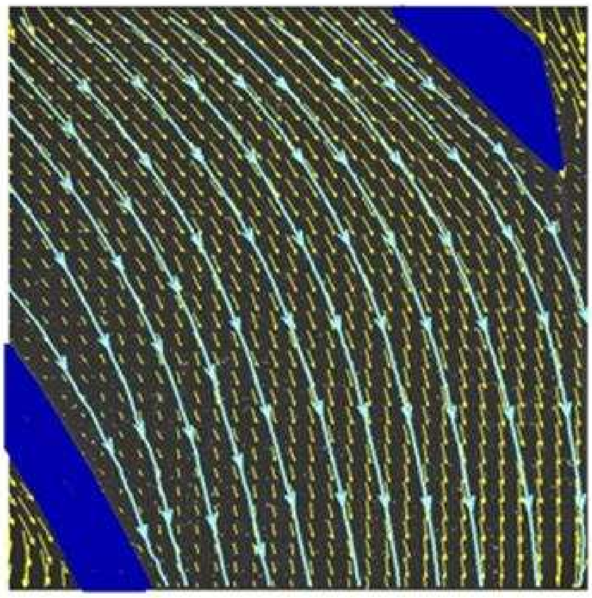

Figure 4.9: Streamlines inside impeller a) inlet and b) outlet at design flow rate using the averaged 1000 instantaneous images

4.3.1.2 Mean Normalized Primary and Secondary Velocity at Design Flow Rate

Primary Velocity

As mentioned in Chapter 1, the primary velocity (W_p) is the velocity that follows the direction of the blade curvature towards the outlet of the channel while the secondary velocity (W_s) is the component perpendicular to the primary velocity with the positive direction pointing towards the suction side. Due to the locations of the inlet and outlet frames relative to the impeller centre, the primary and secondary velocity components direction changes as the flow proceeds through the channel. The directions of the primary and secondary velocity are shown in Figure 4.10 for the inlet and outlet of the channel.

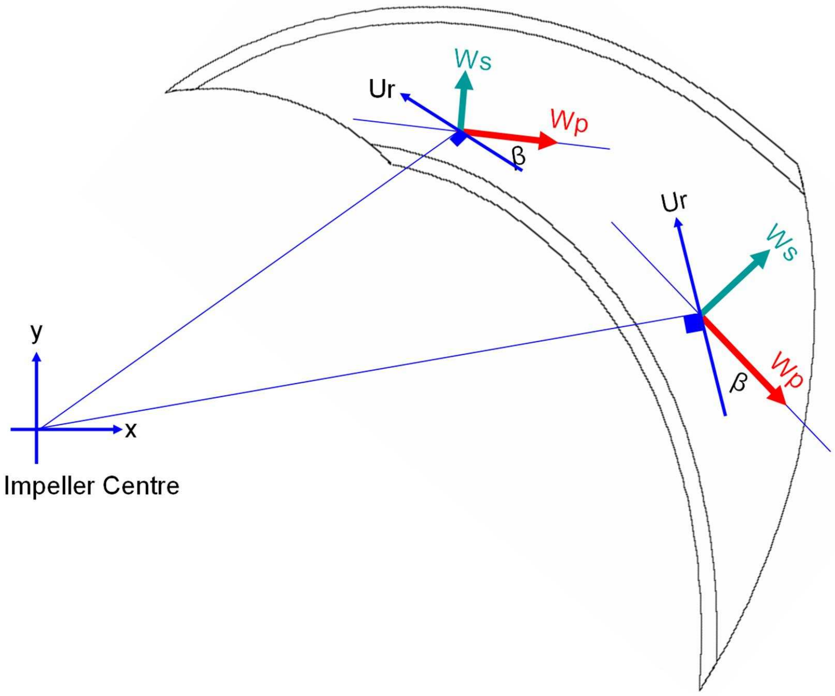

Figure 4.10: Primary and secondary velocity component inside the channel passage

A positive value for the primary velocity component means that the flow is moving towards the outlet of the channel while a negative value mean the fluid is moving towards the channel inlet. Values close to zero for the primary velocity component means the fluid is either stationary or moving from one side to the other inside the channel passage which is the case when we look at the secondary velocity component. Positive secondary velocity values mean that the fluid is moving towards the suction side of the channel. This is usually the case at the inlet to the mid channel passage at design flow. Negative secondary velocity values mean that the fluid is moving towards the pressure side of the channel. This usually takes place close to the exit of the channel at the design flow condition. Primary and secondary velocities are measured at six different locations inside the impeller passage (Figure 4.11). These locations occurs at arcs of distances 140 mm (close to inlet), 152 mm, 165 mm, 191 mm, 216 mm and 229 mm (close to exit) from the centre of the impeller.

It is important to mention that the primary velocity is dominant over the secondary component at design condition. This is due to the general flow direction which the primary component follows. Due to the small magnitude of the secondary velocity component, a small change in the flow direction is significant. Figure 4.12 shows the mean normalized primary velocity components at six different locations inside the impeller passage at the design flow rate.

In Figure 4.12 a) to f), it is clear throughout the channel (all six locations) that the magnitude of the primary velocity increases as it moves from the pressure side to the suction side of the channel. At locations very close to the blade wall at the suction side, the primary

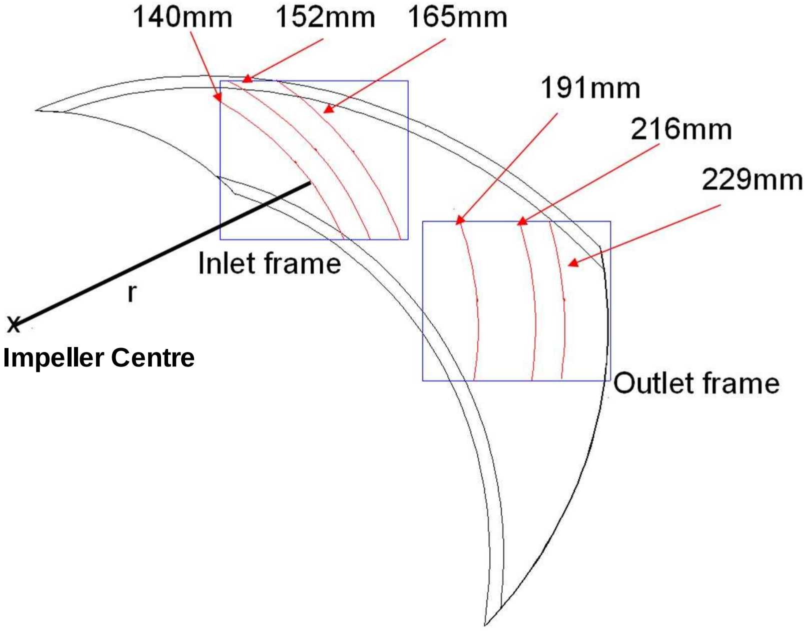

Figure 4.11: Locations of the primary and secondary velocity measurement inside the channel

velocity values start decreasing again and this due to the flow being affected by the boundary layer. Comparing Figure 4.12 b), c) and f), which include values touching the blade at the suction side, it is noticeable that the decrease in primary velocity values due to the boundary layer effect is growing more towards the mid passage. This means that the boundary layer at the suction side is thickening as the fluid moves toward the channel exit. Also, comparing the whole profile of the primary velocity throughout the channel passage, it is noticed that a general decrease in the magnitude when approaching the exit. The reason for the reduction in primary velocity profile is the expansion of the area from the inlet to the outlet where the same amount of fluid is passing through (Figure 4.13). The uncertainty in the mean normalized primary velocity measured is presented in Appendix A.

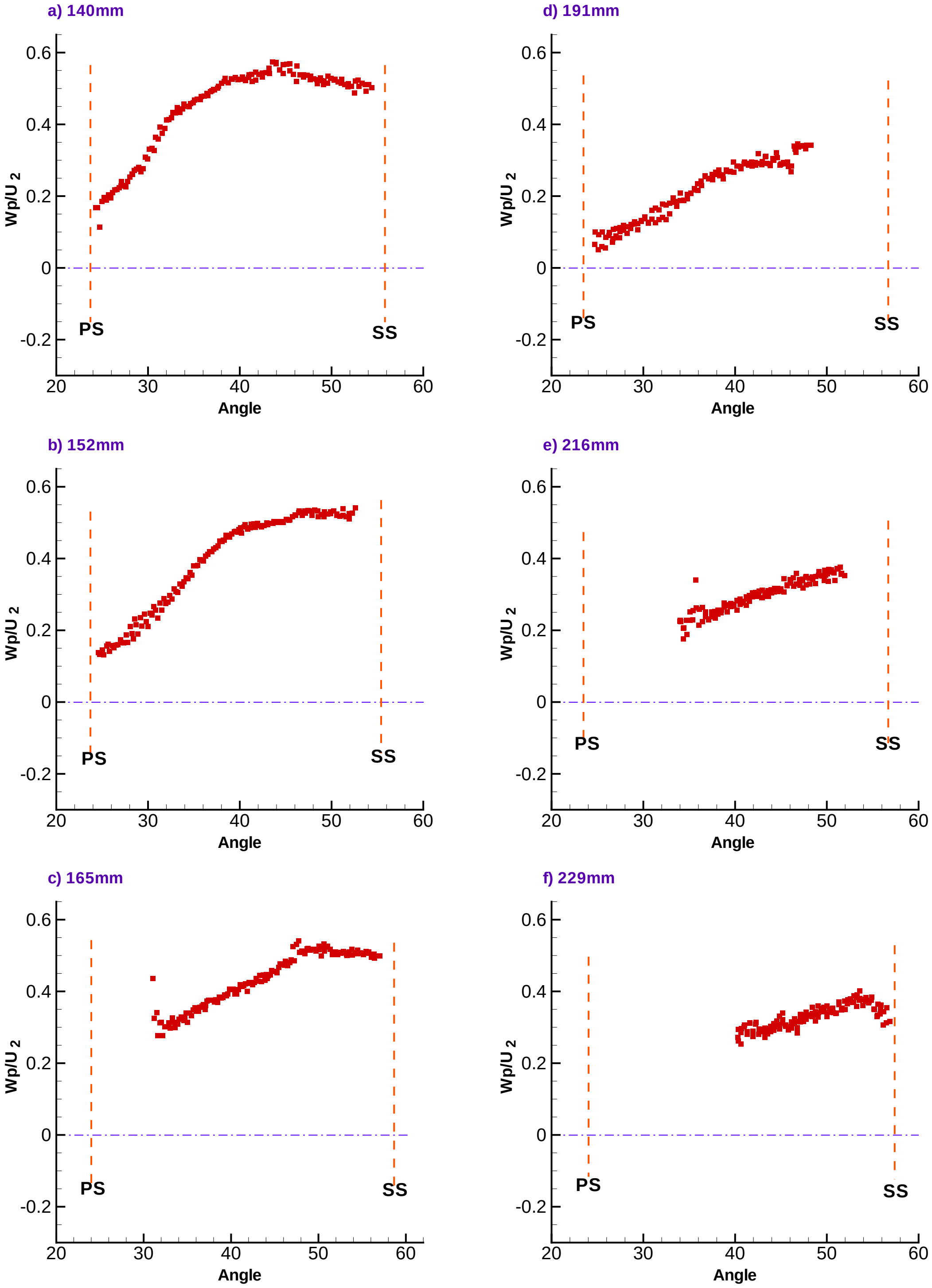

a) 140mm

b) 152mm

c) 165mm

d) 191mm

e) 216mm

f) 229mm

Figure 4.12: Mean normalized primary velocity for design condition at a) 140 mm b) 152 mm c) 165 mm d) 191 mm e) 219 mm and f) 229 mm

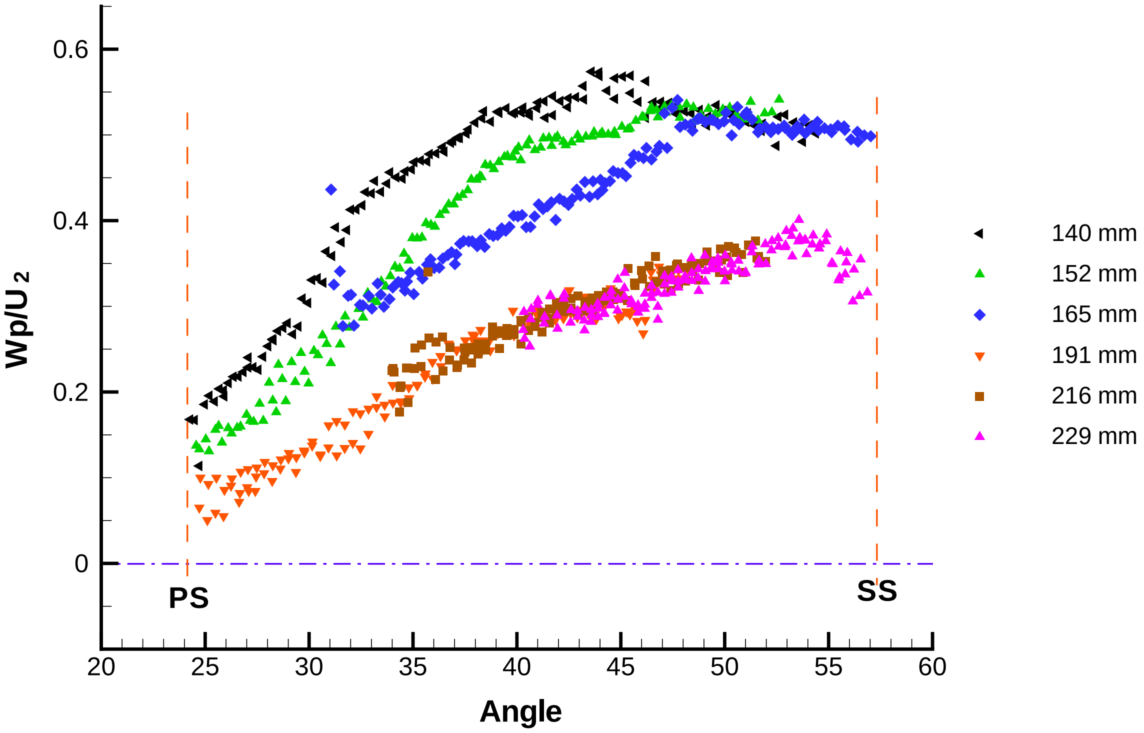

Figure 4.13: Effect of area increase on the mean normalized primary velocity profile throughout the channel at design condition

Secondary Velocity

Figure 4.14 shows the mean normalized secondary velocity components at six different locations inside the impeller passage at the design flow rate.

At the inlet of the blade channel(Figure 4.14 a), b) and c)), the secondary velocity is mainly positive and increasing in magnitude as it approaches the suction side of the blade. This agrees with the flow theory at the design flow rate explained in Chapter 1. Looking at Figure 4.14 d), e) and f), the secondary velocity profile starts with negative values in the area close to the pressure side and it increases as it proceeds towards the channel exit. This also agrees with the flow theory explained in Chapter 1. The change in the secondary velocity sign from negative to positive at mid channel is due to the design of the blade curvature at the exit of the channel shown in Figure 4.10. The small values of the secondary velocity do not imply a large change in the flow direction when the sign changes. As seen in the primary velocity, the whole profile of the secondary velocity shifts to a lower magnitude as it moves towards the channel exit. The reason for the reduction is the expansion of the area from the inlet to the outlet where the same amount of fluid is passing through (Figure 4.15).

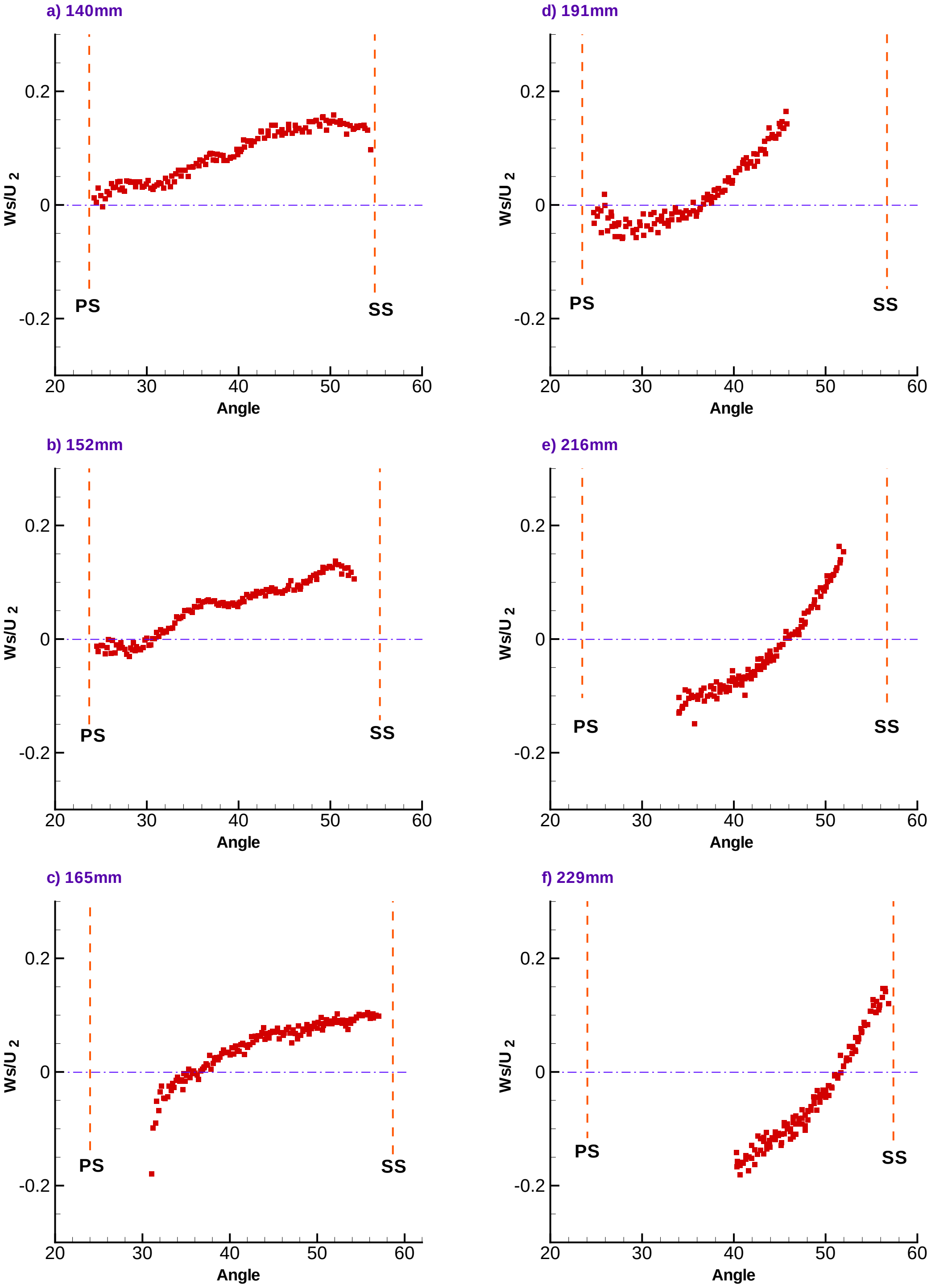

Figure 4.14: Mean normalized secondary velocity for design condition at a) 140 mm b) 152 mm c) 165 mm d) 191 mm e) 219 mm and f) 229 mm

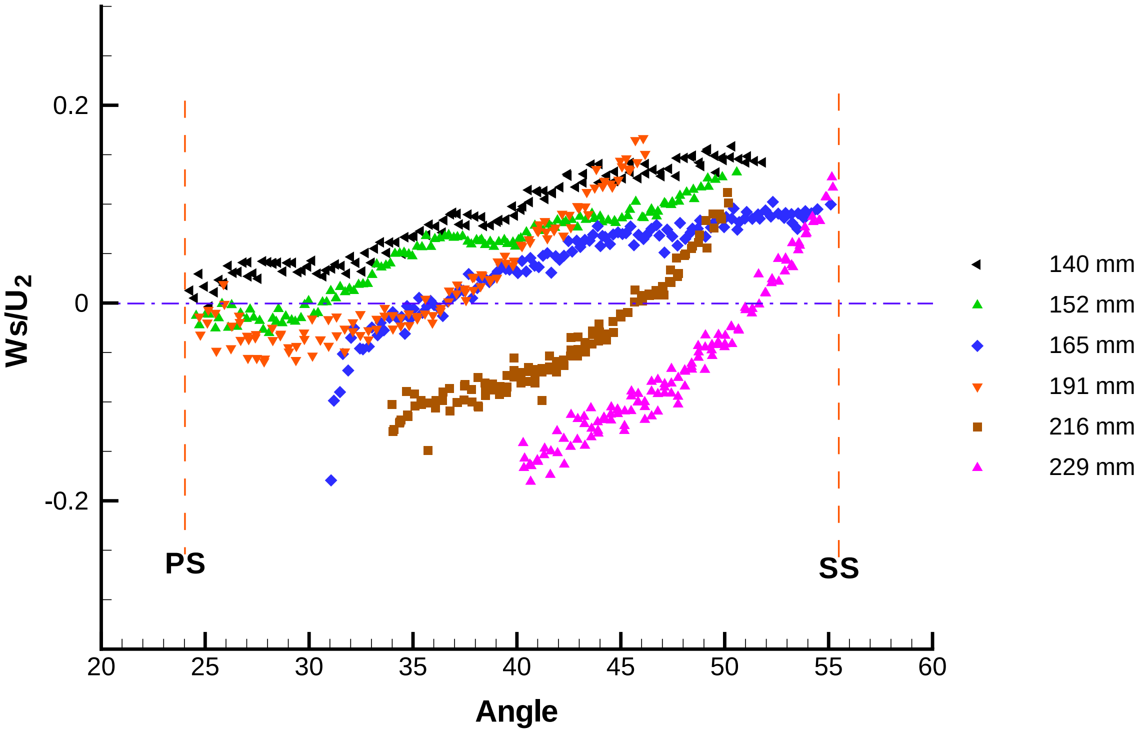

Figure 4.15: Effect of area increase on the mean normalized secondary velocity profile throughout the channel at design condition

4.3.1.3 Mass Balance Calculation

A mass balance calculation was performed to compare the flow rate measured using the PIV technique with the design flow rate measured using the ultrasonic flowmeters. At the design flow rate, the primary velocity components on the 152 mm arc across the channel were used. The flow rate was calculated using the following formula:

$$Q = (W_p \times A) \times 8 \text{ Channels} \tag{4.2}$$

where A is the total area inside the channel at 152 mm. The total mass flow calculated was 15.6 L/s which is higher than the measured flow rate at design condition (13.4 L/s). Assuming the turbulent fluid flow inside the impeller channel to be similar to that inside pipes and ducts (Figure 4.16), the maximum velocity should occur at the mid height of the channel where it was actually measured. The calculated ratio of the average velocity to the maximum in this case was 0.86. With Reynolds numbers ranging between 10^4 to 10^5 (average primary velocity of 2 m/s inside the channel), the ratio of the average velocity to the maximum velocity ranges from 0.814 to 0.852. The calculated ratio in this case is reasonably comparable to the range stated above by White [1].

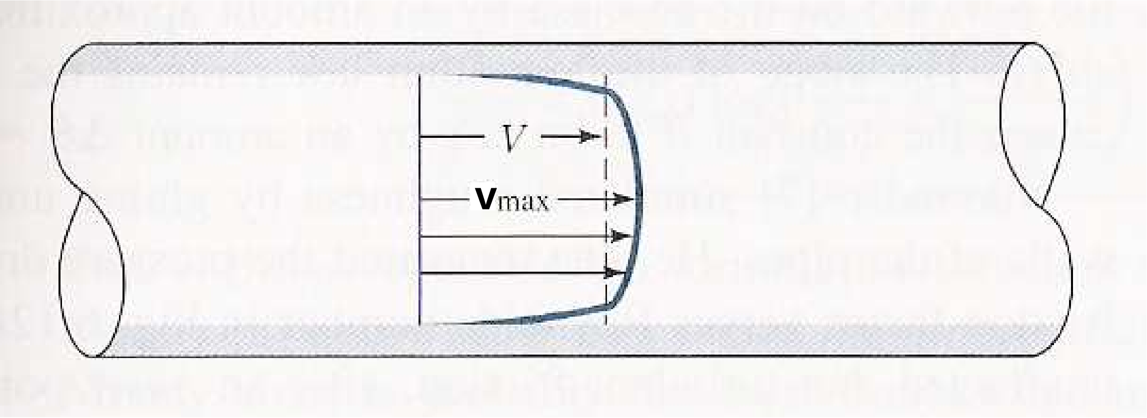

Figure 4.16: Turbulent pipe flow velocity profile [1]

4.3.2 Flow Behaviour at Off-Design Conditions

4.3.2.1 Mean Relative Velocity and Streamline

The off-design conditions in this study are 75%, 50%, 40%, 30% and 25% of the design flow rate (13.43 L/s). The reason for studying these flow rates is to observe the fluid behaviour as the flow rate decreases gradually. This should show the range of flow rates such an impeller could acceptably perform if the flow has to be reduced. Furthermore, this should demonstrate the evolution of stalled channels and approximately detect the flow rate where it occurrs.

Figures 4.17 to Figure 4.26 show the mean relative velocity vectors and the streamlines for all off-design flow rates at both the inlet and the outlet. These figures are presented as an average of 1000 images taken at the same location with the same flow rate.

At 75% of the design flow rate, there is no significant change in the flow behaviour at the inlet of the channel (Figure 4.17). However, at the outlet, the growth of the boundary layer on the suction side is evident and results in a very minor separation at the exit of the suction side of the channel (Figure 4.18). There is no circulation or inward flow at 75% design flow rate.

At 50% of the design flow rate, the change in the relative velocity angle of attack at the tip of the blade resulted in a separation in the wake of the blade (suction side) which evolved to a recirculation zone (Figure 4.19). This area of recirculation occupies around one quarter of the width of the inlet. The remainder ofthe inlet shows a flow towardsthe exit of the channel and following the pressure side curvature (Figure 4.19 b). As expected, the separation that started at the wake of the blade at the inlet propagated to the exit of the channel and produced a recirculation zone that covers almost a third of the channel exit (Figure 4.20). With almost two thirds of the channel passage containing fluid passing through the channel the impeller efficiency at this flow rate is 48% which means a loss of almost 25% of the peak efficiency (64.8%).

At 40% of the design flow rate, the centre of the recirculation zone started moving from the suction side towards the mid channel covering almost half of the channel inlet (Figure 4.21). At the outlet, close to a third of the channel exit area contains water passing through while the other two thirds experiences a large recirculation (Figure 4.22). This means that a complete stall eddy is not yet formed at this flow rate and the channel is not considered stalled despite of the large recirculation zone. It is important to note that the recirculation region does not represent one huge vortex but a combination of many small ones with their centres falling almost at the same path and forming the centre of the large one when they are averaged. Instantaneous relative velocity vector maps will be demonstrated later in this chapter as averages of 1000 images do not adequately represent the flow field.

At 30% of the design flow rate, the recirculation region becomes bigger and stronger and located at the mid channel inlet with water flowing towards the channel inlet on the suction side and towards the outlet at the pressure side (Figure 4.23). This strong distortion of the flow behaviour continues throughout the channel and almost forms a full blockage at the exit of the channel (Figure 4.24 a). The streamlines show that the fluid is crossing the channel exit radially from the pressure side to the suction side instead of exiting the channel passage (Figure 4.24 b). The same behaviour is observed at 25% of the design flow rate inside both the inlet and the outlet (Figure 4.25 and Figure 4.26).

As explained before, averaging 1000 images at flow rates lower than the design condition is not very informative where details of the flow separation and existence of eddies and vortices can not be assessedated. However, the general flow pattern was still evident in locations where there were no frequent changes such as the flow near the suction and pressure sides. The path where vortices existed was also observed where the velocity vectors are averaged to zero (Figure 4.23). Examples of the instantaneous images of the flow behaviour at off-design conditions are presented in the next section.

In summary, the results indicated that there was no significant change in the general flow behaviour between the design condition and the 75% flow rate case. Major changes in the flow behaviour, when compared with the design condition, started to appear at 50% of the design flow rate and lower. This included the development of the separation area at

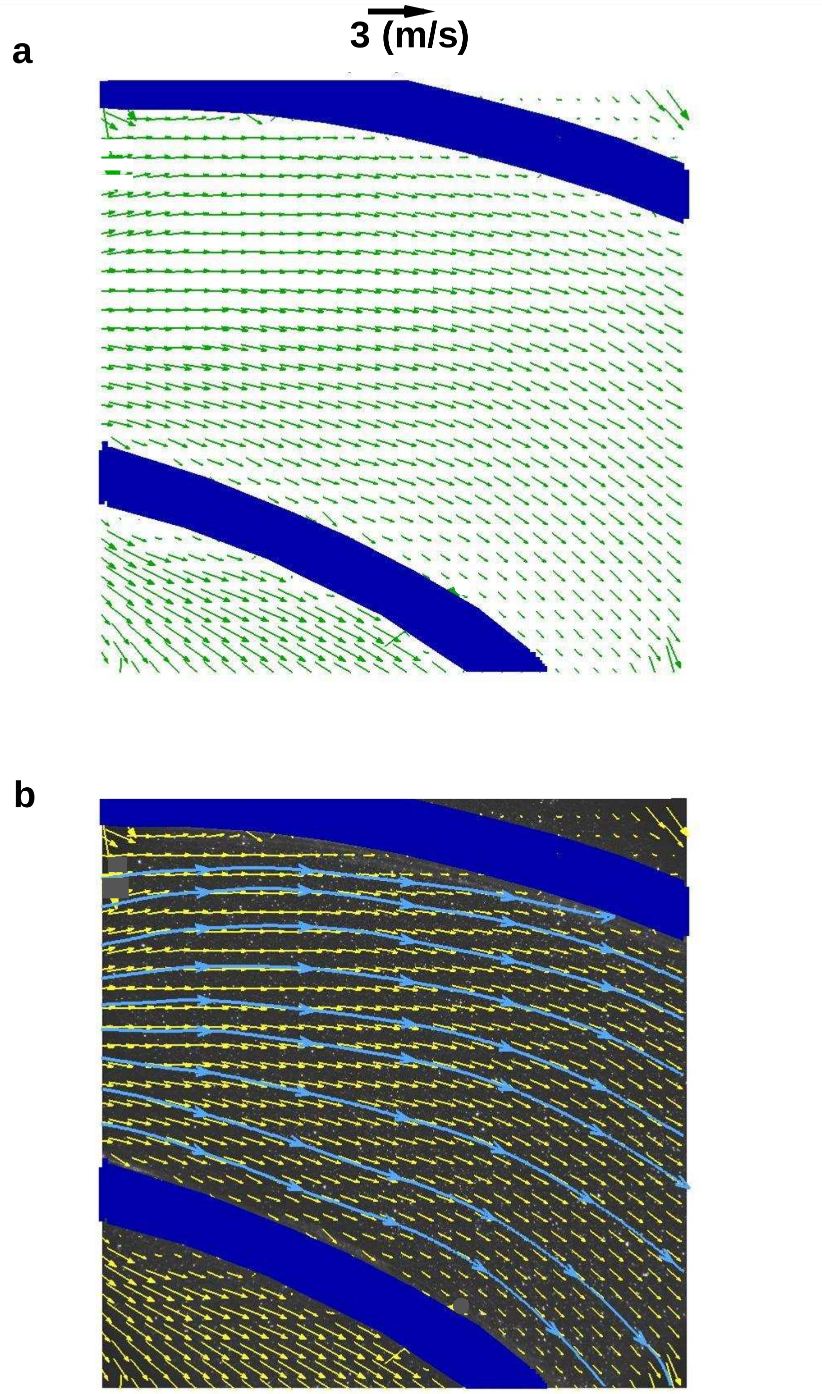

Figure 4.17: Mean relative velocity a) vector map and b) streamlines at the inlet at 75 % of design flow rate

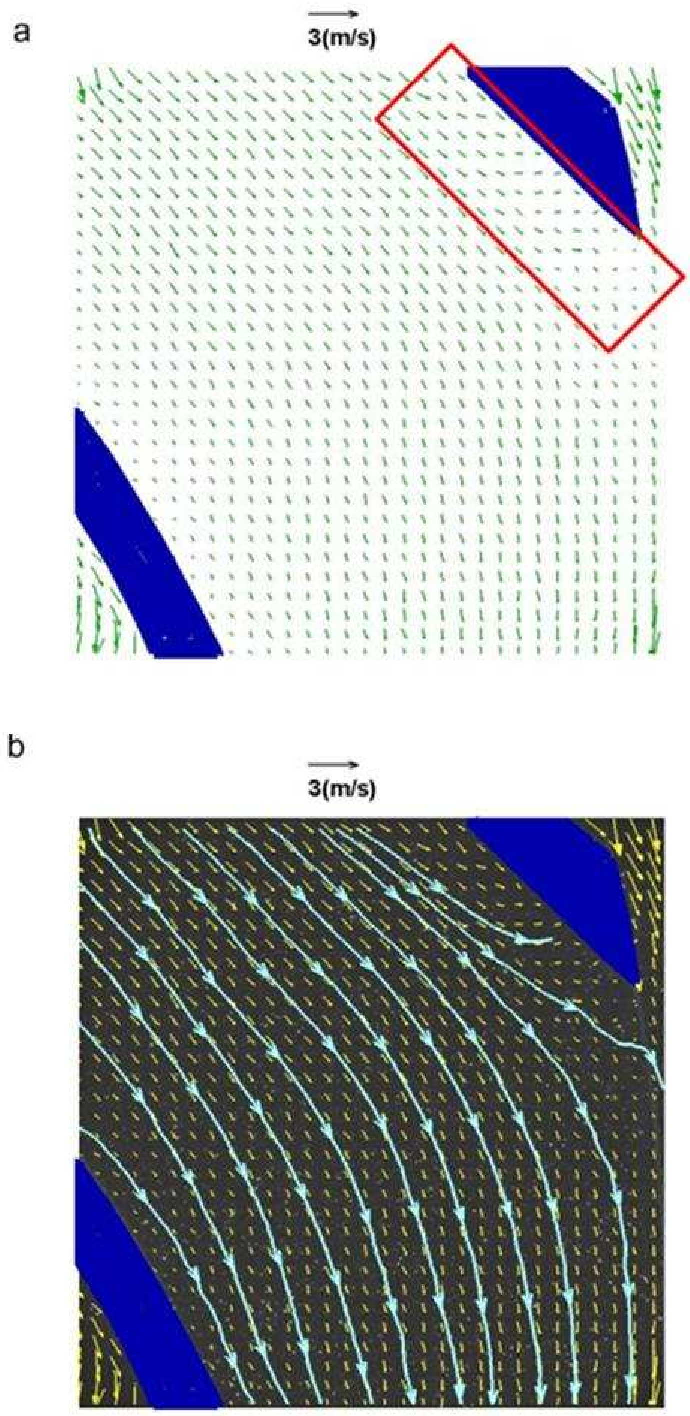

Figure 4.18: Mean relative velocity a) vector map and b) streamlines at the outlet at 75 % of design flow rate

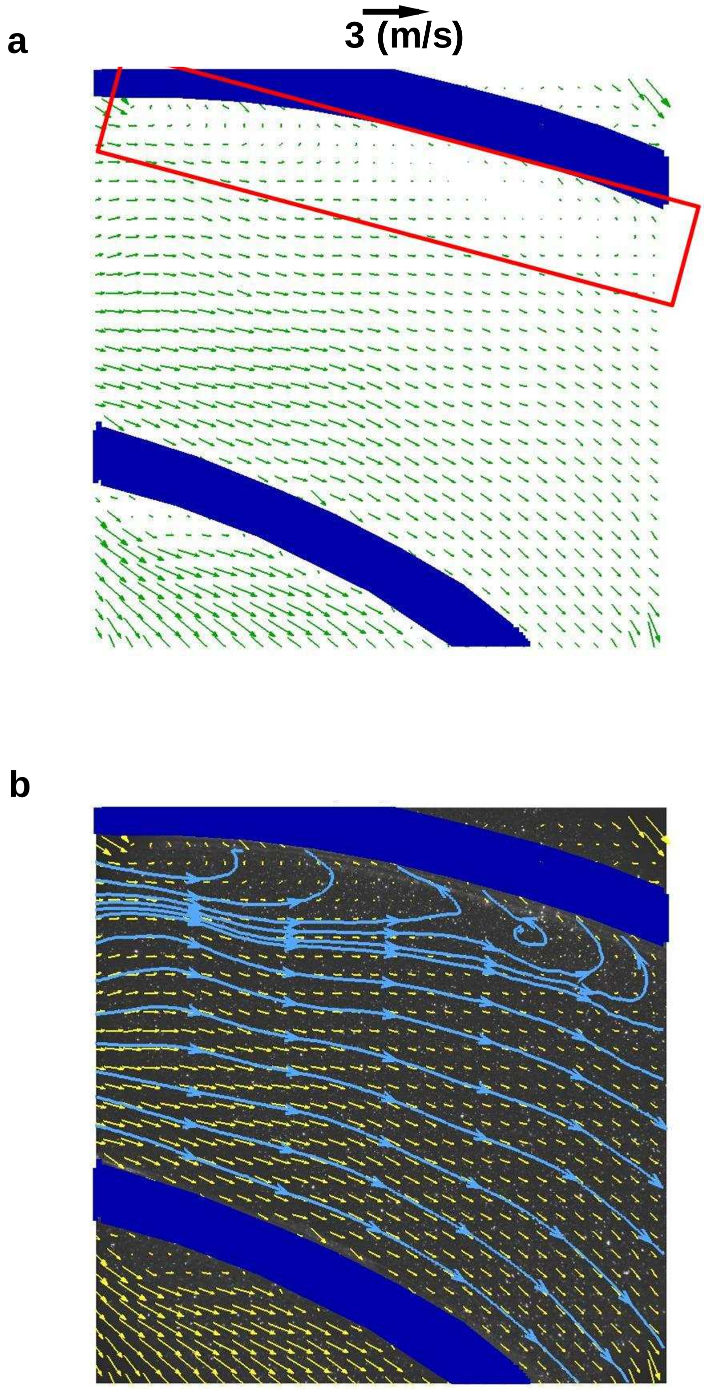

Figure 4.19: Mean relative velocity a) vector map and b) streamlines at the inlet at 50 % of design flow rate

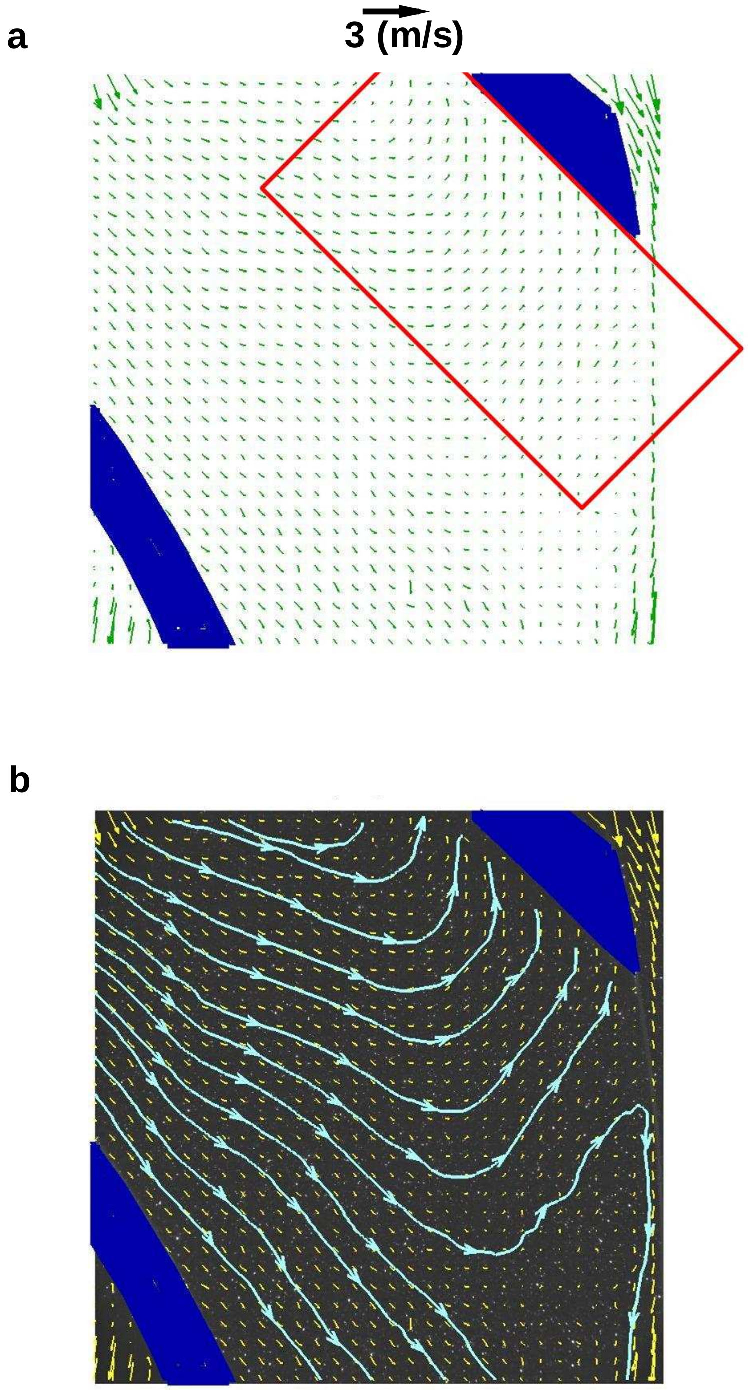

Figure 4.20: Mean relative velocity a) vector map and b) streamlines at the outlet at 50 % of design flow rate

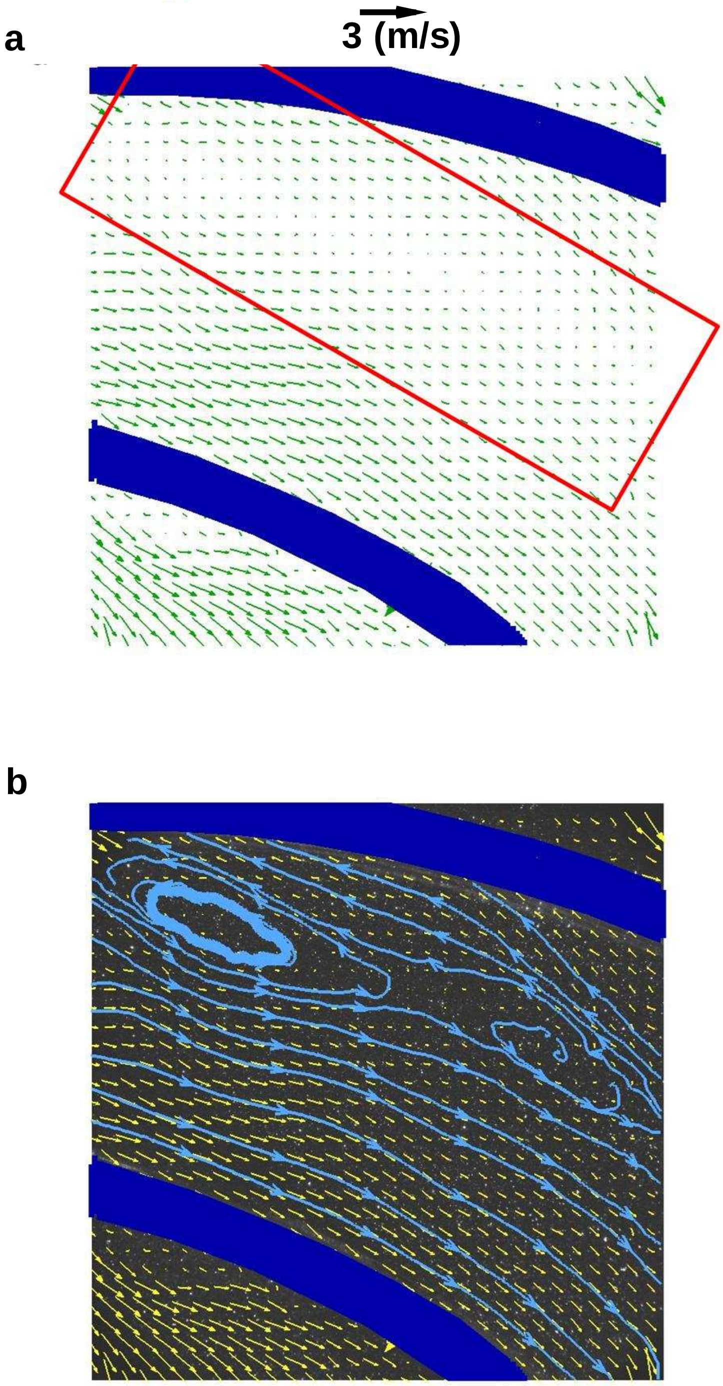

Figure 4.21: Mean relative velocity a) vector map and b) streamlines at the inlet at 40 % of design flow rate

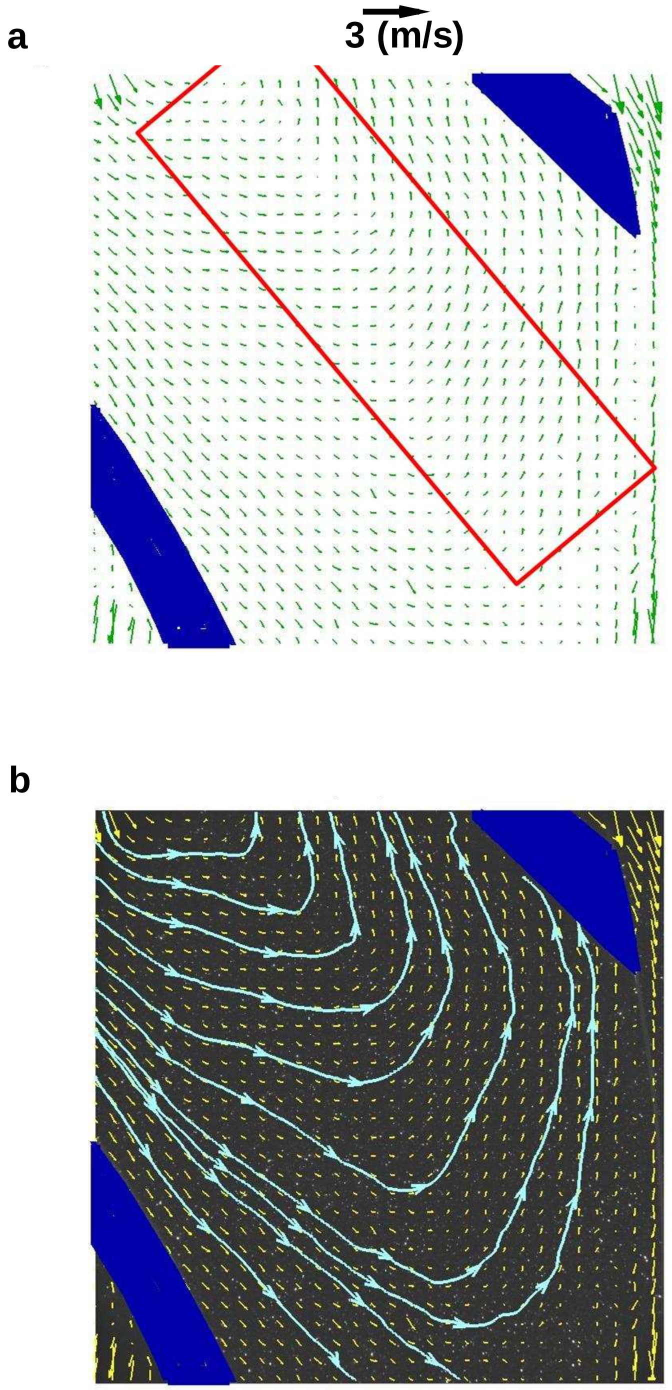

Figure 4.22: Mean relative velocity a) vector map and b) streamlines at the outlet at 40 % of design flow rate

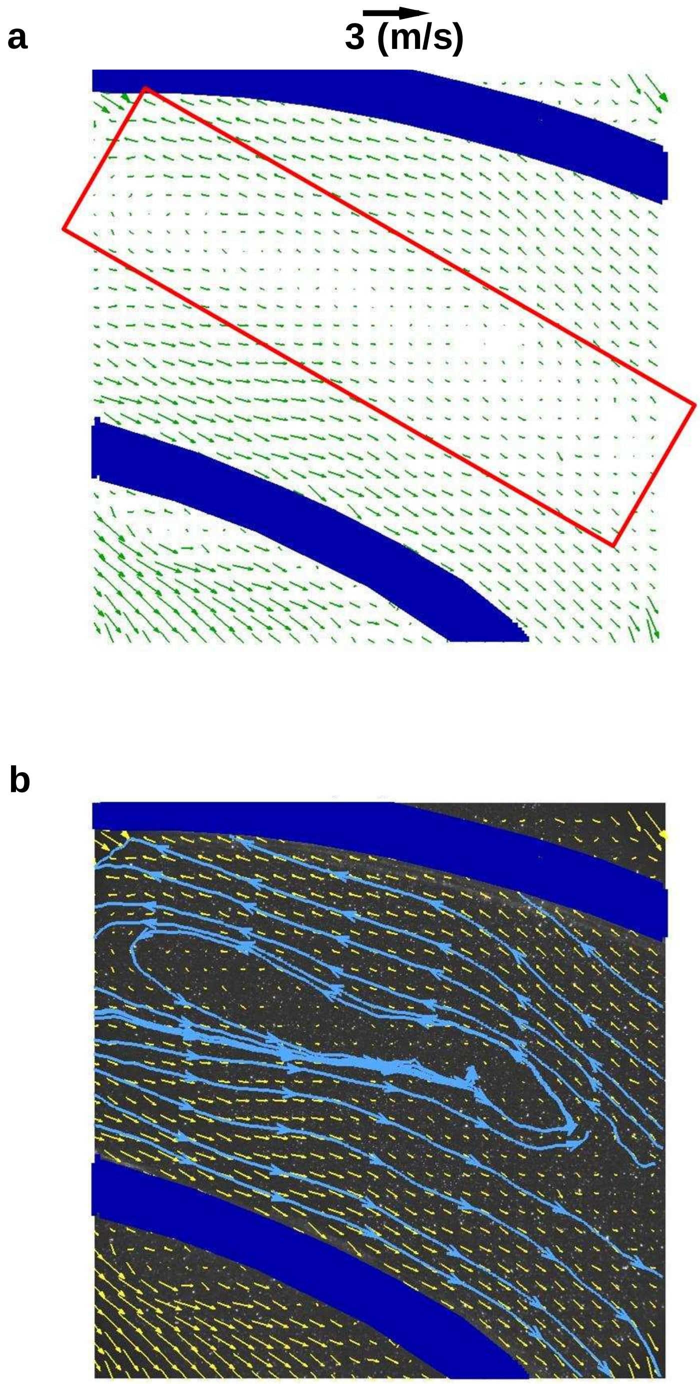

Figure 4.23: Mean relative velocity a) vector map and b) streamlines at the inlet at 30 % of design flow rate

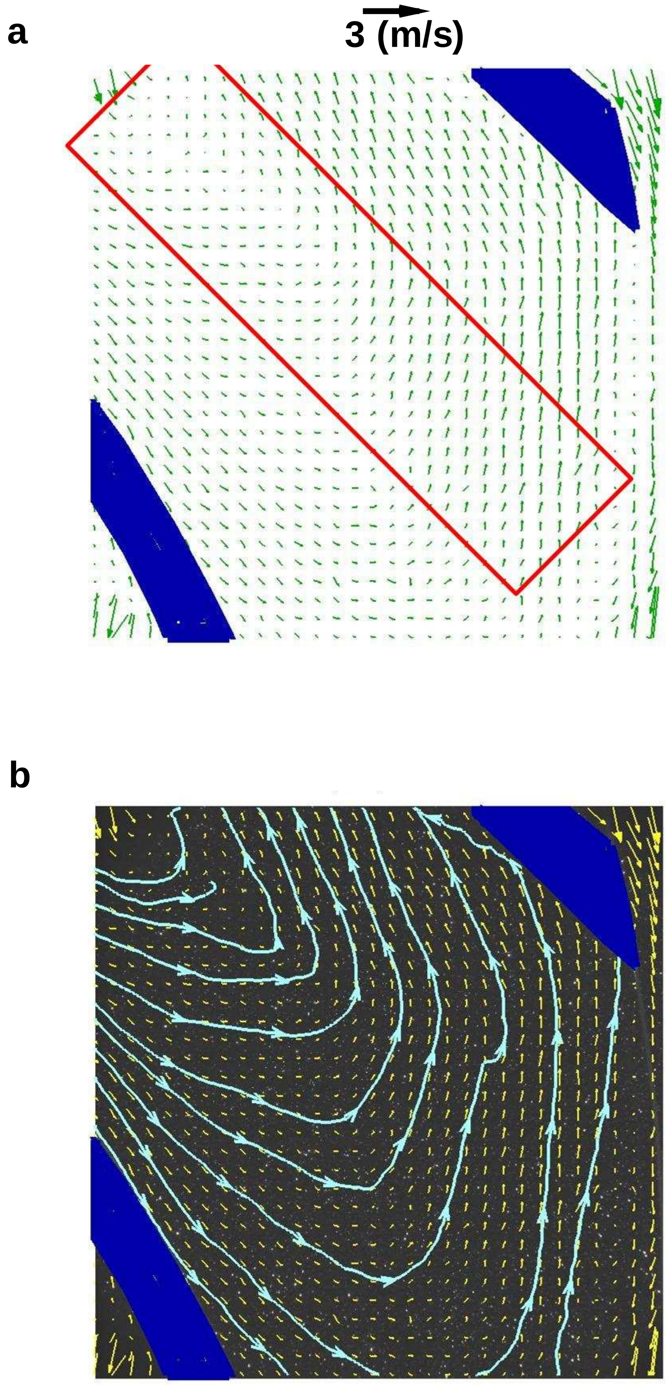

Figure 4.24: Mean relative velocity a) vector map and b) streamlines at the outlet at 30 % of design flow rate

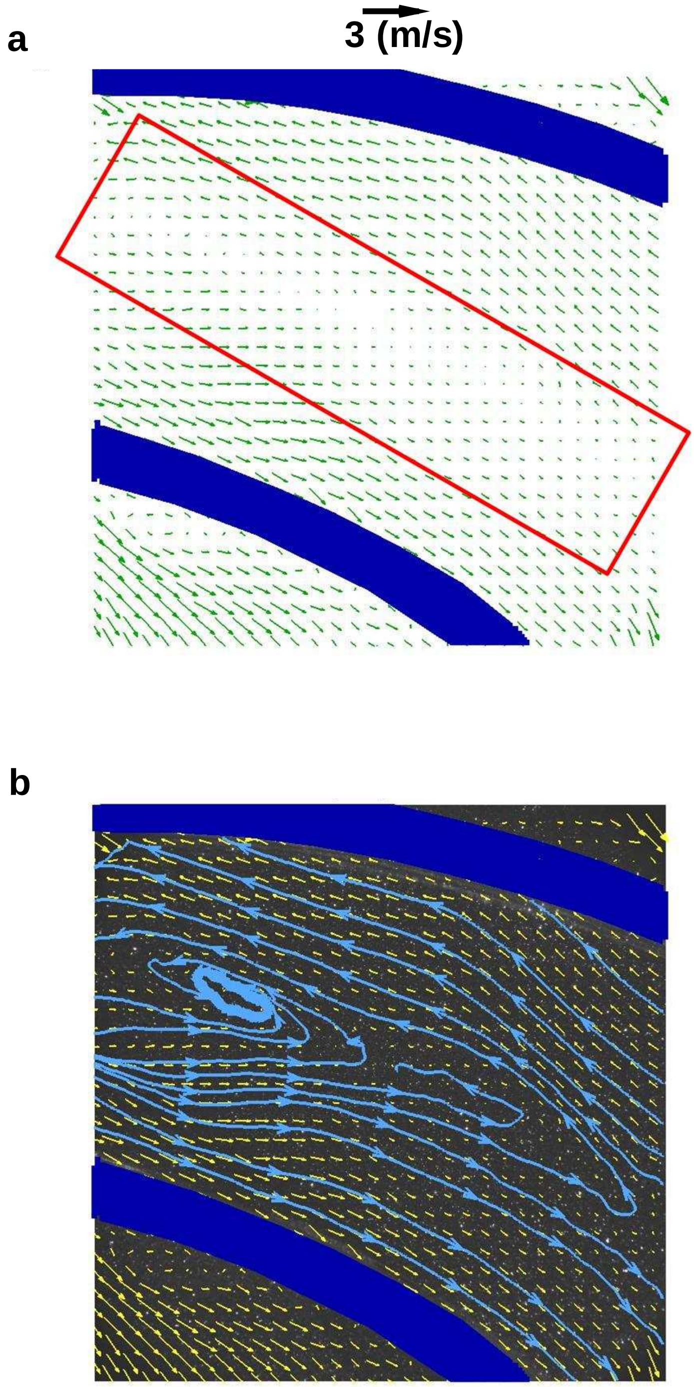

Figure 4.25: Mean relative velocity a) vector map and b) streamlines at the inlet at 25 % of design flow rate

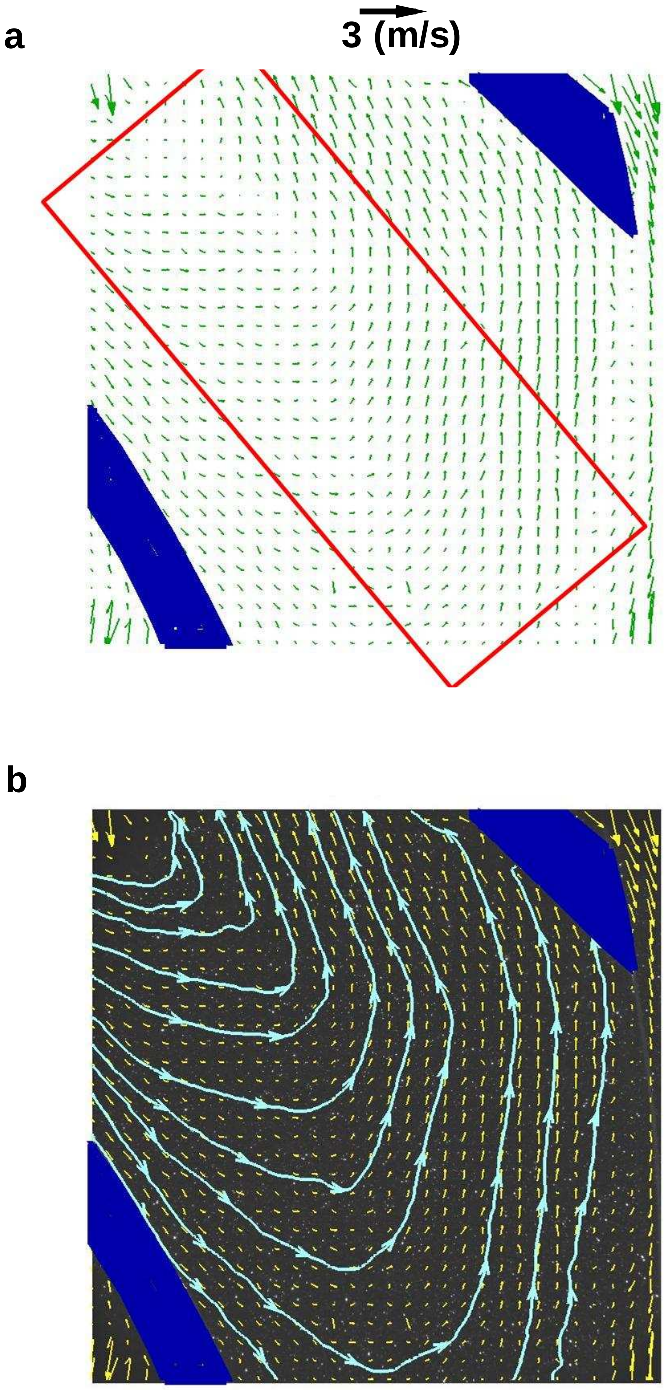

Figure 4.26: Mean relative velocity a) vector map and b) streamlines at the outlet at 25 % of design flow rate

the suction side of the impeller channel at 50% and 40% of the design flow rate. A large circulation occurred at flow rates of 30% and 25% of the design condition which caused circulation of the fluid inside the channel and the absence of through flow. In contrast, a smooth through flow from the inlet to the outlet was observed at the design condition (100% flow rate).

4.3.2.2 Instantaneous Relative Velocity

To determine if the eddies that form the recirculation area are stationary or moving, an investigation of those vortices in the instantaneous vector maps was performed for 25% of the design flow rate. Figure 4.27 to Figure 4.30 show the instantaneous vector maps sellected from the first 40 vector maps of the set that contains 1000 images. There was no clear pattern of movement of the vortices inside the impeller channel. Some vector maps show the existence of a single vortex at the inlet of the channel (Figure 4.27) while others show another vortex close to the mid passage of the channel (Figure 4.28). Furthermore, Figure 4.29 show two vortices at both the inlet and mid passage of the channel at the same time which matched the results of Behseta [27]. Figure 4.30 taken from the same set at the same flow rate shows that there are no complete vortices but flow patterns with a tendency to form eddies. This means that the flow behaviour at 25% of the design flow rate is not stationary but actually moving along the channel.

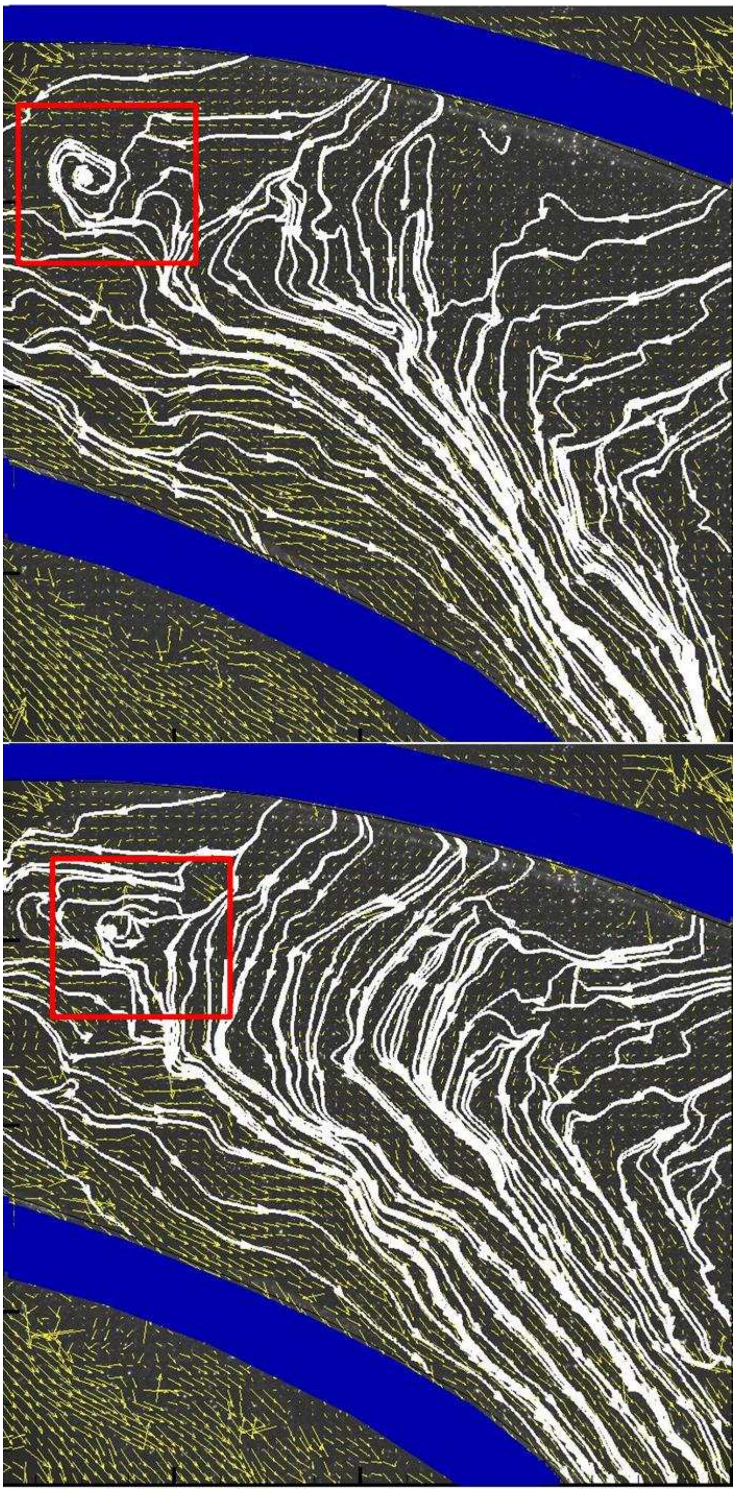

Figure 4.27: Instantaneous vendor maps for 25 % of design flow rate with a vortex at the inlet of the channel

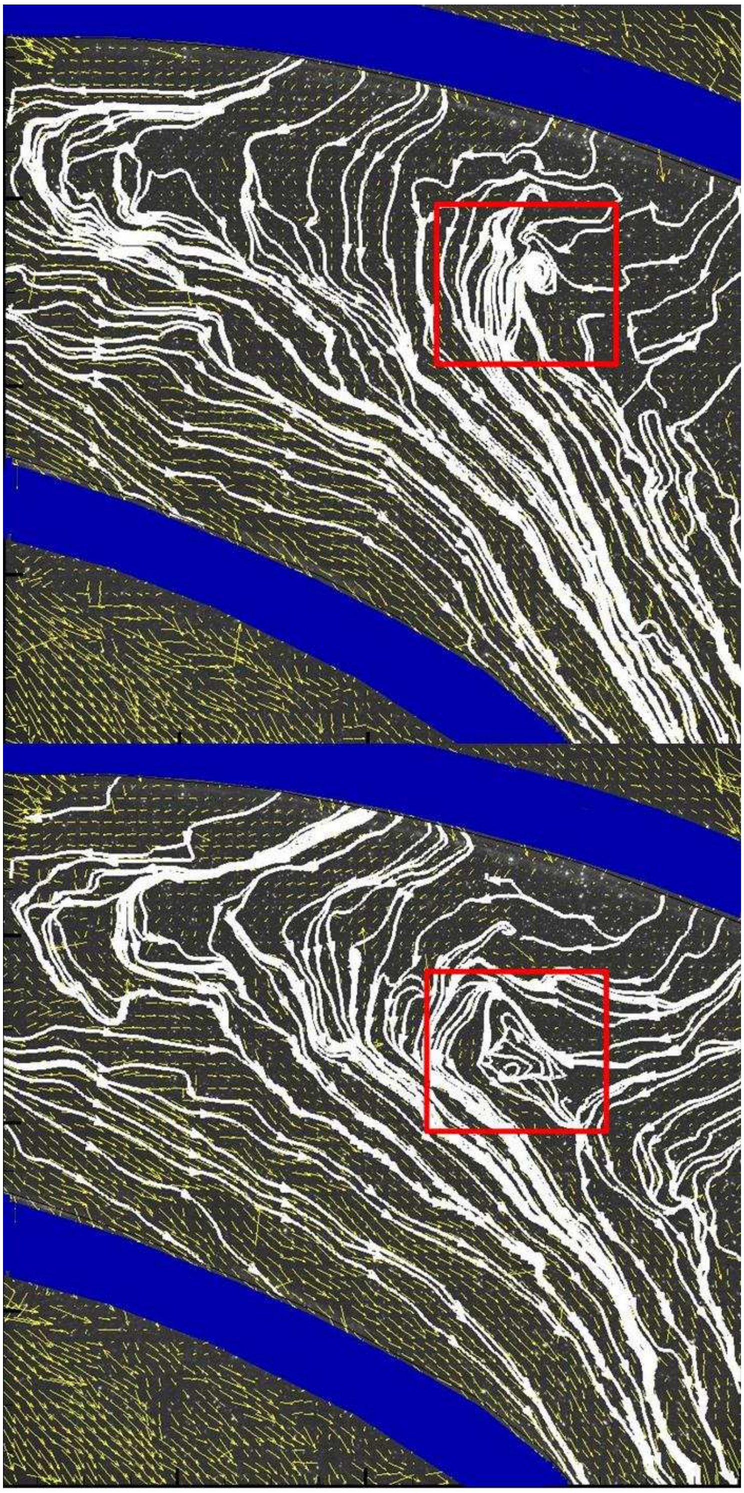

Figure 4.28: Instantaneous vendor maps for 25 % of design flow rate with a vortex at the mid channel

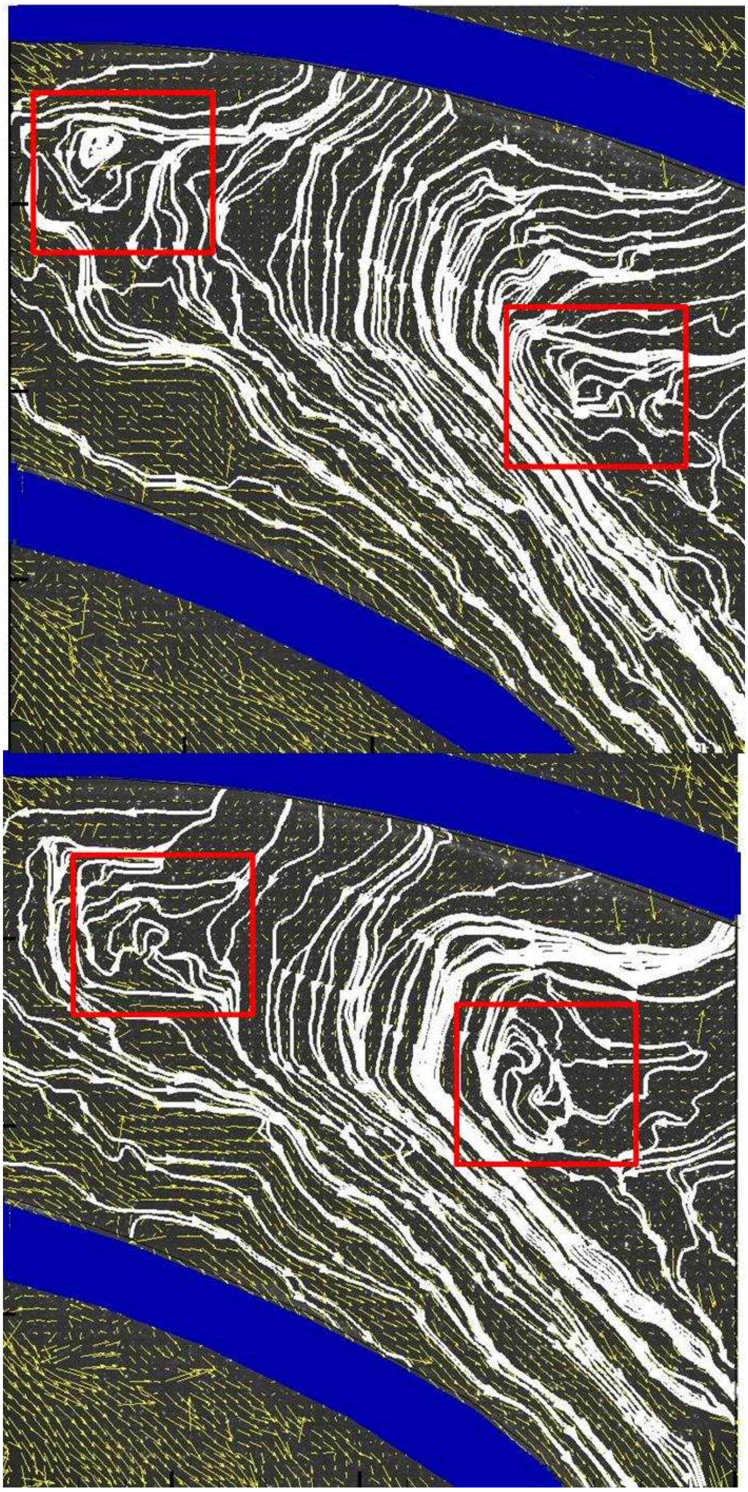

Figure 4.29: Instantaneous vendor maps for 25 % of design flow rate with two vortices at the inlet and mid channel

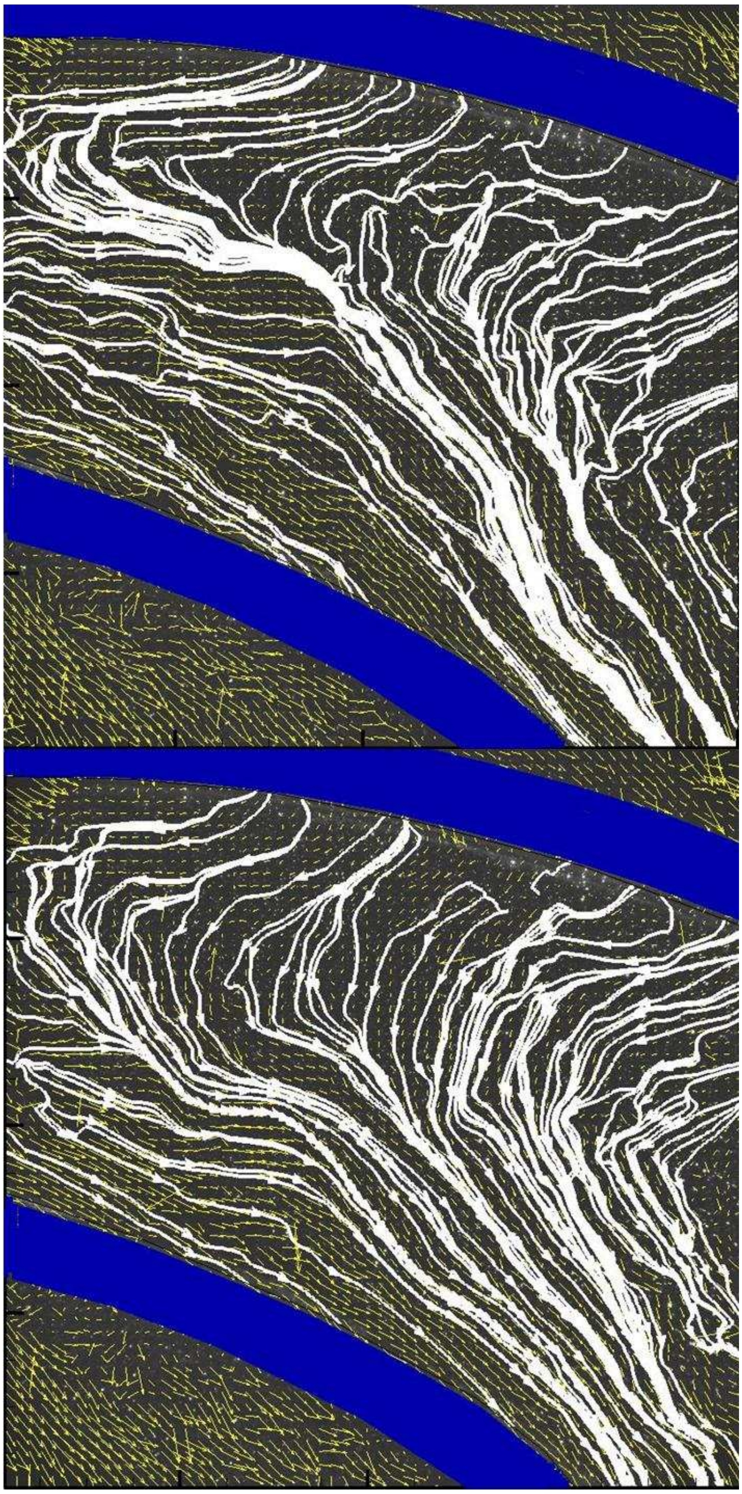

Figure 4.30: Instantaneous vendor maps for 25 % of design flow rate with no vortex inside the channel

4.3.2.3 Mean Normalized Primary and Secondary Velocity at Off-Design Flow Rate

Primary Velocity

Figure 4.31 shows the mean normalized primary velocity components at six different locations inside the impeller passage at 75% of the design flow rate. At the inlet of the channel (Figure 4.31 a), the magnitude of the primary velocity components increases from the pressure side to the suction side. A distortion in profile of the mean normalized primary velocity (in the form of a bell shape) was noticed at the inlet of the impeller due to the sudden change in the fluid direction from axial to radial. A slight decrease in the magnitude of the primary velocity happens in the mid channel due to the effect of the suction side boundary layer combined with the reduction in magnitude of the relative velocity as a result of the change in the angle of attack. The same scenario happens at 152 mm and 165 mm with a general decline in the profile of the primary velocity as it moves through the channel (Figure 4.31 b and Figure 4.31 c). Calculated from the outlet frame, the same decline in magnitude of the primary velocity is noticed but with no significant increase from the pressure side to the suction side (Figure 4.31 d and Figure 4.31 e). At the exit of the channel which is represented by a radius of 229 mm, the primary velocity remains in the same range it started with on the pressure side but it decreases significantly when it approaches the suction side (Figure 4.31 f). This agrees with the separation observed earlier in Figure 4.18. There is no negative primary component measured throughout the whole channel at 75% of the design flow rate which means the absence of reverse flow.

At 50% of the design flow rate, the increasing pattern was only observed close to the inlet of the channel at radius 140 mm probably due to inlet distortion(Figure 4.32 a). At radii 152 mm, 165 mm, 191 mm and 216 mm the primary velocity is the highest close to the pressure side (Figure 4.32 b, c and d) and starts decreasing until a reverse in flow is noticed very close to the blade wall at the suction side (Figure 4.32 e). Figure 4.32 f represents the exit of the channel where the same pattern of high primary velocity close to the pressure side that decreases as it gets closer to the suction side is noticed from the negative values measured. The sudden change in the flow direction very close to the suction side at radius 229 mm is due to the slip of fluid just at the tip of the blade towards the exit of the impeller passage. There is still no complete eddy or recirculations of the flow throughout the whole channel at this percentage of the design flow rate except at locations very close to the blade suction side starting from the mid way of the passage. The positive values of the primary velocity at the pressure side indicate that fluid is passing to the outside of the channel at the area close to the pressure side which was also shown previously in Figure 4.20.

At 40% of the design flow rate, all the primary velocity profiles throughout the channel passage are decreasing from the pressure side to the suction side (Figure 4.33). The inlet portion is definitely affected by the large change in the relative velocity angle of attack but with no evidence of inflow to the inlet of the channel (Figure 4.33 a). Unlike the case of 50% of the design flow rate, the fluid flowing inward to the inlet of the channel is shifting more towards the centre of the channel passage where the negative values are spotted away from the suction side at 152 mm and almost from the mid channel at 229 mm (Figure 4.33 b, c, d, e and f).

A complete recirculation indicating the presence of a stalled channel is noticed throughout the whole channel passage from the inlet to the outlet at 30% of the design flow rate (Figure 4.34). All velocity profiles experience a change from positive values at the pressure side (flowing outward) to negative values at the suction side (flowing inward). This change in sign and, therefore, direction starts from the last third at the inlet of the channel and then propagates and shifts towards the mid channel where the change in direction happens almost at the mid channel passage at 229 mm (Figure 4.34 f).

The same flow behaviour observed at 30% of the design flow occurs at one quarter (25%) of the design flow rate. The only difference noticed is the general reduction in the magnitude of the primary velocity profiles, when compared to that at 30%, at all the locations inside the channel. This reduction causes a minor shift towards the centre of the channel passage for the location where the flow direction changes (Figure 4.35).

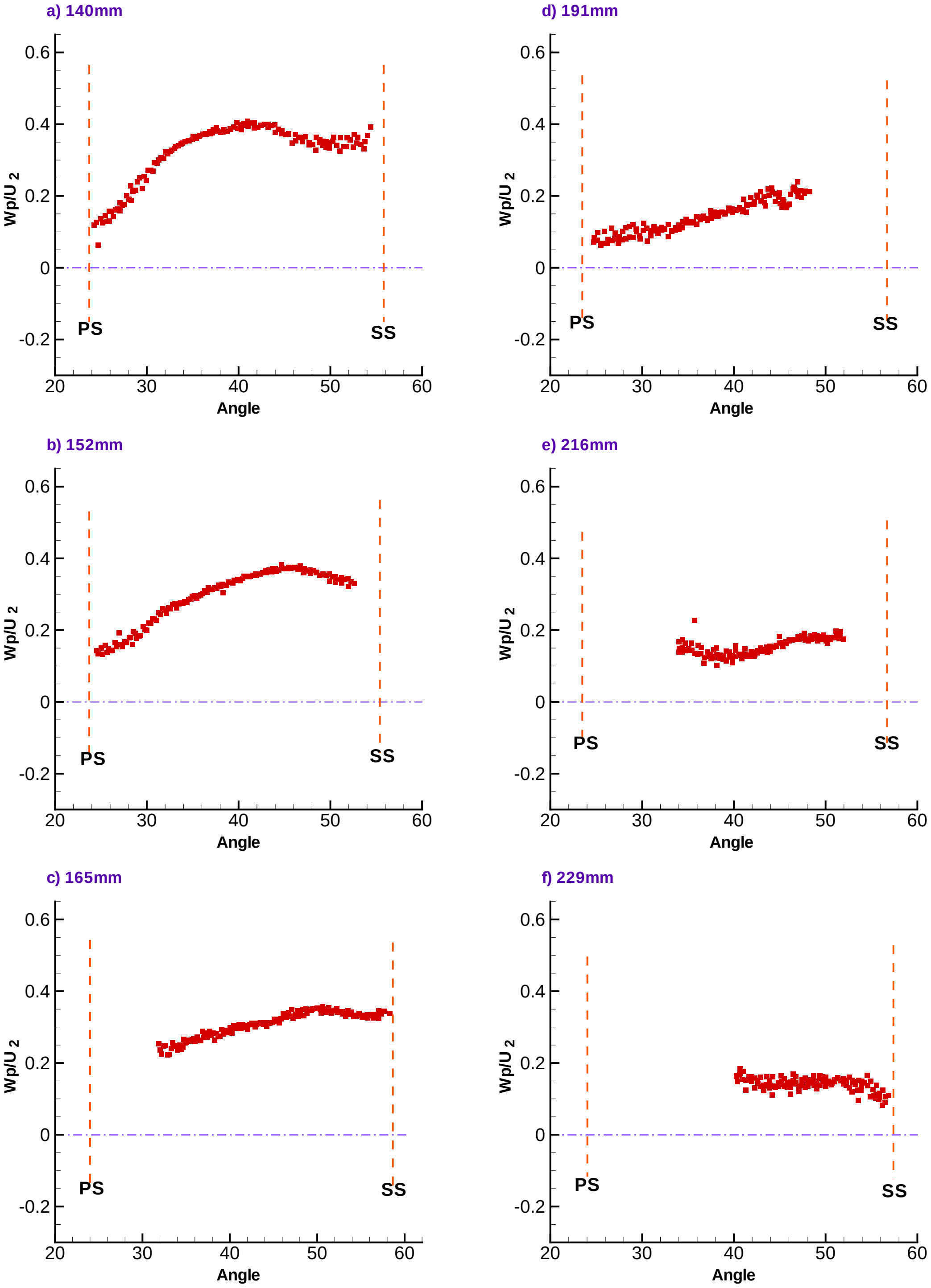

Figure 4.31: Mean normalized primary velocity for 75 % of design flow rate at a) 140 mm, b) 152 mm, c) 165 mm, d) 191 mm, e) 216 mm and f) 229 mm

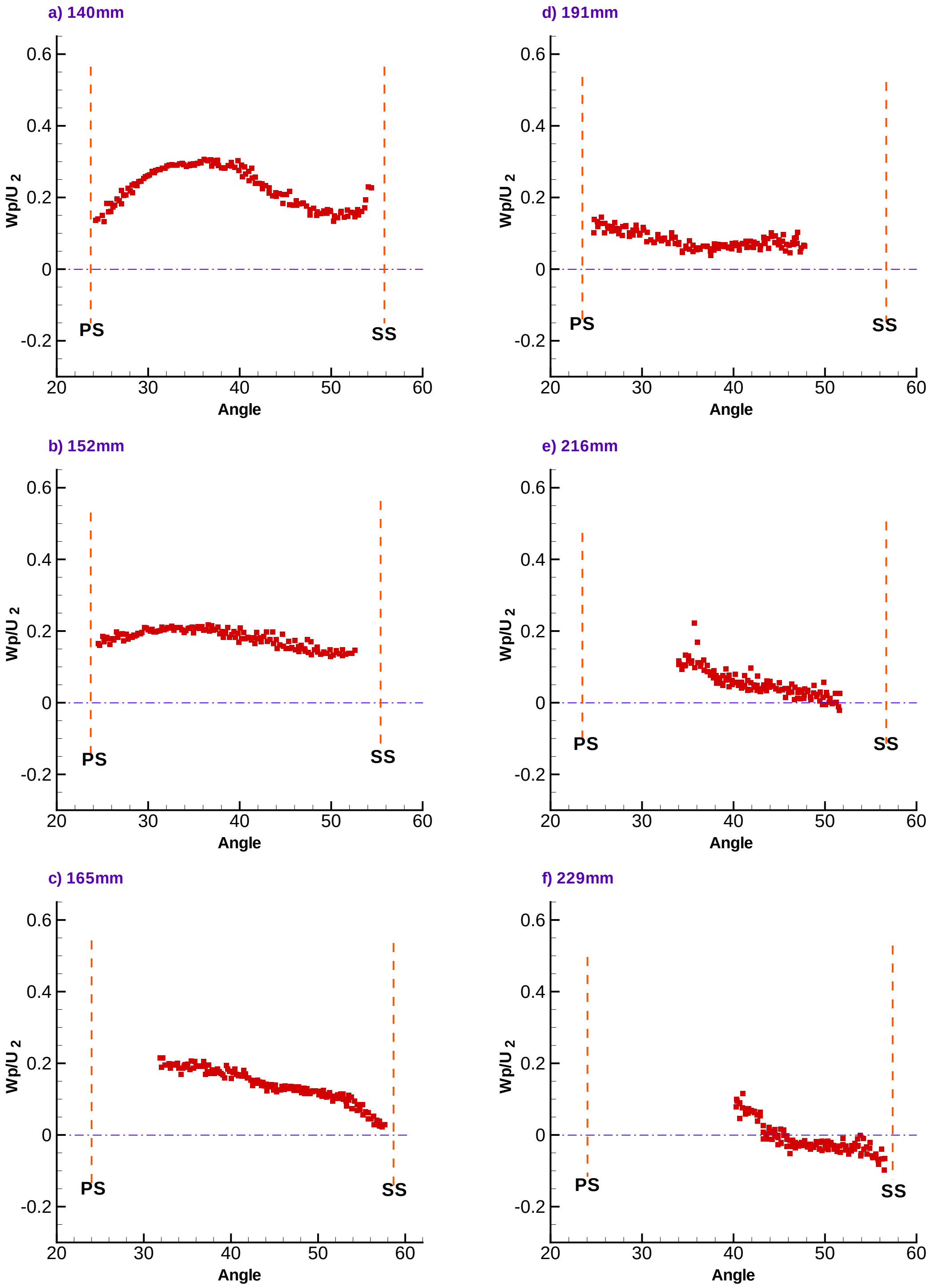

Figure 4.32: Mean normalized primary velocity for 50 % of design flow rate at a) 140 mm, b) 152 mm, c) 165 mm, d) 191 mm, e) 216 mm and f) 229 mm

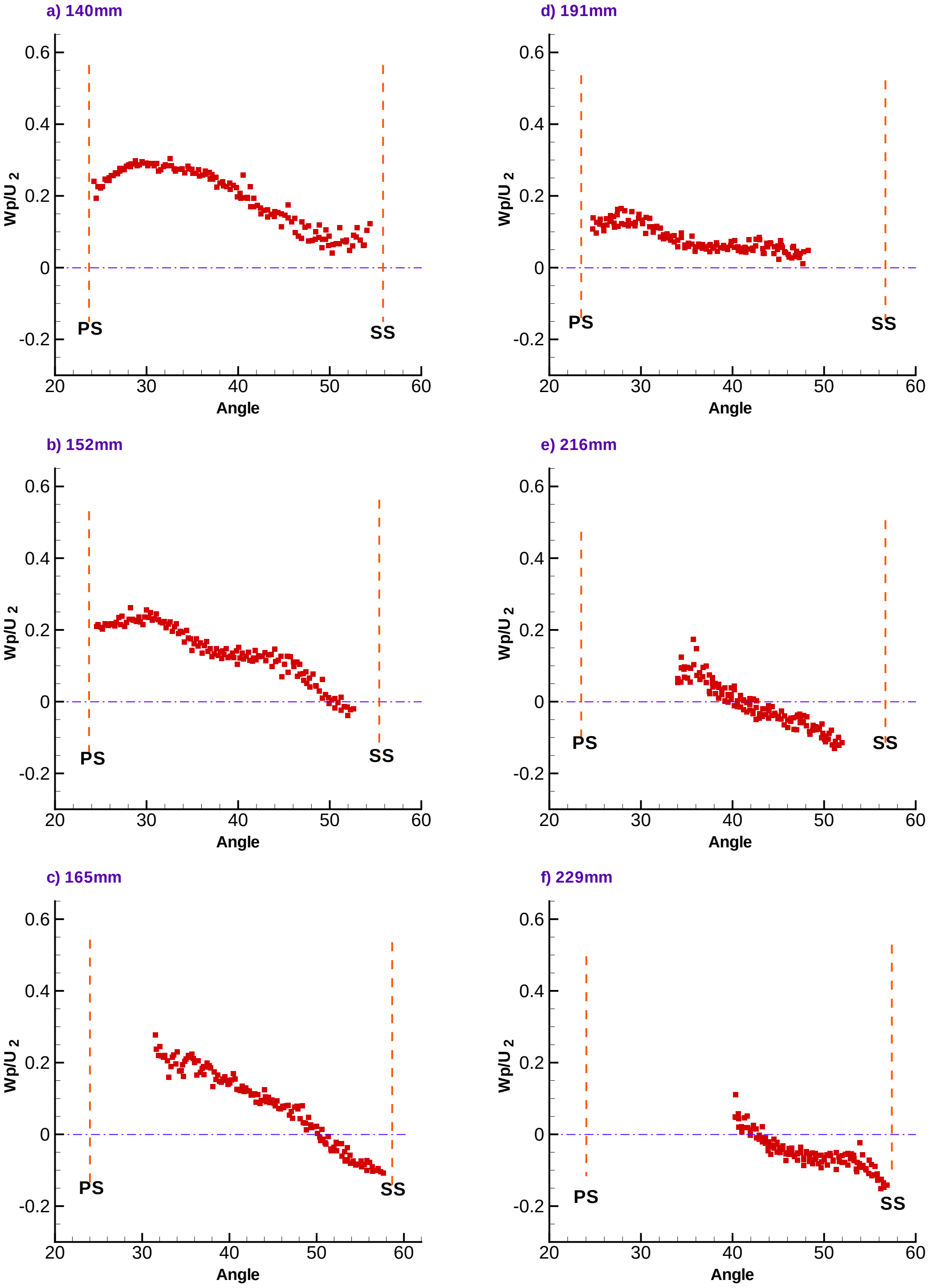

Figure 4.33: Mean normalized primary velocity for 40 % of design flow rate at a) 140 mm, b) 152 mm, c) 165 mm, d) 191 mm, e) 216 mm and f) 229 mm

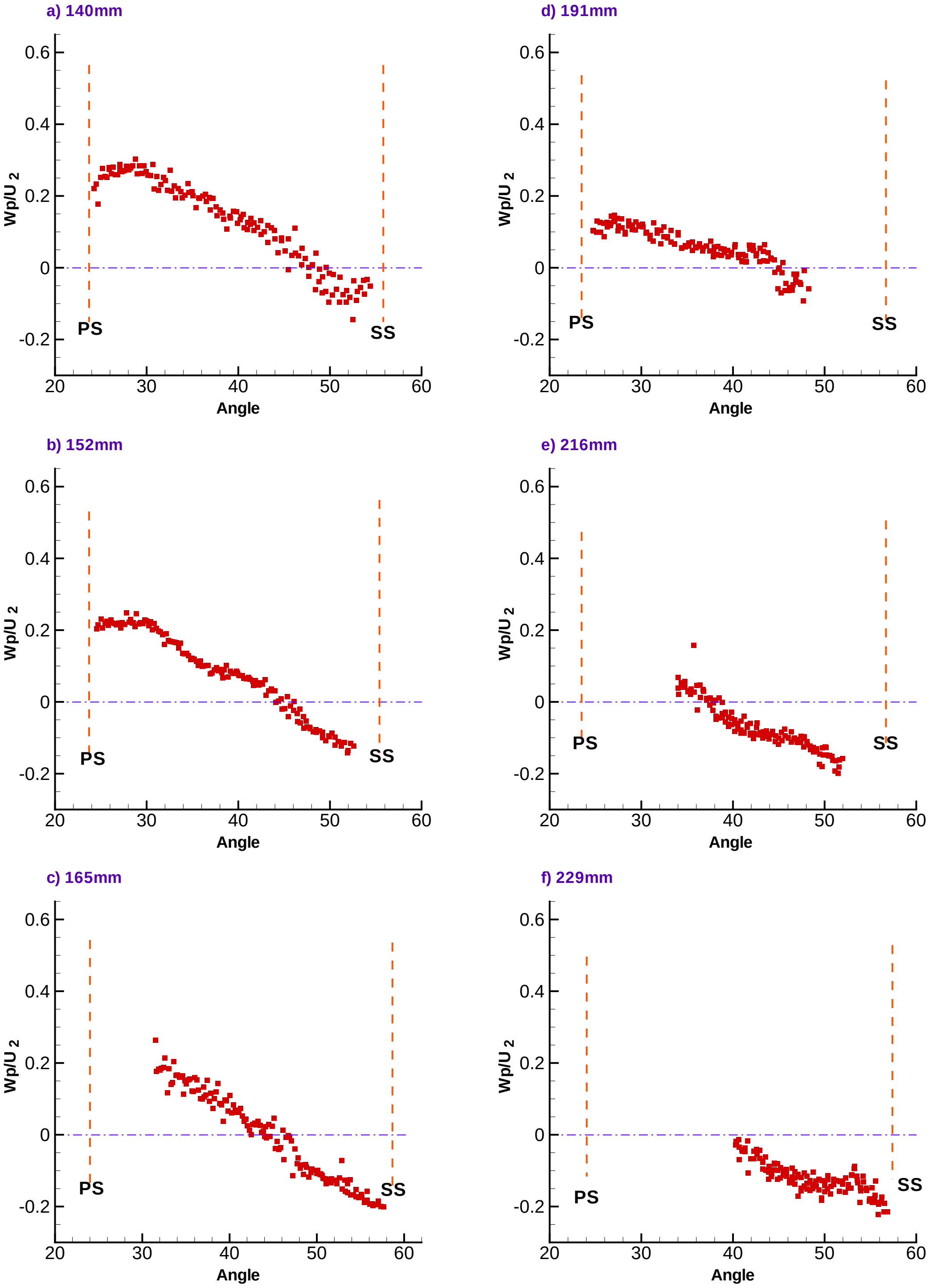

Figure 4.34: Mean normalized primary velocity for 30 % of design flow rate at a) 140 mm, b) 152 mm, c) 165 mm, d) 191 mm, e) 216 mm and f) 229 mm

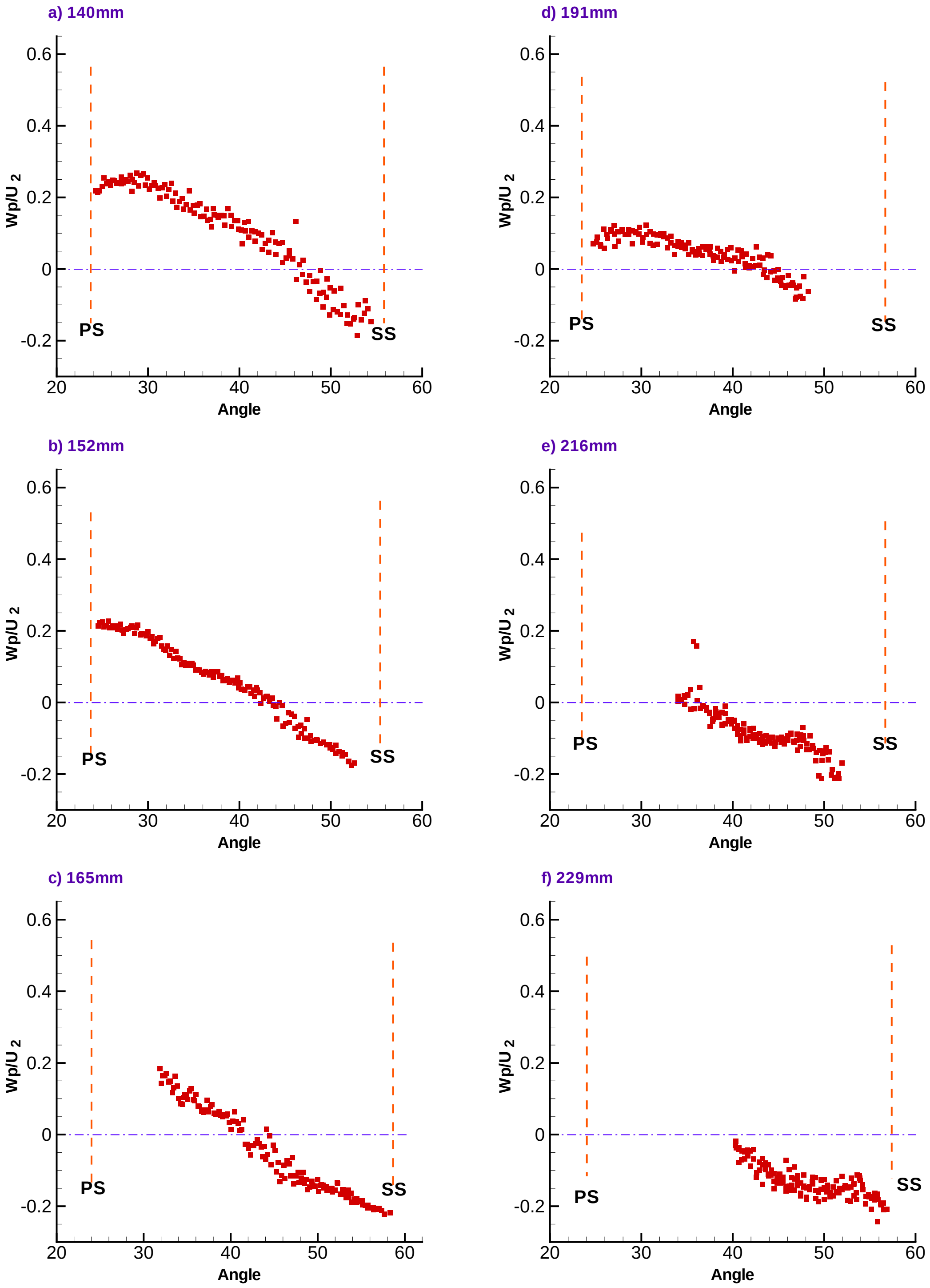

Figure 4.35: Mean normalized primary velocity for 25 % of design flow rate at a) 140 mm, b) 152 mm, c) 165 mm, d) 191 mm, e) 216 mm and f) 229 mm

Another way to represent the data is by observing the effect of the flow rate change on each location inside the impeller (Figure 4.36 to Figure 4.41). In summary, as the flow rate decreases, the flow behaviour inside the impeller channel deviates from the flow phenomena described in Chapter 1. Furthermore, as the flow rate decreases, the path of the formed vortices moves from the suction side where it initially started to the middle channel passage. It was noticed that even when the reduction in the flow reaches 40% of the design flow rate, some fluid still passes through the channel very close to the pressure side. At flows of 30% and 25% of the design flow rate the channel is completely stalled with a reversed flow reaching the inlet of the channel.

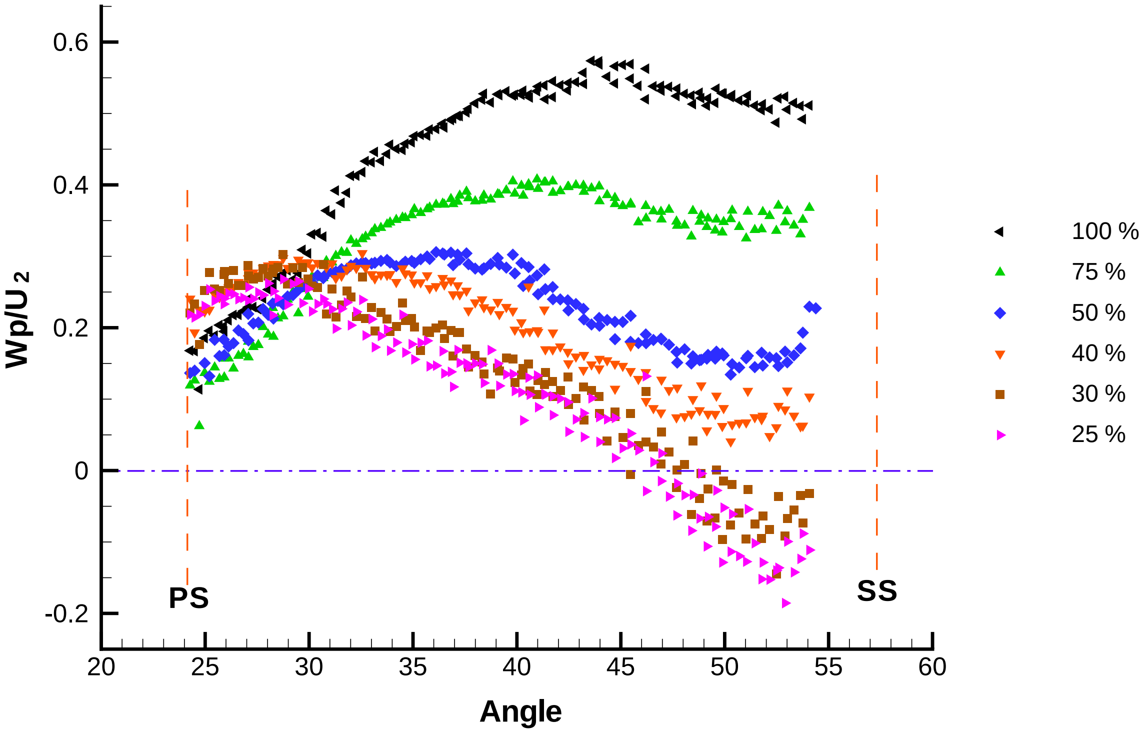

Figure 4.36: Mean normalized primary velocity at r = 140 mm for 100 %, 75 %, 50 %, 40 %, 30 % and 25 % of design flow rate

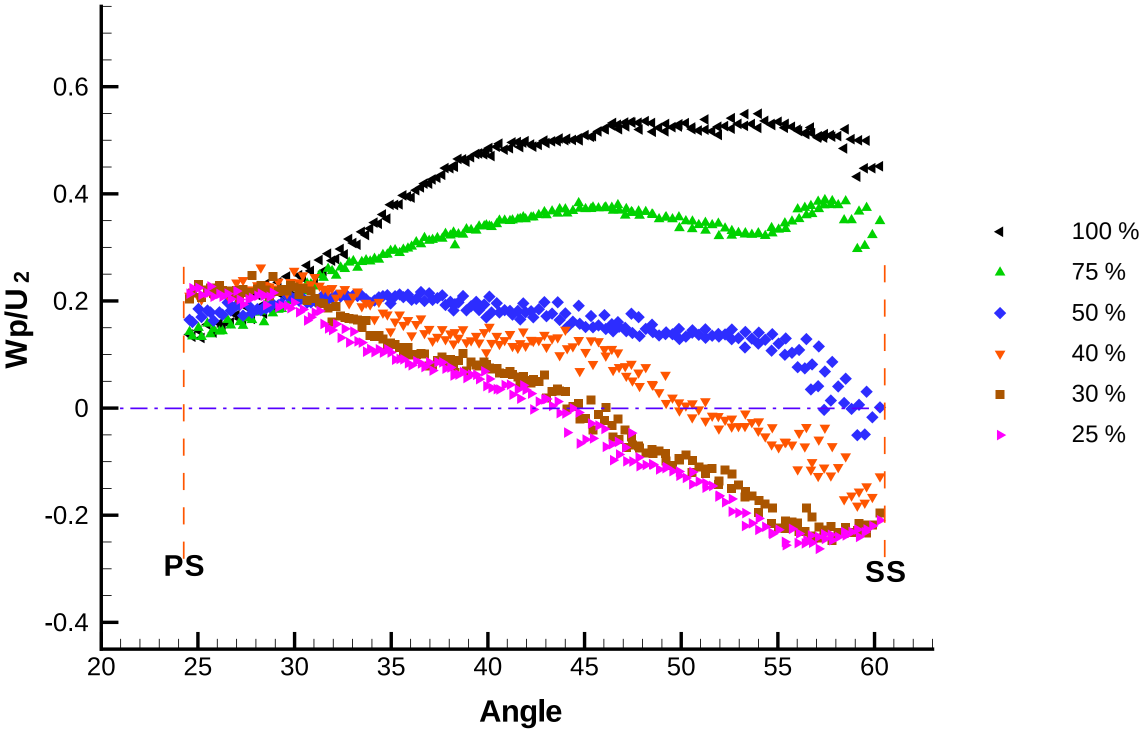

Figure 4.37: Mean normalized primary velocity at r = 152 mm for 100 %, 75 %, 50 %, 40 %, 30 % and 25 % of design flow rate

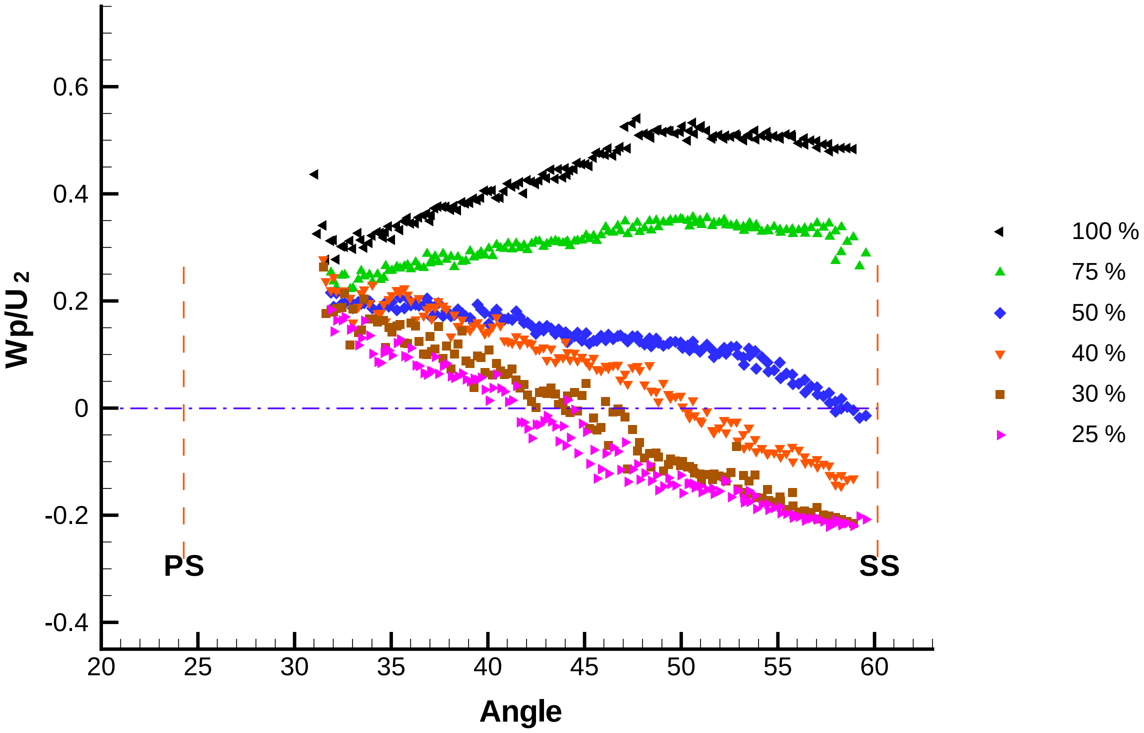

Figure 4.38: Mean normalized primary velocity at r = 165 mm for 100 %, 75 %, 50 %, 40 %, 30 % and 25 % of design flow rate

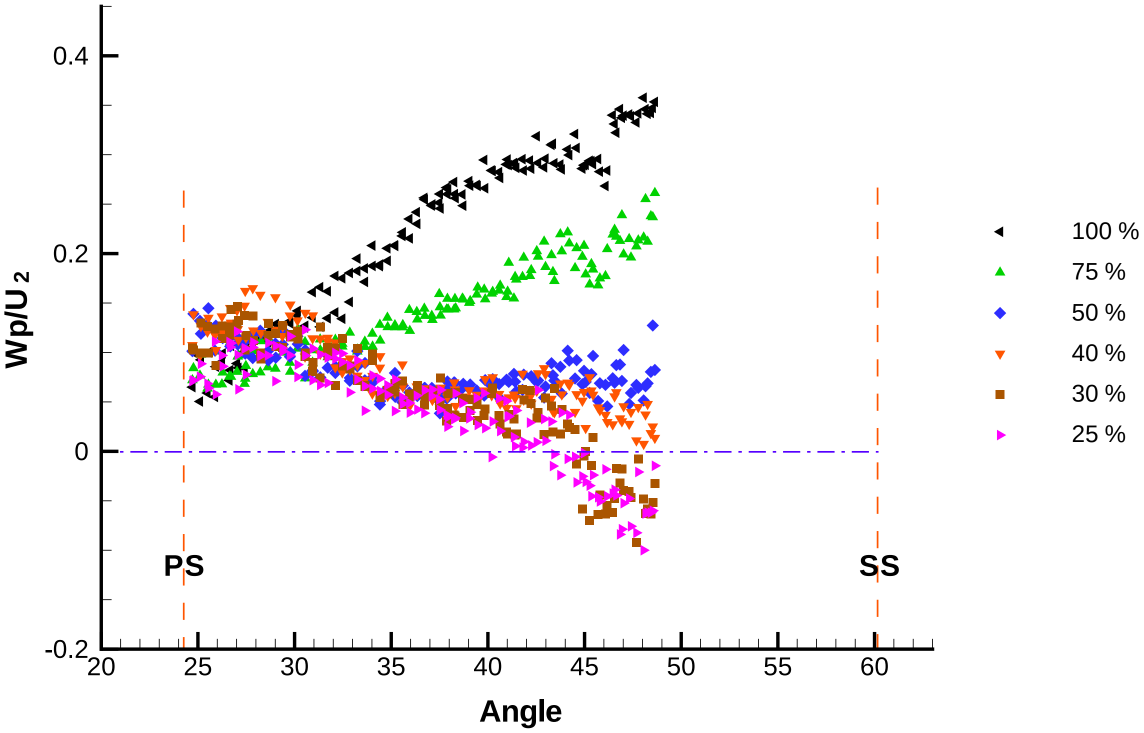

Figure 4.39: Mean normalized primary velocity at r = 191 mm for 100 %, 75 %, 50 %, 40 %, 30 % and 25 % of design flow rate

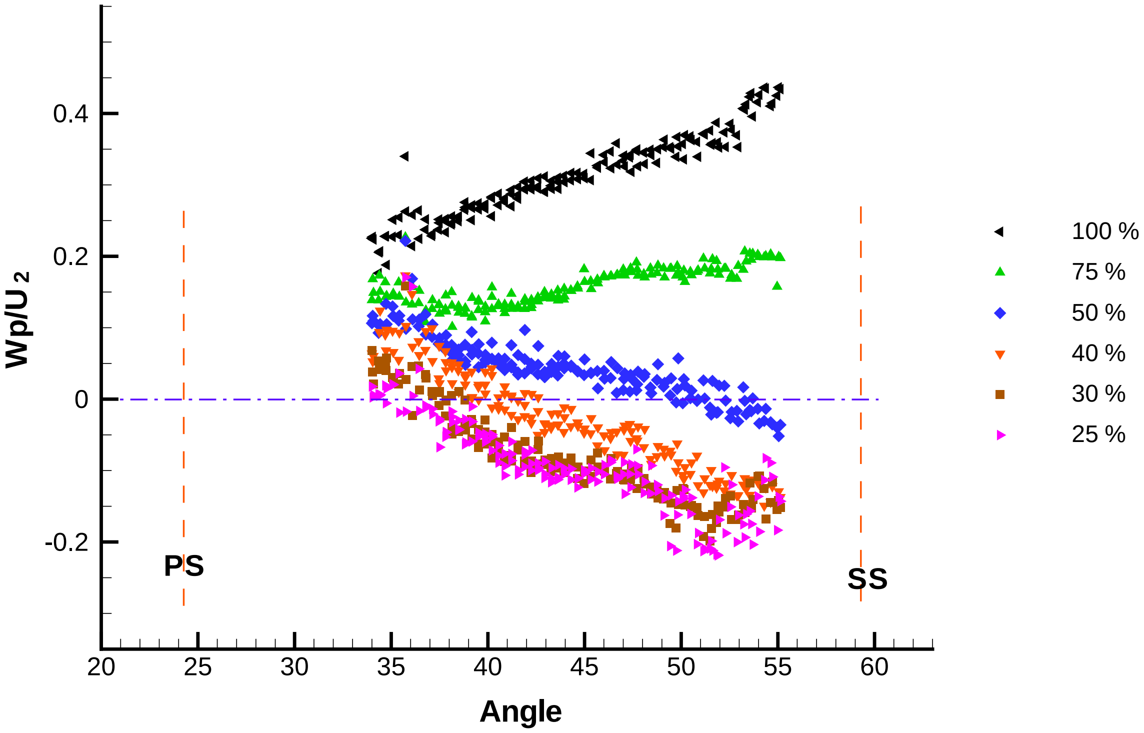

Figure 4.40: Mean normalized primary velocity at r = 216 mm for 100 %, 75 %, 50 %, 40 %, 30 % and 25 % of design flow rate

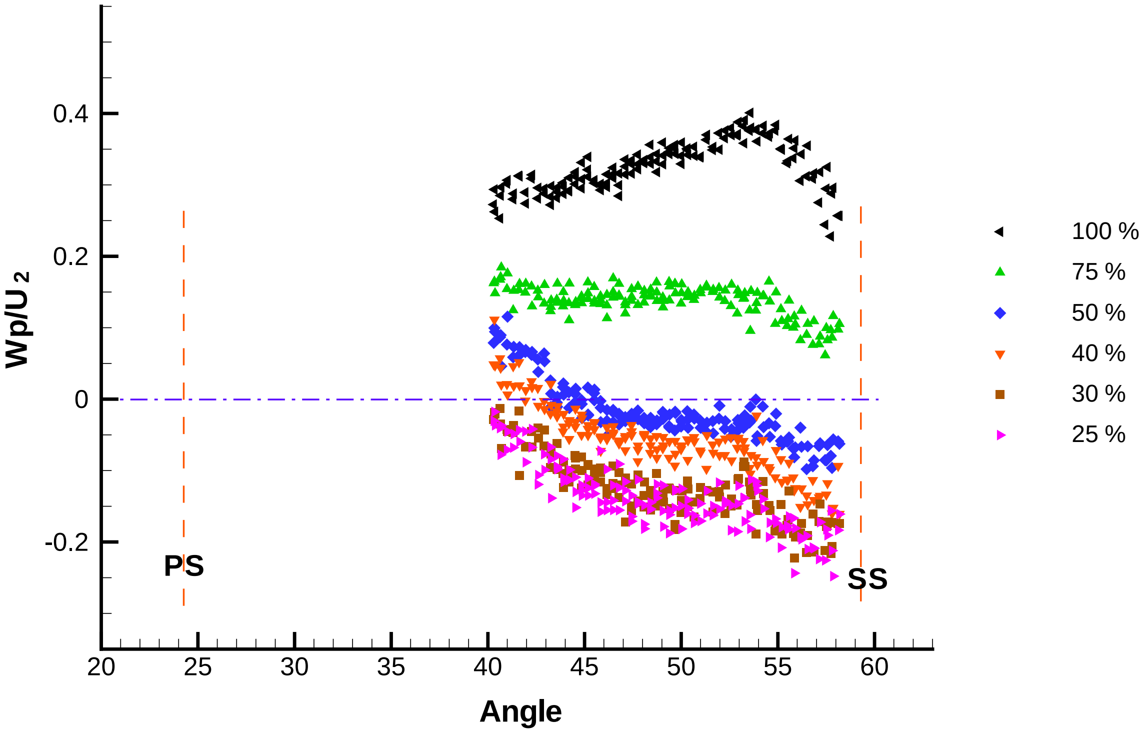

Figure 4.41: Mean normalized primary velocity at r = 229 mm for 100 %, 75 %, 50 %, 40 %, 30 % and 25 % of design flow rate

Looking at the previous results, it was noticed that the mean normalized primary velocity profile for both the design condition and 75% flow rate were positive throughout the whole channel. This indicated the absence of any inward flow at those conditions. At 50% and 40% flow rates, inward flow was observe at the exit of the channel where the values of the mean normalized primary velocity were negative. In contrast to the 100% flow rate, inward flow from the outlet to inlet of the channel close to the suction side was observed at 30% and 25% of the design flow rate.

Secondary Velocity

Knowing that the magnitude of the normalized secondary velocity is very small when compared to the normalized primary velocity, large fluctuations were anticipated in the profile of the normalized secondary velocity at off-design flow rates.

In Figure 4.42, the normalized secondary velocity at six different locations inside the channel is presented for 75% of the design flow rate. The fluid direction at all locations was very similar to the design condition case (Figure 4.14) with higher variations in the magnitude observed at locations close to the suction side.

As expected, the variation of the secondary velocity direction were clear and repetitive in the case of 50% design flow rate (Figure 4.43). This was due to the existence of the recirculation zone close to the suction side and its propagation as it moved towards the channel exit. It was hard to define a clear pattern in this case.

A comparison of the mean normalized secondary velocity flow is more meaningful and this is shown in Figure 4.44 to Figure 4.49. In Figure 4.44, the secondary velocity at the inlet of the channel, 140 mm, was in the direction of the suction side at 75% of the design flow rate with disturbances in the direction when it approached the blade wall at the suction side. When the flow rate was reduced to 50% of the design flow rate, the separation occured at the suction side affected the direction of the secondary velocity vectors. The same occured at 40%, 30% and 25% of the design flow rate.

At 152 mm from the centre of the impeller (Figure 4.45), the effect of the separation that occurred at 75% of the flow became clearer and caused some disturbances as it approached the suction side. At lower flow rates, the tendency of the fluid to move towards the suction side was limited by the recirculation formed near the suction side.

At mid passage of the impeller, 165 mm, the effect of separation grew at 75% of the flow rate (Figure 4.46). At lower flow rates, the fluid was almost following the dominant primary velocity and maintained close-to-zero values.

Just past the mid way of the channel (Figure 4.47), the secondary velocity profile at 75% of the design flow rate was behaving similar to the design flow rate case with negative values close to the pressure side turning to positive as it approached the suction side. As the flow was decreased below 50% of the design flow rate, the fluid moved away from the pressure side due to the effect of the big circulation that moved radialy towards the suction side as demonstrated earlier by the streamlines (Figure 4.20, Figure 4.22, Figure 4.24 and Figure 4.26).

Close to the outlet of the channel (at 216 mm from the centre of the impeller), the fluid changed its direction from the pressure side and started moving towards the pressure side as the flow rate was decreased (Figure 4.48). The opposite occurred in the part of the passage close to the suction side in which the tendency of the fluid to slip to the outside of the channel (positive secondary velocity values) changed to a flow moving away from the suction side and when combined with the primary it showed a flow moving inward.

The pattern of the secondary velocity profile at 216 mm was repeated at 229 mm away from the centre (Figure 4.49). The only noticeable difference between the two locations was the increase in the range of change of the secondary profile from the pressure side to the suction side.

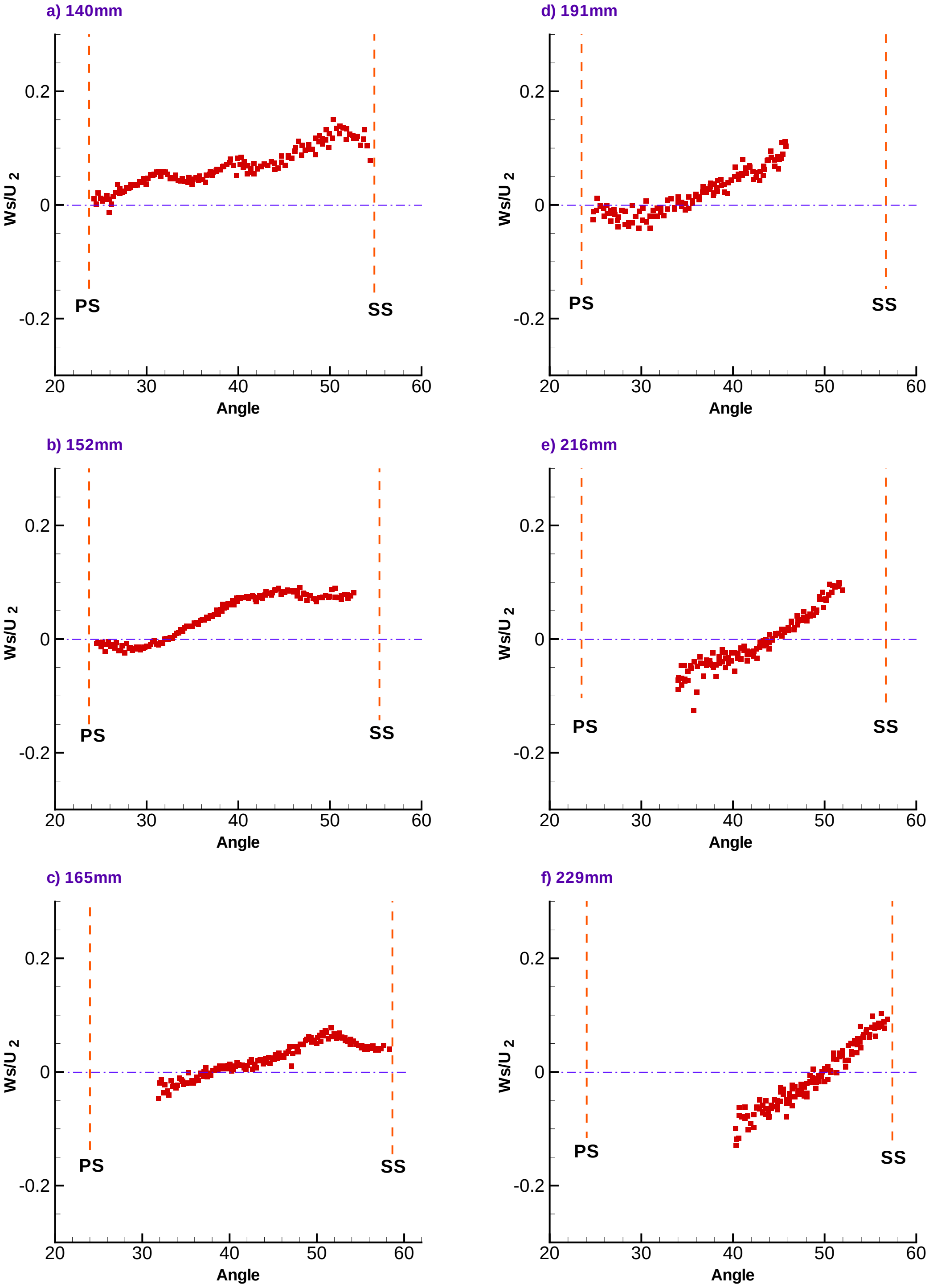

Figure 4.42: Mean normalized secondary velocity for 75 % of design flow rate at a) 140 mm, b) 152 mm, c) 165 mm, d) 191 mm, e) 216 mm and f) 229 mm

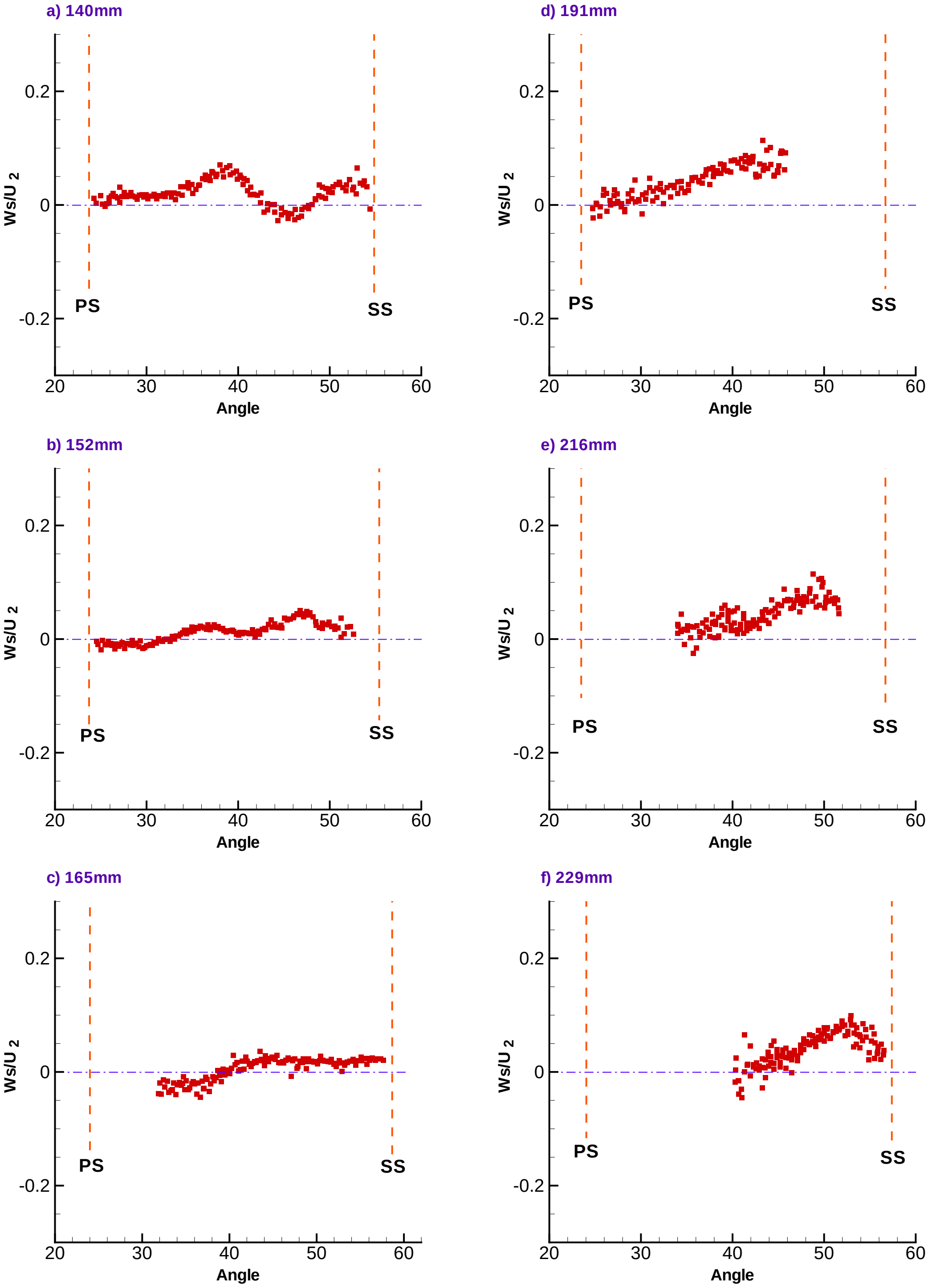

Figure 4.43: Mean normalized secondary velocity for 50 % of design flow rate at a) 140 mm, b) 152 mm, c) 165 mm, d) 191 mm, e) 216 mm and f) 229 mm

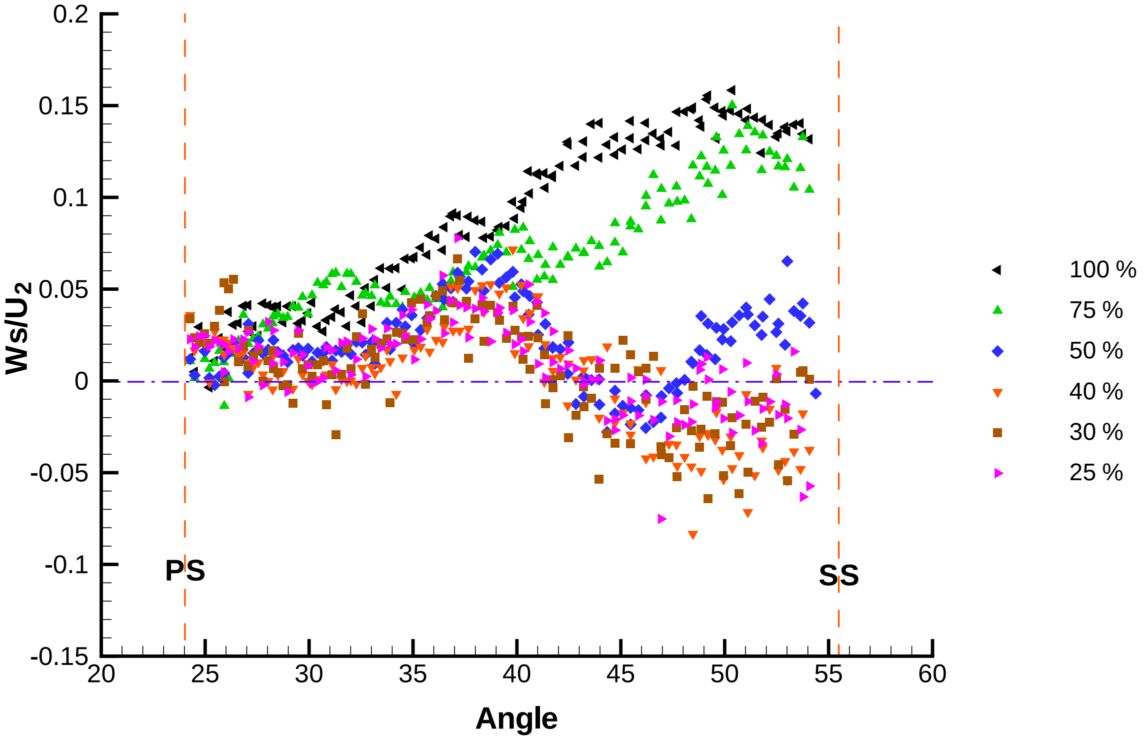

Figure 4.44: Mean normalized secondary velocity at r = 140 mm for 100 %, 75%, 50%, 40%, 30% and 25% of design flow rate

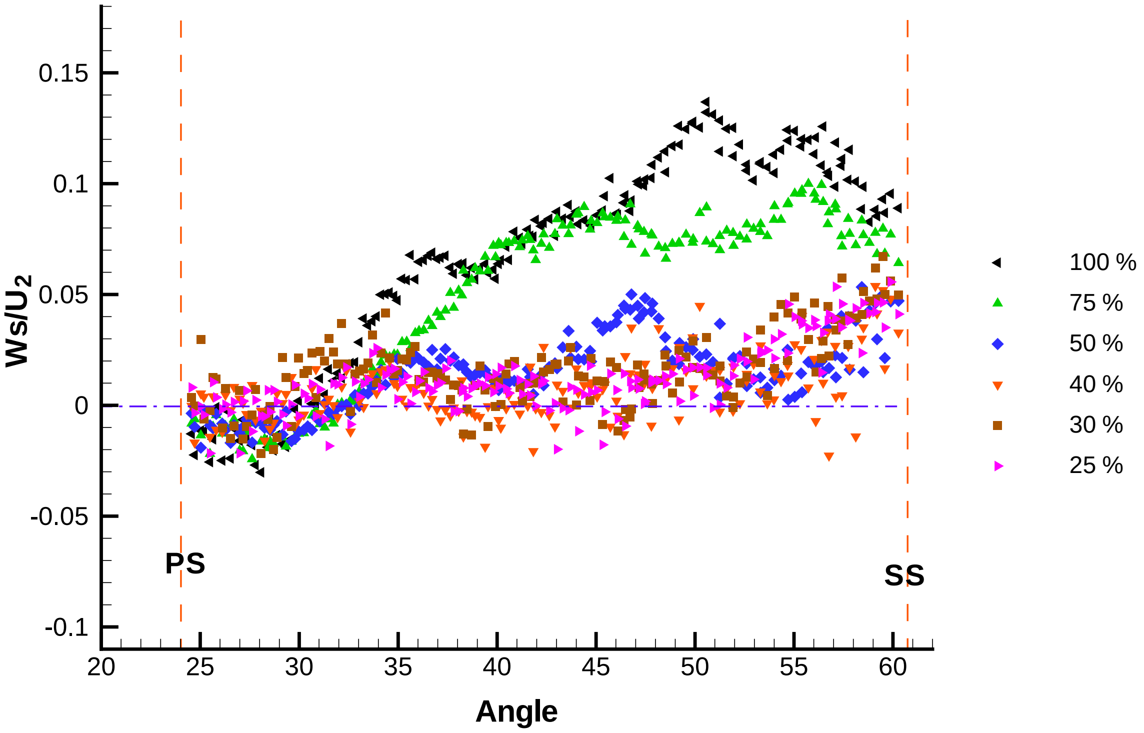

Figure 4.45: Mean normalized secondary velocity at r = 152 mm for 100 %, 75%, 50%, 40%, 30% and 25% of design flow rate

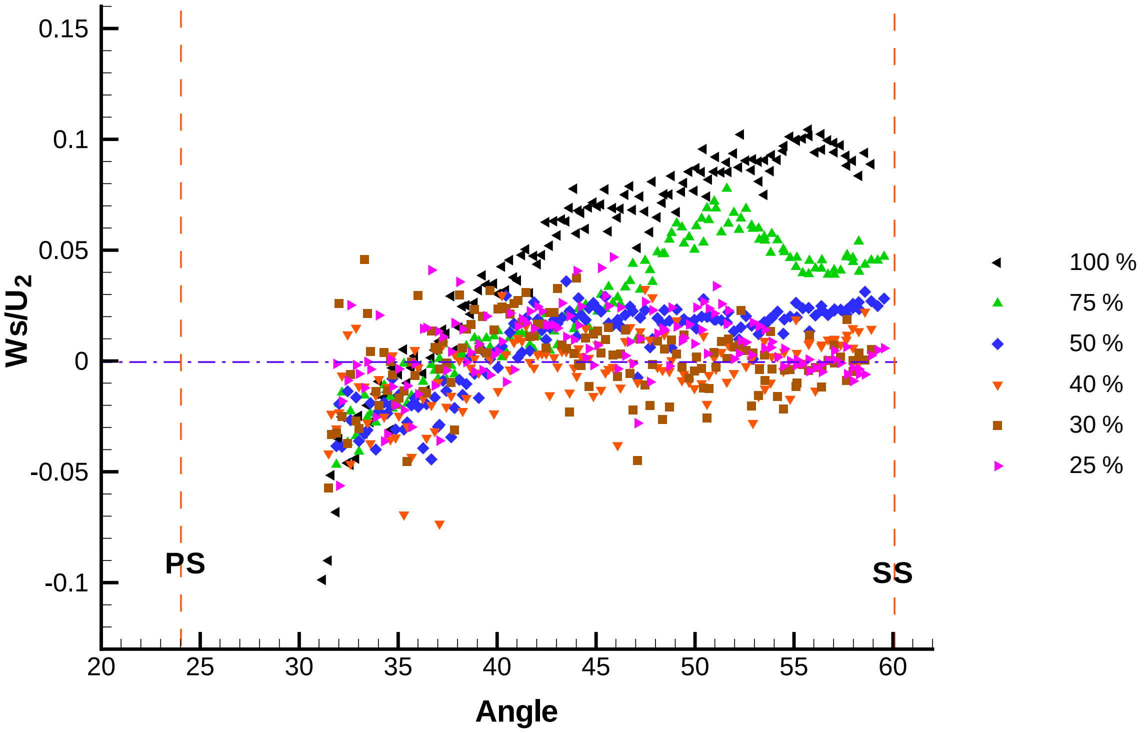

Figure 4.46: Mean normalized secondary velocity at r = 165 mm for 100 %, 75%, 50%, 40%, 30% and 25% of design flow rate

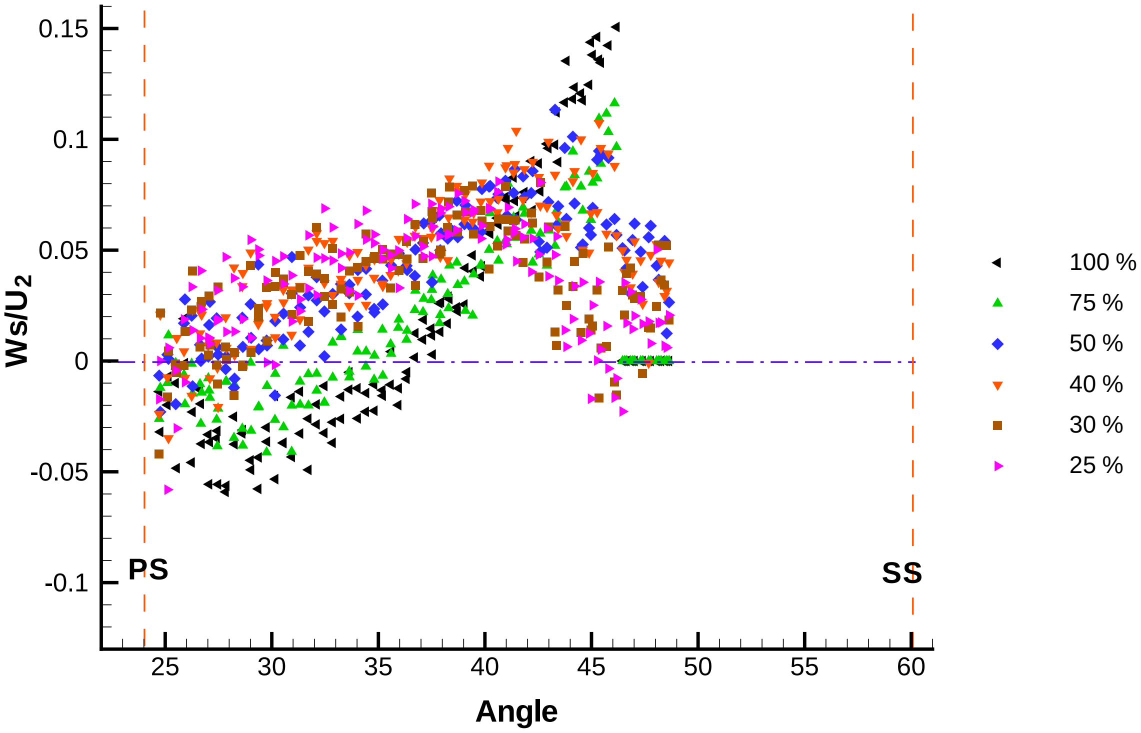

Figure 4.47: Mean normalized secondary velocity at r = 191 mm for 100 %, 75%, 50%, 40%, 30% and 25% of design flow rate

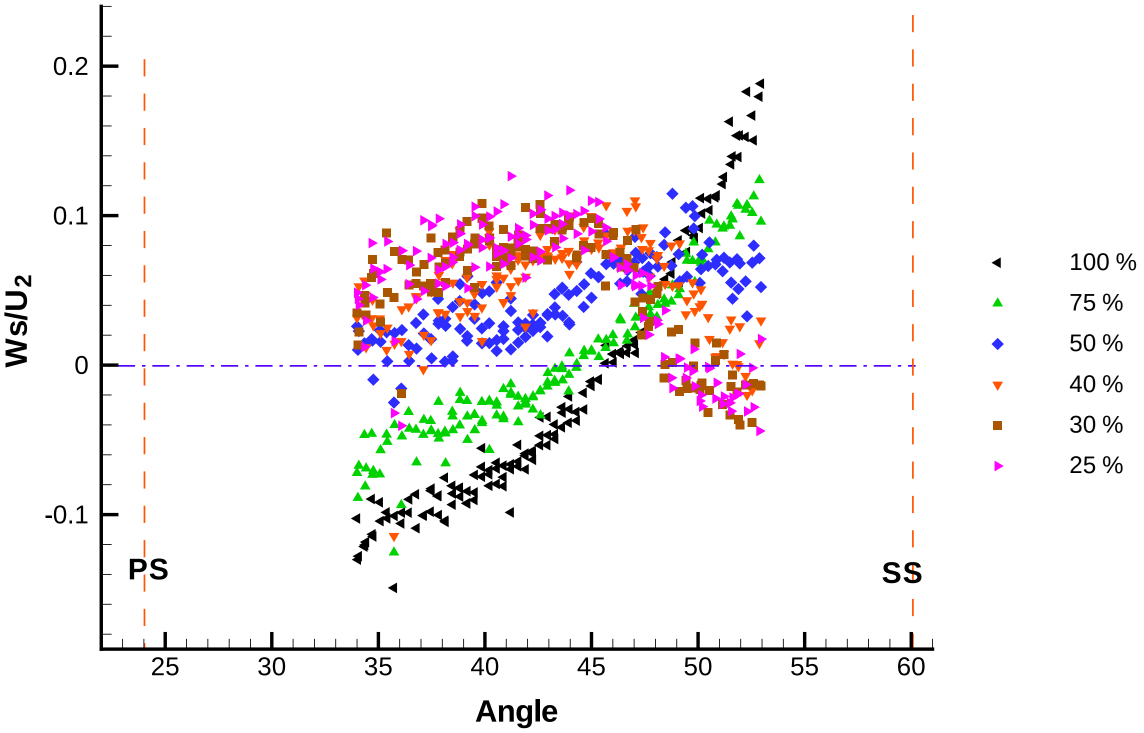

Figure 4.48: Mean normalized secondary velocity at r = 216 mm for 100 %, 75%, 50%, 40%, 30% and 25% of design flow rate

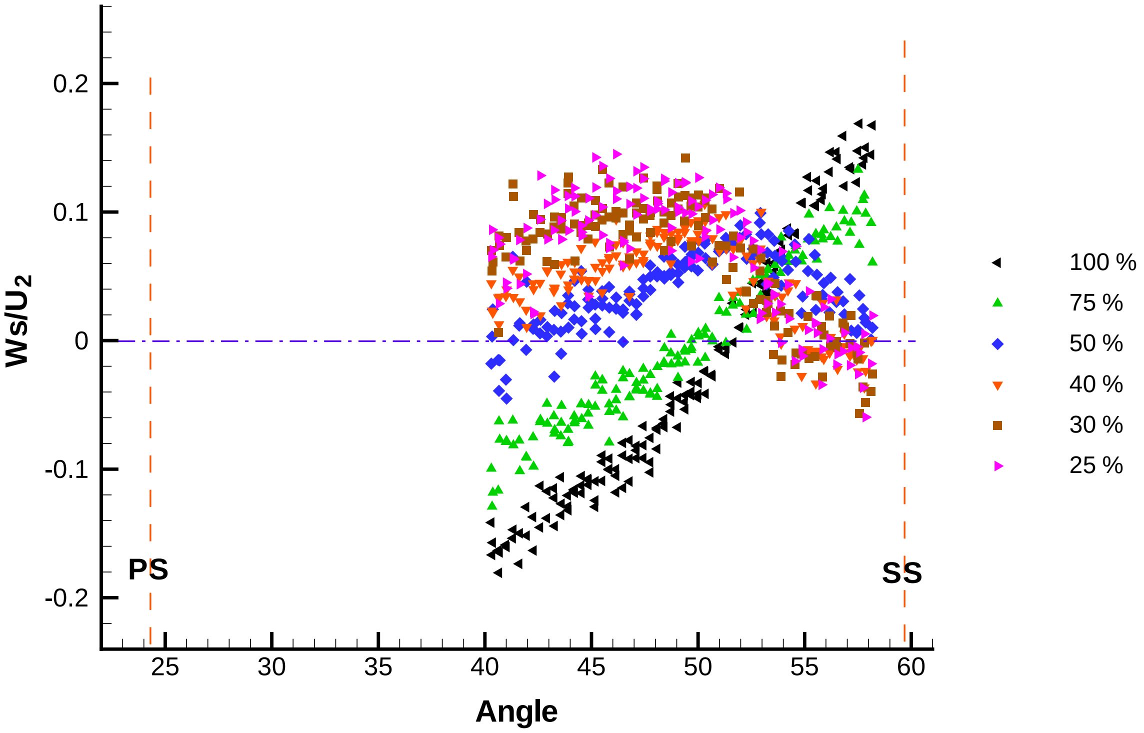

Figure 4.49: Mean normalized secondary velocity at r = 229 mm for 100 %, 75%, 50%, 40%, 30% and 25% of design flow rate

4.3.3 Turbulence Intensities at Design and Off-Design Conditions

Turbulence intensities (TI) in this research is a measure of the fluctuations in x and y components of the relative velocity vector. The turbulence intensity calculation includes the Turbulence Kinetic Energy (TKE) which measures the deviation of the instantaneous x (W_x) and y (W_y) components of the relative velocity from the mean values of those components [10].

$$TKE = \frac{\overline{W_x'^2} + \overline{W_y'^2}}{2} \tag{4.3}$$

$$TI = \sqrt{\frac{TKE}{W_x^2 + W_y^2}} \tag{4.4}$$

where $\overline{W_x'^2}$ and $\overline{W_y'^2}$ in the TKE is substituted by the standard deviation calculated by the Flow Manager program. Areas with high turbulence intencity values indicate the existance of flow separation and moving vortices due to the vast changes in the velocity gradients in those areas.

Contour maps of the turbulence intensities calculated at the inlet for design and off-design conditions are shown in Figure 4.50. Figure 4.51 shows the turbulence intensities calculated at design and off-design conditions at the outlet frame. Looking at the frames taken at the inlet (Figure 4.50), it is very clear how the path of the vortices that started as separation close to the suction side were moving towards the mid channel as the flow was decreased from the design flow rate. The same pattern was present in the turbulence intensity maps taken at the outlet frame (Figure 4.51). Comparing inlet and outlet frames at the same flow rate shows how the separation propagated towards the exit throughout the channel passage. For instance, at 50% of the design flow rate, the separation that started in the suction side at the tip of the blade grew wider off the suction side at the exit of the channel. The same was observed at different frame locations (inlet and outlet) for the same flow rate. The fact that the vortices formed at off-design conditions are continuously moving contributed to some errors in the representation of thier locations in the turbulence intensity maps shown.

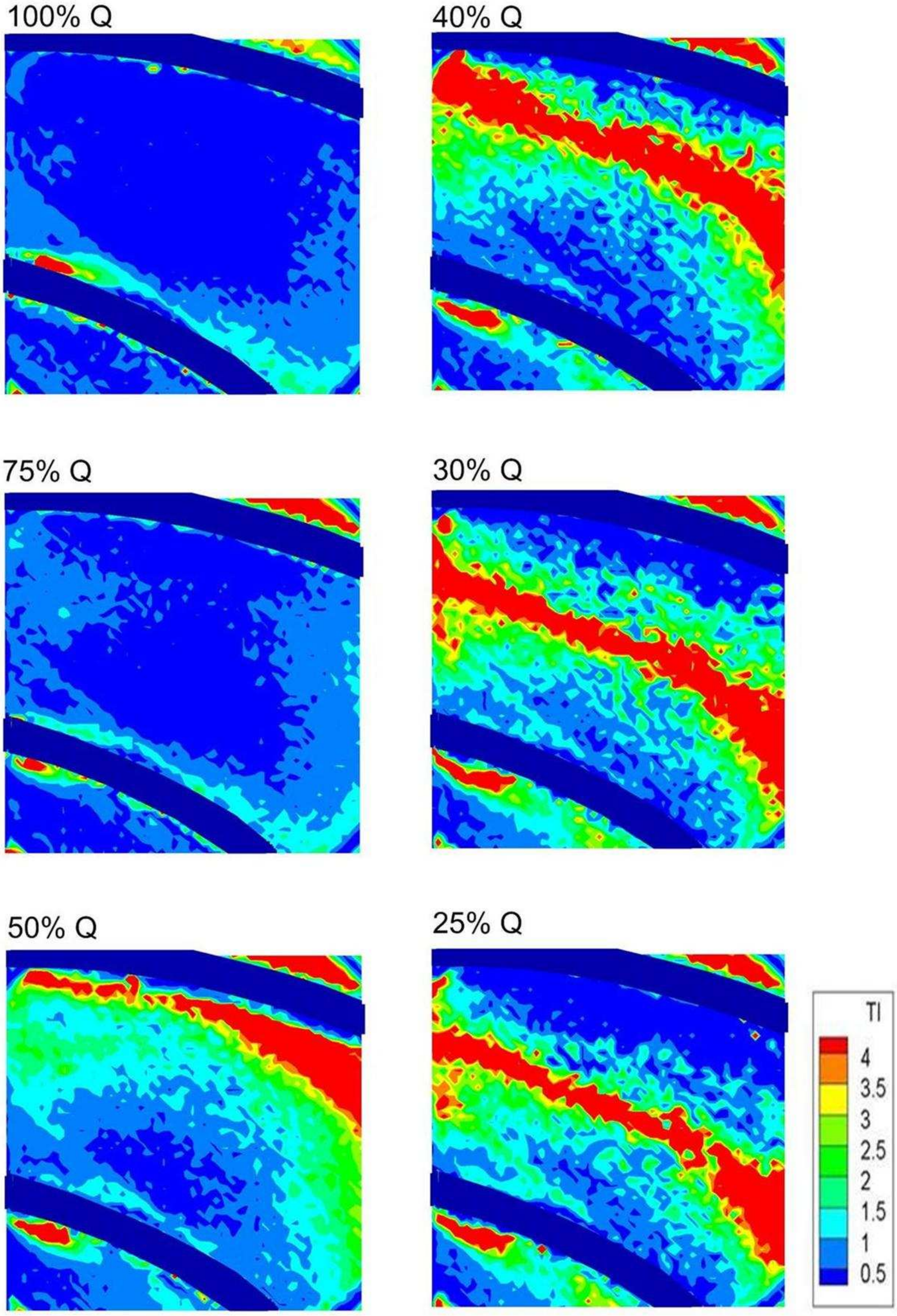

Figure 4.50: Turbulence intensity contour at the inlet at design condition (100 %), 75%, 50%, 40%, 30% and 25% of the design flow rate

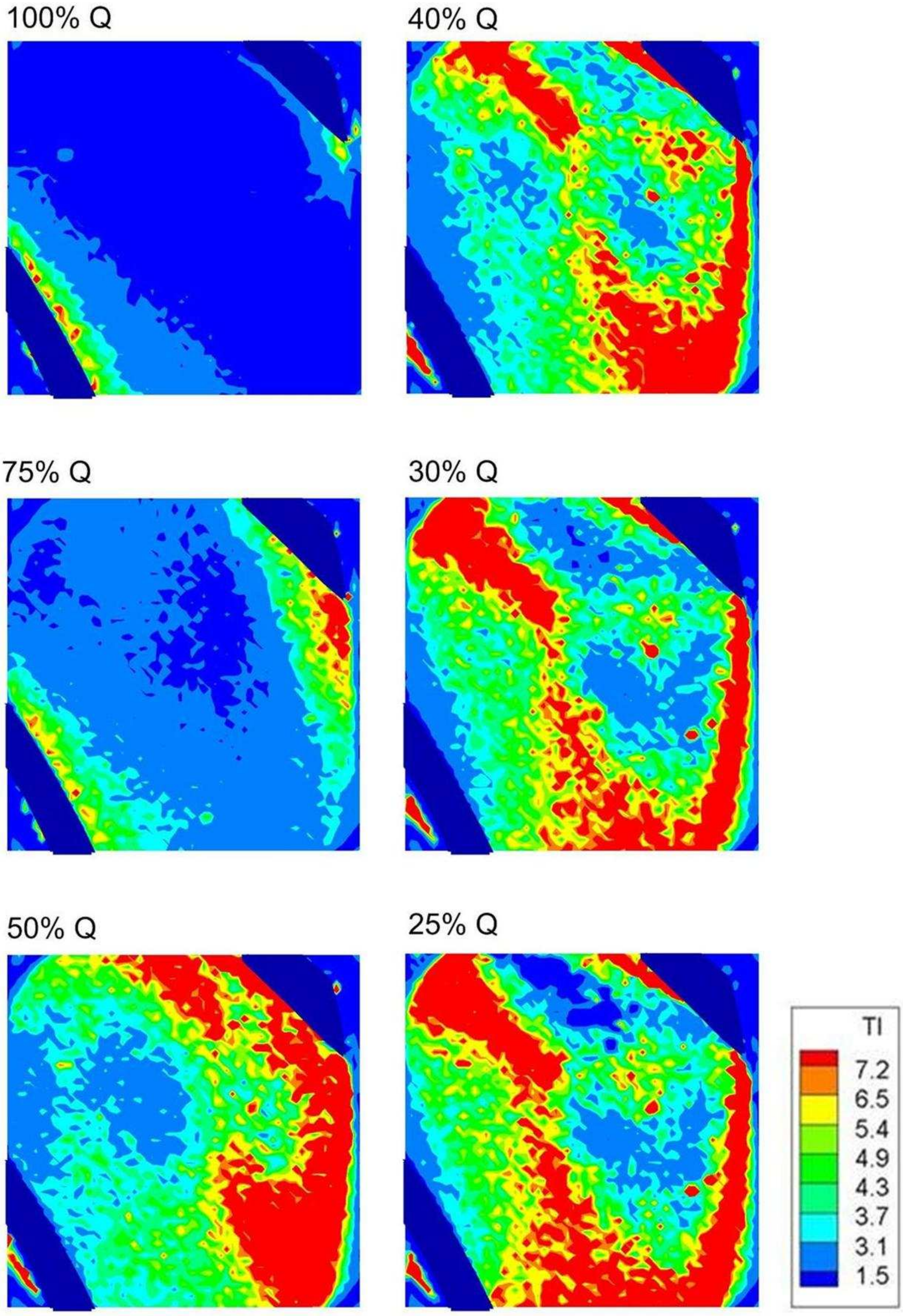

Figure 4.51: Turbulence intensity contour at the outlet at design condition (100 %), 75%, 50%, 40%, 30% and 25% of the design flow rate

4.3.4 Angle Deviation

In order to find the direction of the relative velocity, its deviation from the blade curvature was studied. To find this deviation, the primary velocity angle was found using the following formula:

$$\beta_r = \tan^{-1}\frac{W_p}{W_s} \tag{4.5}$$

Where β_r is the relative velocity angle. The difference between the relative velocity angle and the blade angle, β_2, (30 degrees) was found using the following equation:

$$\beta_d = \beta_r - \beta_2 \tag{4.6}$$

Contour plots of β_d at design condition at the inlet measured in this research (a) and that done by Pedersen [10]are shown in Figure 4.52 (a) and (b), respectively. A value of zero indicates that the primary velocity is following the blade curvature. Positive β_d values indicate that W_p is directed towards the suction side while negative β_d values mean that the fluid is moving toward the blade's pressure side. In Figure 4.52 a, positive values were noticed indicating that fluid is moving toward the suction side at the inlet. This result was very similar that found by Pedersen (Figure 4.52 b). On the other hand, negative values were found at the outlet of the channel indicating that the fluid was moving towards the pressure side (Figure 4.53a). This result was very similar that found by Pedersen (Figure 4.53 b). The impeller used by Pedersen was a 6-blade backward swept impeller and this is believed to be the cause of the minor differences in the calculated angle values found between the contour plots of this research and Pedersen's [10]. The existence of this deviation caused part of the change in the H-Q plot calculated earlier (Figure 4.4).

a) Altaf

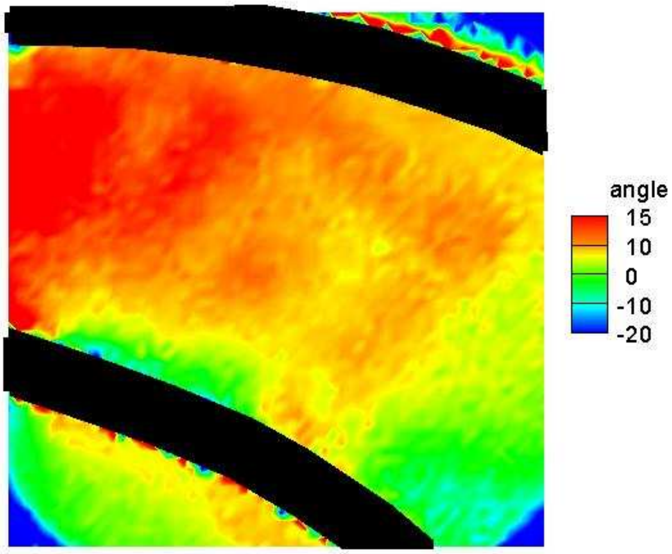

b) Pedersen

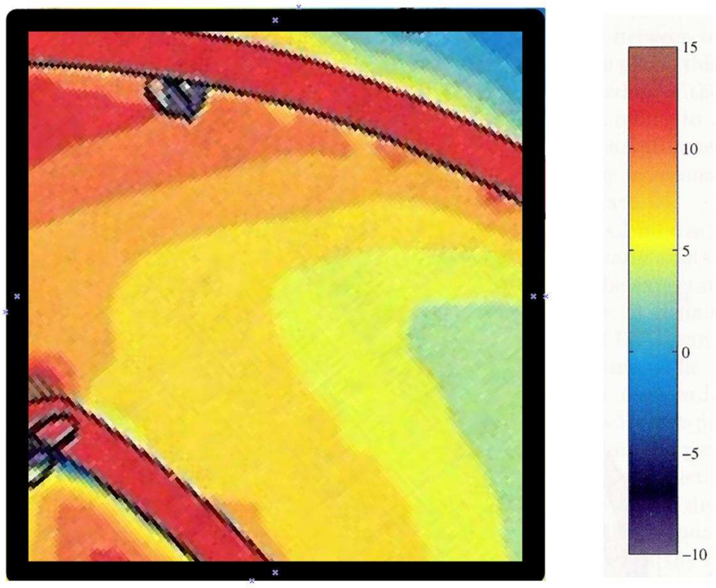

Figure 4.52: Angle deviation at 100% flow rate at the inlet for a)Altaf and b)Pedersen [10]

a) Altaf

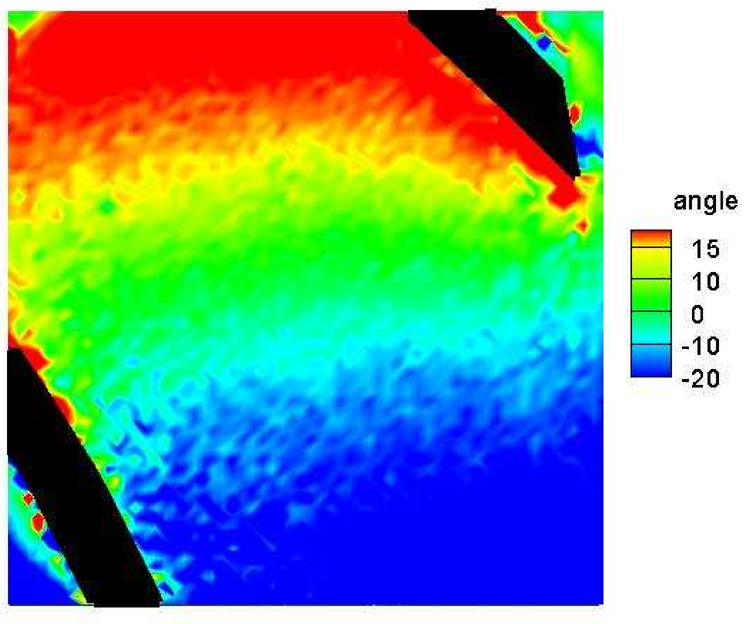

b) Pedersen

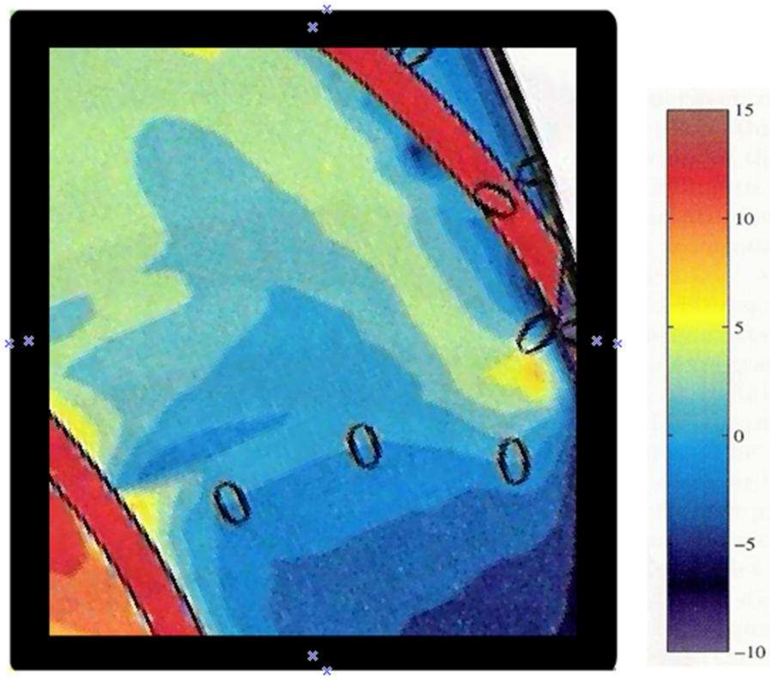

Figure 4.53: Angle deviation at 100% flow rate at the outlet for a)Altaf and b)Pedersen [10]

4.3.5 Comparison of PIV Results at Design Condition

A comparison of the normalized primary and secondary velocity profiles at design flow rate in three different locations inside the impeller passage will be presented in this section. This comparison was made using the available results found by Hesse [25] and Onwuama [26] at 140 mm, 191 mm and 229 mm from the centre of the impeller. An impeller, which was the same in dimensions as the impeller of this research work, was used in both research studies of Hesse [25] and Onwuama [26]. Differences between the two impellers, if there are any, are the results of the manufacturing process. Hesse [25] and Onwuama [26] conducted their experimental work using LDV and PIV, respectively.

Figure 4.54 demonstrates the mean normalized primary velocity obtained in the three studies at the three locations mentioned above. The pattern of the velocity profile was very similar where a smaller magnitude of the primary velocity observed close to the pressure side and then it increased as it approached the suction side. The effect of the suction side boundary layer was captured in all three cases at all locations (except at Figure 4.54 b where the image frame does not capture the whole width of the passage). At the inlet (Figure 4.54 a), there were few differences between the three studies and this was expected due to the large change the fluid faces as its direction was changed from axial to radial when it entered the impeller channels. As the flow proceeded further inside the channels, it started behaving as in the theory explained in Chapter 1 where the match between the three studies was noticed at 191m and 229 mm represented in Figure 4.54 b and c. The velocity profiles of the three studies were shifted (do not fall on the top of each other) and this could be due to factors such as the slight differences (due to accuracy of measuring devices) in the flow rate , the rotational speed and other factors which do not match in all the studies. The same observations for the mean normalized primary velocity are applicable to the profiles of the mean normalized secondary velocity at 140 mm, 191 mm and 229 mm of the three studies (Figure 4.55).

a) 140mm

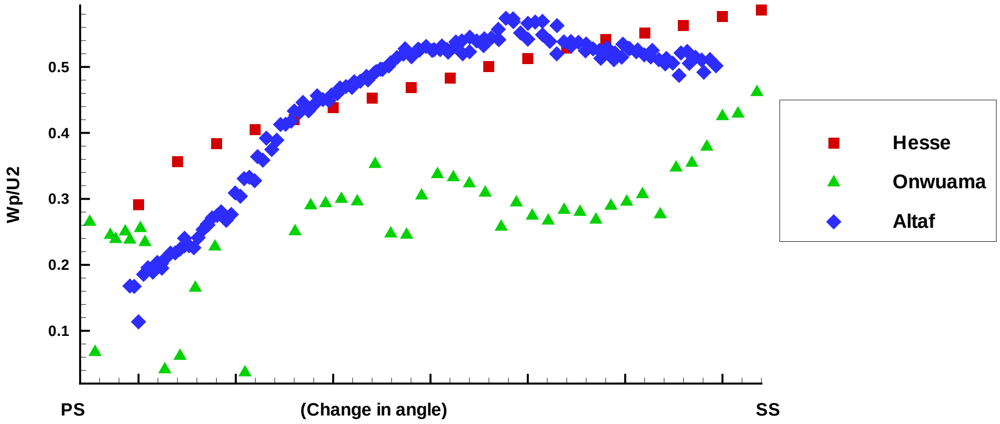

b) 191mm

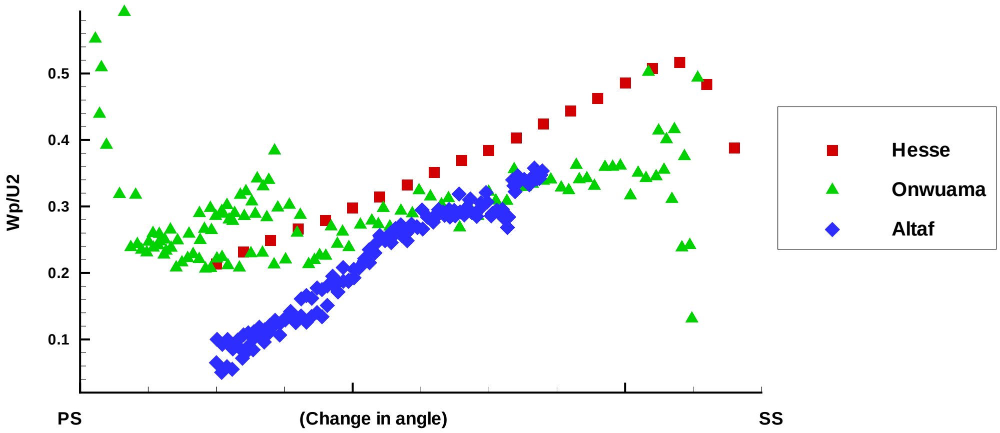

c) 229mm

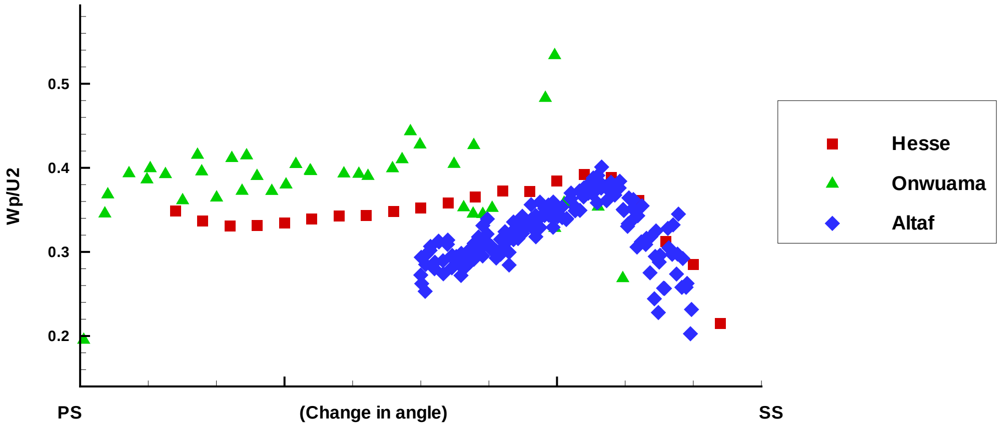

Figure 4.54: Comparison of mean normalized primary velocity at design condition at three different locations with Onwuama and Hesse results [25, 26]

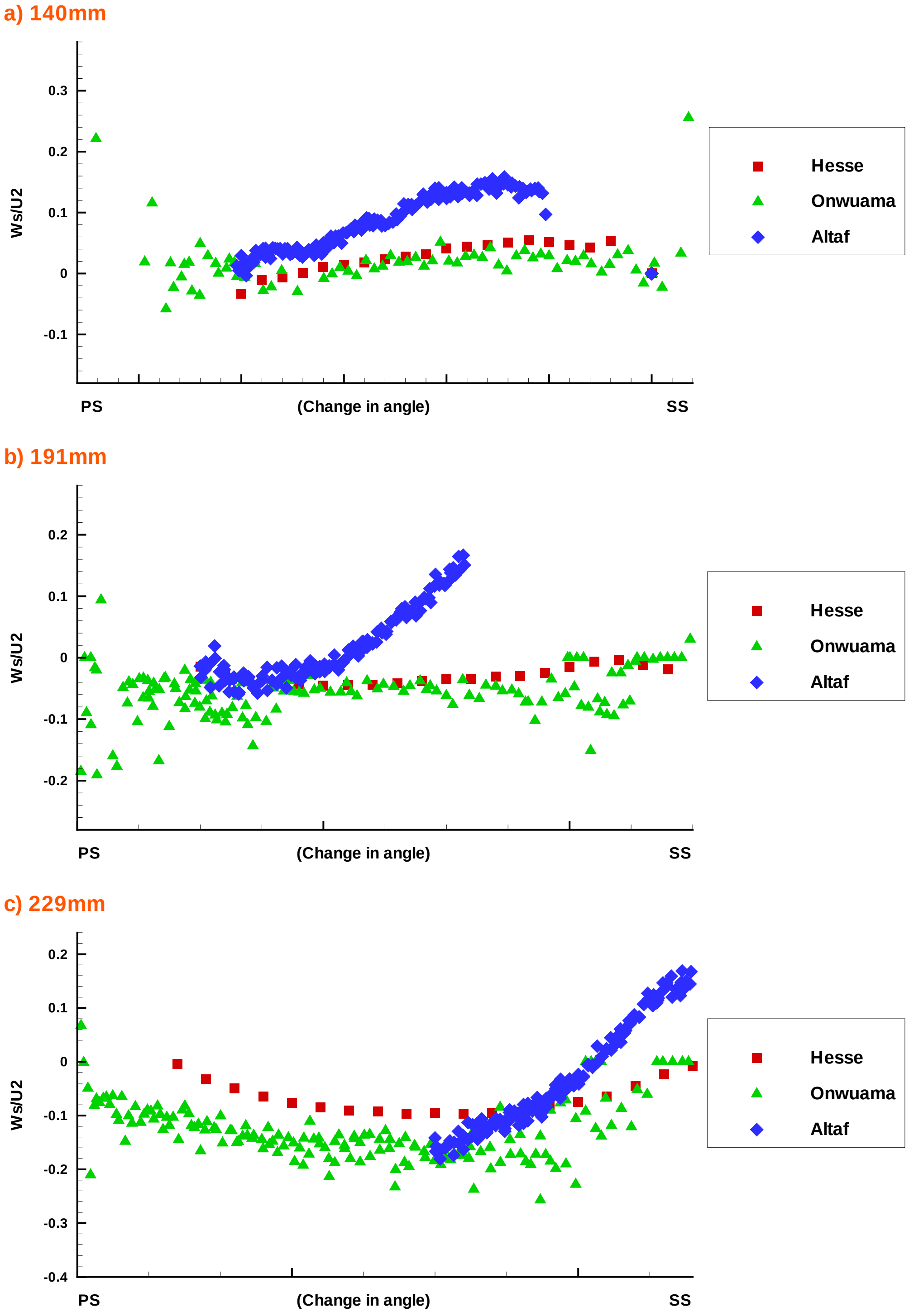

Figure 4.55: Comparison of mean normalized secondary velocity at design condition at three different locations with Onwuama and Hesse results [25, 26]

4.4 Visual Observations

The reason of manufacturing a completely transparent impeller was to facilitate the analysis of the flow inside all the channels. This analysis could be done using a measurement technique such as the PIV technique used in this research. Also visual observation, if possible, can help in supporting the qualitative results found using the measurement technique used. Detecting cavitation bubbles or a rotating stall pattern, for example, are types of possible visual observation. A pattern of bubble accumulation developed inside the impeller channels when conducting this research work will be analyzed in this section.

Each set of PIV images was taken over at least a two hour time period. It was noticed, due to the transparent acrylic hub covering all the channels, that small bubbles were formed at 30% and 25% of the design flow rate experiment runs. These bubbles were sticking to the hub plate and they were located close to the suction side at the channel exit (Figure 4.56 and Figure 4.57). These bubbles were alternating between the 8 channels of this impeller. When the runs were repeated, the bubbles were formed in the same alternating pattern but on a different set of blades. If the impeller was left running for a short period of time these bubbles are not formed with the same quantity. This implies that this pattern of bubbles is not rotating between the impeller blades otherwise it would not form as dense bubbles as found after a two hour run. It is not clear if these bubbles resulted from possible cavitations or if they were originally trapped in the test rig parts. The water was left in the rig for several days to allow gases in the cold-filled-water to come out.

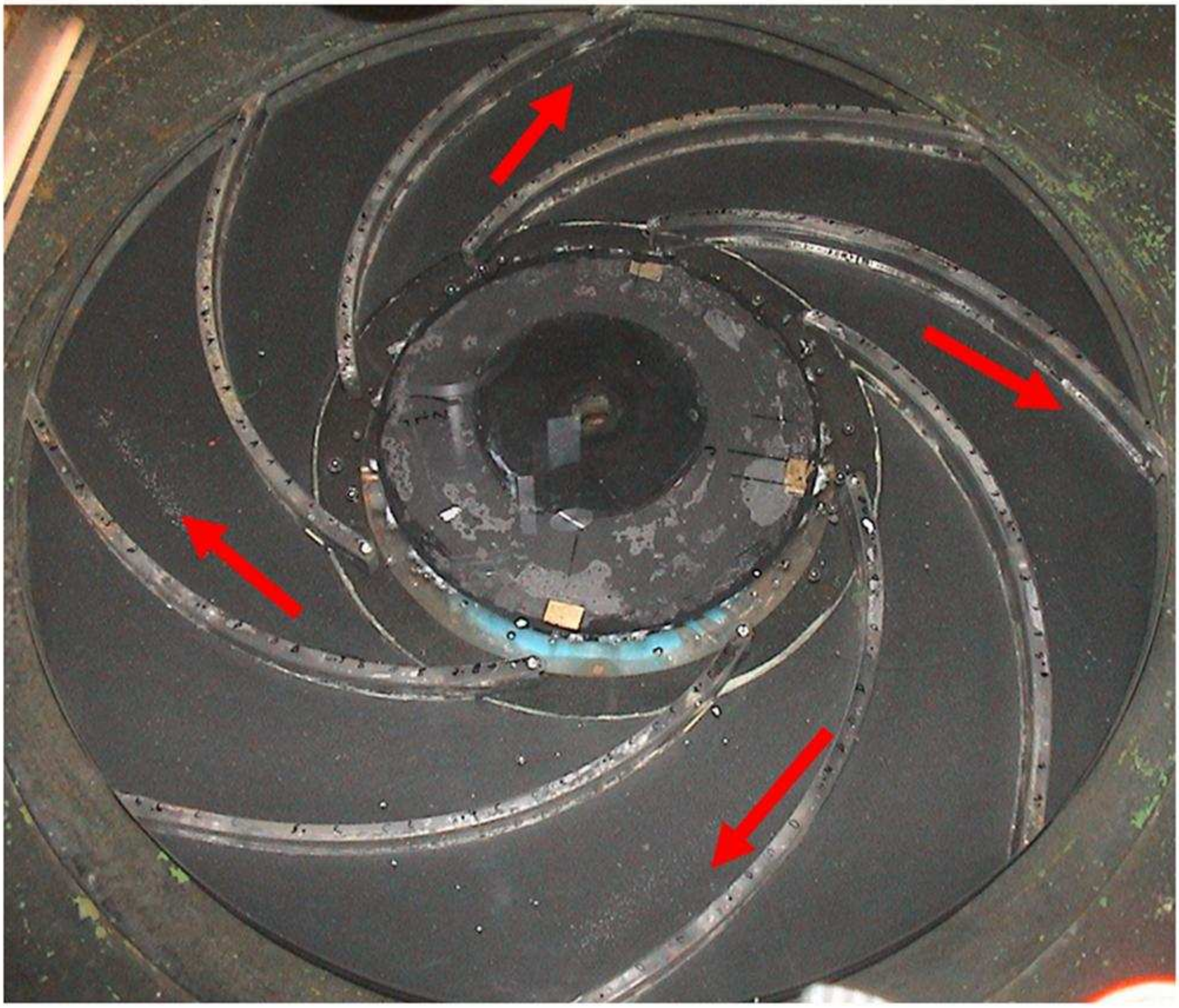

Figure 4.56: Alternating pattern of the bubbles formed and accumulated at the hub internal surface close to the suction side at 25 % of the design flow rate

Figure 4.57: Bubbles formed and accumulated at the hub internal surface close to the suction side at 25 % of the design flow rate

4.5 Summary of Experimental Results

The experimental results of the performance of the newly constructed impeller and the flow behaviour at both design and off-design conditions were presented in this chapter. The impeller performance parameters at design condition were compared with the theoretical Euler models and the results were found to be as expected from an actual impeller experiment.

Using the PIV technique, the flow behaviour at the design condition and off-design condition (75%, 50%, 40%, 30% and 25% of the design flow rate) was analyzed. At design condition, the fluid flow was very similar to the theory of the flow behaviour described in Chapter 1. There was no tendency to flow separation throughout the whole channel with the relative velocity moving towards the suction side at the inlet and towards the pressure side at the channel outlet. The same flow pattern was observed by Choi [23]. There was no significant change in the general flow behaviour between the design condition and 75% flow rate case. When compared with the design condition, major changes in the flow behaviour started to appear at flow rates lower than 50% of the design flow rate. This included the development of a separation area at the suction side of the impeller channel at 50% and 40% of the design flow rate. A larger circulation region occurred at flow rates of 30% and 25% of the design condition. This caused circulation of the fluid inside the channel, restricting the through flow. In contrast, a smooth through flow from the inlet to the outlet was observed at the design condition (100% flow rate). Similar results at design condition and 25% of the design flow rate were observed in studies done by Pederson [10], Hesse [25], Onwuama [26] and Behseta [27]. The existence of two vortices at the instantaneous images at 25% of the design flow rate was similar to those found by Behseta [27]. Choi [20] and Kittmer [19] observed flow seperation on the suction side at off-design conditions similar to that found in this study.

The mean normalized primary and secondary velocity profiles at design and off-design conditions were measured and presented in this chapter. It was noticed that the mean normalized primary velocity profile for both the design condition and 75% flow rate was positive throughout the whole channel indicating the absence of any inward flow. At 50% and 40% flow rates, inward flow was observed at the exit of the channel where negative values of the mean normalized primary velocity were measured. In contrast to the 100% flow rate, inward flow from the outlet to inlet of the channel close to the suction side was observed at 30% and 25% of the design flow rate. Due to the smaller magnitude of the normalized secondary velocity components, the change in the direction of the relative flow from suction side at the inlet to pressure side at the outlet was clearer for the design condition case. At off-design conditions, developing patterns of relative velocity direction was harder due to the high fluctuation in the secondary velocity component between positive and negative values. The profiles of the mean normalized primary and secondary velocity components of this study and those measured by Hesse [25] and Onwuama [26] were satisfactorily similar specially for the primary velocity components. These results were also similar to those found by Behseta [27].

Turbulence intensity calculations showed no major variation in the magnitudes of velocity components among the same set of image at the design condition. Once the flow rate was reduced from 100%, changes in the velocity magnitudes among the same set appeared at the suction side and moved towards the mid channel as the flow was reduced to severely low flow rates. These areas of high turbulence intensities indicated large changes in the velocity magnitudes which was believed to be due to the effect of small eddies and vortices moving along those areas. Contour maps of the turbulence intensities at the design condition measured in this study are very similar to those measured by Behseta [27].

Another supporting result to the flow behaviour at the design condition was found by calculating the angle deviation of the relative velocity from the blade curvature. The results of angle deviation in the 6-blade impeller of Pederson [10] were very similar to those found in this research work.

Visual observations indicated an alternating existence of tiny bubbles inside the impeller channels. The time it took those bubbles to form (almost 2 hours for each experiment setting) strongly supported the fact that the stalled cells were stationary. It was not clear if those bubbles were the result of cavitation. Pedersen et al. [21] found similar alternating stall pattern to that found in this study.

Chapter 5

Conclusions and Recommendations

5.1 Conclusions

At normal operating conditions, attaining higher pump performance is possible if better understanding of the flow behaviour of fluids inside pumps is achieved. Flow rate reductions and flow network interruptions are part of industrial activities. Thus, understanding pump performance at these off-design conditions is crucial in saving industrial assets and maintaining acceptable network operations.

In this research work, an experimental analysis using the PIV technique was performed on a low specific speed centrifugal impeller with 8-backswept blades maintaining a constant blade angle of 30 degrees. This impeller was manufactured using acrylic material to improve flow analysis and visibility. The pump's performance was measured where an efficiency of 64.8% was reached at 13.43 L/s.

The experimental work took place in a test rig that was designed to control the flow rate and impeller rotational speed as required. To investigate the flow inside the impeller channels, sets of 1000 images were taken at both inlet and outlet of the channel. At each location, the flow behaviour was investigated at design flow rate, 75%, 50%, 40%, 30% and 25% of the design flow rate. This included the analysis of relative velocity vector maps, turbulence intensity contours, relative velocity angle deviation, and primary and secondary velocity profiles at six different locations inside the impeller channel (140 mm, 152 mm, 165 mm, 191 mm, 216 mm and 229 mm from the centre of the impeller).

At design flow rate, the results showed a well-behaved flow pattern that matched the theoretical flow behaviour. There was no evidence of flow separation and experimental results fairly matched other experimental findings in previous experimental work for a similar pump design.

A flow rate of 75% of the design flow rate was found to be an acceptable operating condition with no obvious flow separation detected. Flow separation was detected at 50% of the design flow rate which affected the impeller performance by blocking part of the channel passage. It was found that the channel blockage due to the flow separation became larger as the flow rate is reduced and started shifting towards the mid passage of the channel. Non stationary vortices and eddies were formed in alternating channels of the impeller as the flow was reduced to 30% and 25% of the design flow rate. These eddies caused flow recirculation inside the channels resulting in stalled passages. There was no evidence of stall rotation between the impeller channels. Bubbles were spotted at severe off-design conditions attaching inside the impeller channel in the same stall alternating pattern.

5.2 Recommendations

Experimentally, several studies could be done to support the results found in this research work. Using the time resolved PIV approach, the start of a separation can be detected accurately. Also, the development of eddies and vortices and their movement inside the impeller channel can be studied better using this technique. The pattern of the stall cells and the possibility of cavitations occurrence can be investigated using time resolved PIV to ensure their existence (the accumulated bubbles found in this research). This technique requires the availability of a high speed camera and a more advance PIV processor. The camera should be able to capture images of the whole impeller or otherwise be attached to the rotating shaft.

The effect of changing the number of blades on the flow behaviour can be studied but required manufacturing a new impeller. Also, changing the type of fluid to study the effect of fluid viscosity on the flow behaviour inside the channels can be studied. The fluid selected must be safe to use, cheap, easy to clean and replace and transparent for the PIV technique to work. The effect of introducing a volute (must be transparent) on the flow behaviour inside the impeller can be studied.

Numerically, a simulation study could be done to predict the flow behaviour at design flow condition and off-design flow rates. The RANS method and the LES method could possibly provide enough details of the flow behaviour especially at low flow rates. Simulating the fluid flow at design condition is expected to generate fairly similar results but not at off-design conditions [26, 27].

Improving the cross-correlation codes that process each pair of images in terms of sub-pixel resolution and filtering is another area of enhancement.

Bibliography

[1] F. M. White. *Fluid Mechanics.* McGraw-Hill, New York, 5th edition, 2003.

[2] S. L. Dixon. *Fluid Mechanics, Thermodynamics of Turbomachinery.* Pergamon Press, Oxford, 3rd edition, 1978.

[3] G. F. Round. *Incompressible Flow Turbomachines: Design, Selection, Applications, and Theory.* Butterworth-Heinemann, 2004.

[4] R. L. Daugherty, J. B. Franzini, and E. J. Finnemore. *Fluid Mechanics With Engineering Applications.* McGraw-Hill, 8th edition, 1985.

[5] D. A. Johnson. Turbomachines-ME563 course notes, 2006.

[6] R. K. Turton. *Principles of Turbomachinery.* Chapman Hall, London, 2 edition, 1995.

[7] F. J. Wiesner. A review of slip factors for centrifugal impellers. *Journal of Engineering for Power*, 89:558–572, 1967.

[8] M. Abramian and J. H. G. Howard. Experimental investigation of the steady and unsteady relative flow in a model centrifugal impeller passage. *Journal of Turbomachinary*, 116:269–279, 1994.

[9] C. Pfleiderer and H. Petermann. *Stromungsmaschinen.* Springer, Berlin, 6th edition, 1998.

[10] N. Pedersen. *Experimental investigation of flow structures in a centrifugal pump impeller using particle image velocimetry.* PhD thesis, Technical University of Denmark, Copenhagen, Denmark, 2000.

[11] N. Krause, K. Zahringer, and E. Pap. Time-resolved particle imaging velocimetry for the investigation of rotating stall in a radial pump. *Experiments in Fluids*, 39:192–201, 2005.

[12] R. J. Adrian. Twenty years of particle image velocimetry. *Experiments in Fluids*, 39:159–169, 2005.

[13] D. A. Johnson, N. Pedersen, and C. B. Jacobsen. Measurements of rotating stall inside a centrifugal pump impeller. *In proceedings of ASME Fluids Engineering Summer Conference (FED 05)*, FEDSM2005-77313, June 19-23, 2005. Houston, Texas.

[14] C. I. Onwuama and D. A. Johnson. Experimental investigation of flow separation and blade loading in a low specific speed centrifugal impeller. *In proceedings of ASME Fluids Engineering Division Summer Meeting (FEDSM 01)*, FEDSM2001-18075, May 29- June 1, 2001. New Orleans, Louisiana.

[15] J. H. G. Howard and P. Herman. Experimental investigation of impeller and volute flow fields for a low specific speed pump with single and double volutes. *In proceedings of the 1987 ASME/JSME Thermal Engineering Joint Conference*, 1987.

[16] Y. S. Kim J. W. Kim and C. Y. Park. Failure analysis of cracking at volute tongues of feedwater pump casings. *Engineering Failure Analysis*, 9:17–30, 2002.

[17] Y. D. Choi, K. Nishino, J. Kurokawa, and J. Matsui. PIV measurement of internal flow characteristics of very low specific speed semi-open impeller. *Experiments in Fluids*, 37:617–630, 2004.

[18] E. Lennemann and J. H. G. Howard. Unsteady flow phenomena in rotating centrifugal impeller passage. *ASME J. Eng. Power*, 92:65, 1970.

[19] C. W. Kittmer and J. H. G. Howard. Measured passage velocities in a radial impeller with shrouded and unshrouded configurations. *ASME J. Eng. Power*, 97:207–213, 1975.

[20] J. Choi, D. K. McLaughlin, and D. E. Thompson. Experiments on the unsteady flow field and noise generation in a centrifugal pump impeller. *Journal of Sound and Vibration*, 263:493–514, 2003.

[21] N. Pedersen, P. S. Larsen, and C. B. Jacobsen. Flow in a centrifugal pump impeller at design and off-design conditions-part I: Particle image velocimetry (PIV) and laser doppler velocimetry (LDV) measurements. *ASME Journal of Fluids Engineering*, 125:61–72, 2003.

[22] W. Li. Effect of viscosity of fluids on centrifugal pump performance and flow pattern in the impeller. *International Journal of Heat and Fluid Flow*, 21:207–212, 2000.

[23] Y. Choi, J. Kurokawa, and J. Matsui. Performance and internal flow characteristics of a very low specific speed centrifugal pump. *ASME Journal of Fluids Engineering*, 128:341–349, 2006.

[24] R. Dong, S. Chu, and J. Katz. Quantitative visualization of the flow within the volute of a centrifugal pump. part a: technique. *ASME Journal of Fluids Engineering*, 114:396–403, 1992.

[25] N. H. Hesse. Experimental and numerical investigation of blade passage flows in a low speed centrifugal impeller. Master's thesis, University of Waterloo, Waterloo, Ontario, Canada, 1997.

[26] C. I. Onwuama. Experimental and numerical investigation of blade passage flows in a low speed centrifugal impeller. Master's thesis, University of Waterloo, Waterloo, Ontario, Canada, 2001.

[27] S. Behseta. Off-design conditions analysis of a centrifugal impeller. Master's thesis, University of Waterloo, Waterloo, Ontario, Canada, 2005.

[28] Controlotron. *System 990 Uniflow - Field Manual.* New York, 1993.

[29] Validyne Engineering Corporation. *Instruction sheet-Pressure Transducers Model DPI5-36 and DPI15-50.* California, USA.

[30] Daytronic Corporation. *Model 3178 Strain Gage Conditioner-Instruction Manual.* Ohio, USA, 1982.

[31] Eaton Corporation. *Instruction Manual for Lebow 1600 Series Rotary Transformer Torque Sensor.* Michigan, USA.

[32] Keithley Instruments. *Model 2700 Multimeter/ Data Acquisition System- Service Manual.* Ohio, USA, 2000.

[33] M. Raffel, C. Willert, and J. Kompenhans. *Particle Image Velocimetry: A Practical Guide.* Springer, Berlin Heidelberg New York, 1998.

[34] R. J Adrian. Particle-imaging techniques for experimental fluid mechanics. *Ann. Rev. Fluid Mechanics*, 23:261–304, 1991.

[35] A. Melling. Tracer particles and seeding for particle image velocimetry. *Exp. Fluids*, 8:1406–1416, 1996.

[36] Dantec Measurement Technology. *FlowMap Particle Image Velocimetry Instrumentation - Installation and User's Guide.* Copenhagen, Denmark, 1999.

[37] R. D. Keane and R. J. Adrian. Theory of cross-correlation analysis of PIV images. *Applied Scientific Research*, 49:191–215, 1992.

[38] R. D. Marangoni T. G. Beckwith and J. H. Lienhard. *Mechanical Measurements.* Addison-Wesley, New York, 5 edition, 1993.

[39] A. Boillot and A. K. Prasad. Optimization procedure for pulse separation in cross-correlation PIV. *Experiments in Fluids*, 21:87–93, 1996.

[40] S. Elgoboshi. On predicting particle-laden turbulent flows. *Appl. Sci. Res.*, 52:309–329, 1994.

[41] J. C. Agui and J. Jimenez. On the performance of particle tracking. *Journal of Fluid Mechanics*, 185:447–468, 1987.

[42] H. Huang, D. Dabiri, and M. Gharib. On errors of digital particle image velocimetry. *Meas. Sci. Technol.*, 8:1427–1440, 1997.

[43] Y. G. Guezennec and N. Kiritsis. Statistical investigation of errors in particle image velocimetry. *Experiments in Fluids*, 10:138–146, 1990.

[44] S. K. Sinha. Improving the accuracy and resolution of particle image or laser speckle velocimetry. *Experiments in Fluids*, 6:67–68, 1988.

Appendix A

Uncertainty Analysis

In this appendix, the uncertainty calculations for the impeller efficiency, primary velocity and normalized primary velocity will be presented. The method that used in determining the uncertainty in the parameters calculated is the Root Sum Square (RSS) [38] where the uncertainty in the parameter is a result of all the uncertainties in the independent measurements (variables) which compose that parameter. In the RSS method, the uncertainty for a parameter X (ω_x) includes all the uncertainties in the variables composing X (x1, x2,...., xn) and calculated similarly to standard deviations as follows:

$$\text{Uncertainty in X:}(\omega_X) = [\sum_{i=1}^{n}(\omega_{x_i}\frac{\partial X}{\partial x_i})^2]^{1/2} \tag{A.1}$$

The uncertainty in an experiment is generated due to several sources of errors. Among them are the bias errors (B), which are consistently caused by the measuring instrument and sometimes called the systematic errors, and the precision (P) or random errors which differ for each reading and usually averaged to zero. The total error, ϵ, is calculated as follows:

$$\epsilon = [B^2 + P^2]^{1/2} \tag{A.2}$$

Beckwith et al. [38] provides more information about minimizing different types of errors in an experimental procedure.

Uncertainty in impeller efficiency calculations

The pump efficiency was calculated based on the following equation:

$$\eta = \frac{\rho g H Q}{(T - T_{Tare})\omega} \tag{A.3}$$

Therefore, the uncertainties in all the variables that compose the efficiency equation should be calculated. For those variables that compose efficiency, the following values are used:

$\rho = 1000 \quad kg/m^3$

$g = 9.8 \quad m/s^2$

$H = 0.76 \quad mH_2O$

$Q = 0.0134 \quad m^3/s$

$T = 20.2 \quad N.m$

$\omega = 15.71 \quad rad/s$

As mentioned in Chapter 2, the uncertainties of the instruments used are as follows:

uncertainty of 3% in the flow rate measurements uncertainty of 0.25% in the head measurements

uncertainty of 1% in the torque measurement

uncertainty of 1.5% in the impeller speed measurement

Based on the above mentioned values, the uncertainties for the independent variables were calculated as follows:

$\omega_Q = 0.03 \times 0.0134 = 0.000402$

$\omega_H = 0.0025 \times 0.76 = 0.0019$

$\omega_T = 0.01 \times 20.2 = 0.202$

$\omega_\omega = 0.015 \times 15.71 = 0.235$

Using the uncertainties of the variables calculated above, the uncertainty in the impeller efficiency was calculated as follows:

$\omega_\eta = (1000 \times 9.8) \times [(\frac{0.0134}{20.2 \times 15.71} \times 0.0019)^2 + (\frac{0.76}{20.2 \times 15.71} \times 0.000402)^2 + (\frac{0.76 \times 0.0134}{20.2^2 \times 15.71} \times 0.202)^2 + (\frac{0.76 \times 0.0134}{20.2 \times 15.71^2} \times 0.235)^2]^{1/2}$

$\omega_\eta = 0.058$

Finally, the measured efficiency with the uncertainty = 64.8% ±5.8%.

Uncertainty in primary and normalized primary velocity

Both bias (B) and precision (P) errors were calculated for the results obtained by the PIV technique. A sample point is selected to represent the encountered error in the PIV measurements and it was specifically chosen based on the highest standard deviation from 1000 images taken at the same location. At this point, the following values were calculated:

- angle from the horizontal x axis (reference figure), $\theta = 43.6^\circ$
- Standard deviation x component, $S_x = 0.8 m/s$
- Standard deviation y component, $S_y = 0.84 m/s$
- Primary velocity, $W_p = 2.24 m/s$

The equation used to find the primary velocity at this point is as follows:

$W_p = W_x \cos(60 - \theta)^\circ - W_y \sin(60 - \theta)^\circ$

At $\theta = 43.6^\circ \Rightarrow W_p = 0.96 W_x - 0.28 W_y$

Therefore, the uncertainty in the primary velocity W_p was calculated as follows:

$\omega_{W_P} = [(0.8 \times 0.96)^2 + (0.84 \times -0.28)^2]^{1/2}$

Therefore, $\omega_{W_P} = 0.802 m/s$.

In this experimental work, the average number of particles in the interrogation area was 8 particles. Gueznnec et al. [43] estimated an error of 4 % if 8 particles are present in the interrogation area. This means an estimated bias error of 0.09 m/s (0.04 x 2.24 = 0.09) is encountered. As a result of that, the total uncertainty in the primary velocity is:

$\epsilon_{W_p} = \sqrt{0.802^2 + 0.09^2} = 0.807$

This means that the measured primary velocity with the uncertainty at this point is = 2.24 m/s $\pm 0.8 m/s$ (35.7%). It is important to note that this high uncertainty is a result of choosing a vector with very high standard deviations among those found in the vector map.

To calculate the uncertainty in the normalized primary velocity, the following values are used:

- $W_p = 2.24\ m/s$
- $\epsilon_{W_p} = 0.807\ m/s$
- $U_2 = 3.896\ m/s$
- $\epsilon_{U_2} = \epsilon_\omega = 0.235$

where $\epsilon_{W_p/U_2} = \left[\left(\frac{\epsilon_{W_p}}{U_2}\right)^2 + \left(\epsilon_{U_2}\frac{W_p}{U_2^2}\right)^2\right]^{1/2}$

Therefore, the total error in the normalized primary velocity at the point is 0.21. This means that the measured normalized primary velocity with the uncertainty at this point is = 0.58 ±0.21(36.2%). It is important to note that this high uncertainty is a result of choosing a vector with very high standard deviations among those found in the vector map. The reason for that was to estimate the highest possible error that could occur in the measurements.